Summer 8-15-2018

Spectral and stratigraphic mapping of layered sulfate deposits on Mars using advanced CRISM data processing techniques

Kathryn Elizabeth Powell
Washington University in St. Louis

WASHINGTON UNIVERSITY IN ST. LOUIS
Department of Earth & Planetary Sciences

Dissertation Examination Committee:
Raymond E. Arvidson, Chair
Jeffrey G. Catalano
Bradley L. Jolliff
Joseph A. O'Sullivan
Douglas A. Wiens

Spectral and Stratigraphic Mapping of Layered Sulfate Deposits on Mars Using Advanced CRISM Data Processing Techniques

by
Kathryn Elizabeth Powell

A dissertation presented to
The Graduate School
of Washington University in
partial fulfillment of the
requirements for the degree
of Doctor of Philosophy

August 2018
St. Louis, Missouri

Table of Contents

List of Figures

List of Tables

Acknowledgments

First and foremost, I would like to thank my advisor, Ray Arvidson, for his guidance during my graduate education. Thank you for your thoughtful feedback on my work, your help and patience through many, many drafts, and your support of my career by sending me to conferences, team meetings, and field trips. I have truly been privileged to learn from the best. To the members of my committee, Brad Jolliff, Jeff Catalano, Jody O'Sullivan and Doug Wiens, thank you for your time and effort reviewing my dissertation.

Thank you to Nancy Chabot, Patrick McGovern, and Reginald Dufour, my undergraduate research mentors, for your guidance and encouragement. These early career opportunities to work with with planetary and astronomical data helped to make this PhD journey possible.

My graduate research was funded by the MER, MSL, and CRISM projects, as well as briefly and memorably by the Missouri Space Grant Consortium. I very much appreciate the efforts of the CRISM SOC team at JHU/APL and the MER and MSL teams at JPL and around the globe for their hard work and years of dedication to operating these spacecraft.

Thanks to Linyun He and Daniel Politte for your work building the MLM and neural network. The staff of the Remote Sensing Laboratory and PDS Geosciences Node were an invaluable resource for my data access and IT needs and generally just great people to work with.

I've been fortunate to be part of a department with an amazing grad student community. Valerie Fox was my officemate, travel buddy and receptive audience for my latest grievance with ENVI. Mike Zanetti lent his expertise and his moral support to the Iazu Crater chapter. Many people in the EPSc department have made this endeavour easier, but I want to particularly mention Abby Fraeman, Ryan Nickerson, Elaine Flynn, Kaushik Mitra, and Charis Horn. Special shout out

to the climbing crew, who encouraged me to have goals outside of work and only tried to kill me a couple of times.

Finally, I would like to thank my family. From sending me to space camp as a kid, to encouraging me to intern at APL, to chipping in for my Starbucks habit throughout grad school, your love and support has gotten me to where I am today. And a last, special thanks goes to Robert, for believing in me no matter what.

Kathryn E. Powell

Washington University in St. Louis

August 2018

Abstract of the Dissertation

Spectral and stratigraphic mapping of layered sulfate deposits on Mars using advanced CRISM data processing techniques

by

Kathryn Elizabeth Powell

Doctor of Philosophy in Earth & Planetary Sciences

Washington University in St. Louis, 2018

Professor Raymond Arvidson, Chair

We apply orbital remote sensing of Mars to analyze the mineralogy and geologic setting of two areas near rover landing sites. We use the Compact Reconnaissance Orbiter for Mars (CRISM) observations, modeled to single scattering albedo, to identify and map hydrated sulfates in layered sedimentary sequences in these two locations. In Meridiani Planum, the Opportunity rover has characterized a ~10 m section of sulfate-bearing deposits known as the Burns formation. At our study area in ~20 km to the south at Iazu Crater, we found that the crater walls have strong spectral signatures of polyhydrated sulfate, strongly correlated with a >100 m exposure of strata containing repeated dark and light banding. We use similar CRISM techniques to map a thick section of layered sulfate-bearing strata in Gale Crater, within its central mound, Mt. Sharp. The Curiosity rover will likely visit these areas and our detailed assessments will then be used to guide the rover team in choosing specific sites for upcoming traverses. To assist this study and others we deploy a neural network technique to separate reflectance and thermal contributions to CRISM I/F data, deriving temperatures and single scattering albedo spectra from 0.4-4 μm for each pixel.

Chapter 1: Introduction

This dissertation expands our knowledge of two areas on the planet Mars that are of significance to major changes in environmental conditions in its distant past. In addition, it helps to develop, test, validate, and apply for the first time a significant enhancement to the CRISM dataset. The Martian rock record preserves evidence of the water cycle through time and its effects on geology and habitability. Ancient Mars was at least episodically wetter and warmer than it is today, although probably always arid by terrestrial standards [*Stepinski and Stepinski*, 2005; *Barnhart et al.*, 2009]. In the Noachian era, the presence of water is evidenced by valley network systems that were created and phyllosilicate minerals that were formed across the planet [*Bibring et al.*, 2006; *Ehlmann et al.*, 2011]. The late Noachian and early Hesperian saw a transition to more arid conditions, which had drastic implications for the Martian hydrologic system [*Andrews-Hanna and Lewis*, 2011]. In this era of lower water availability, localized terrains were the site of formation of sulfate in groundwater upwelling systems [*Bibring et al.*, 2006; *Gendrin et al.*, 2006; *Andrews-Hanna et al.*, 2007]. Eventually even this limited and episodic water activity ceased and a dry, cold Mars has persisted for nearly 3 billion years. Very slow erosion rates since mean that ancient terrains on Mars are preserved compared to Earth, allowing us a window into these more water-rich environments in the distant past.

In this dissertation we investigate two locations on Mars that have extensive exposures of layered, sulfate-bearing sedimentary deposits. In the first, Meridiani Planum, our orbital observations broaden the extent of observations made by the Opportunity rover from tens to more than one hundred meters of sulfate strata. Meridiani Planum was chosen as the landing site for the Mars Exploration Rover Opportunity based on the identification of the iron oxide mineral

hematite, an indicator of a past aqueous environment, by Mars Global Surveyor's Thermal Emission Spectrometer (TES) [*Christensen et al.*, 2001]. Opportunity landed in Meridiani in 2004 and discovered that the bedrock is sulfate-rich sandstone, and that hematite is exposed as concretions weathered from the sandstones and concentrated on the surface as shallow ripples [*Squyres et al.*, 2004]. Through investigations of small craters along its traverse, Opportunity characterized the chemistry, mineralogy, and sedimentology of these strata, termed the Burns formation. However, the maximum thickness of the in situ investigated section of Burns was only ~10 m at Victoria Crater [*Squyres et al.*, 2009]. Regional remote sensing suggests the section of sulfate-rich sedimentary strata is much thicker than what was accessible to Opportunity [*Edgett et al.*, 2005; *Griffes et al.,* 2007; *Hynek and Phillips*, 2008; *Wiseman et al.,* 2010].

As of this writing in July 2018, Opportunity was over 14 years into its 90-day mission and investigating the rim of 22-km Endeavour Crater. Endeavour is degraded and predates the deposition of the Burns formation [*Squyres et al.*, 2012], which has subsequently embayed it. Phyllosilicate minerals have been identified on the rim of Endeavour, on Cape York [*Arvidson et al.*, 2014] and in Marathon Valley [*Wray et al.*, 2009; *Noe Dobrea et al.*, 2012; *Fox et al.,* 2016]. They are interpreted as part of a Noachian section that was altered under fairly neutral and non-oxidizing conditions.

In Gale Crater, we identify a similarly hundreds-of-meters thick section of layered, sulfate-bearing material. Our focus is on areas near the current location of the Curiosity rover, and our mapping of this region will be used to guide MSL to geologically interesting areas in the future. Since 2012, Curiosity has been exploring deposits within Gale which have been shown to be formed in fluvial-deltaic-lacustrine environments [*Grotzinger et al.*, 2015]. Curiosity is now ascending the lower layers of Mount Sharp, a 5-km high sedimentary mound within Gale Crater.

Within Mt. Sharp, clay-bearing terrains are found below sulfate-bearing terrains in a continuous stratigraphic section, recording a major environmental transition [*Milliken et al.*, 2010; *Fraeman et al.*, 2016]. The sulfate-rich section is several hundred meters thick and contains extensive banding at the meters to tens of meters scale. The sulfate section is being eroded by wind and represents a section that was once much more extensive in Gale Crater.

"Ground truth" observations of the mineralogy of the Martian surface is available in a few locations from landed missions, and from laboratory measurements of Martian meteorites. However, our knowledge of the composition of the Martian surface in most terrains comes from observations acquired from orbiting satellites. Visible and near infrared spectroscopy is used to identify minerals using their diagnostic absorption features by comparison to laboratory spectra, including clays, sulfates, olivine, pyroxene, iron oxides, and carbonates. Observed spectral signatures vary both with mineralogy and textural properties, and most geologic surfaces are a mixture of minerals rather than pure phases. Intimate mixtures of minerals have spectra that are non-linear combinations of the individual components [*Clark*, 1999]. For instance, a dust coating on basalt will preferentially darken a spectrum at longer wavelengths [*Johnson and Grundy*, 2002]. Textural variables such as grain size and packing affect spectra; in general, decreasing grain size brightens spectra in the visible and near-infrared [*Clark, 1999*]. Reflectance spectroscopy is used in tandem with other remote sensing data sets to interpret the geologic setting and history of an area.

The Compact Reconnaissance Imaging Spectrometer for Mars (CRISM) is a hyperspectral near-infrared push-broom imager aboard the Mars Reconnaissance Orbiter, which began operations at Mars in 2006 [*Murchie et al.*, 2007]. CRISM consists of two detectors operating at 0.4-1 μm ('S' detector) and 1-3.8 μm ('L' detector). Each has spectral resolution of 6.55 nm and

a nominal targeted spatial resolution of 18 m/pixel. In along-track oversampled (ATO) mode, motion of the gimbal causes rows to be taken in partially overlapping fashion such that images can be reconstructed to 12 m/pixel or better. The standard product archived by the CRISM Science Operations Center (SOC) is I/F, the radiance on sensor divided by a scaled solar spectrum and π. CRISM I/Fs in this dissertation were used to model single scattering albedo (SSA) using the Hapke function with a two-term Henyey-Greenstein particle phase function [*Hapke*, 2012]. Using the radiative transfer code DISORT [*Stamnes et al.*, 1988], we generated a multi-dimensional lookup table including atmospheric dust and ice opacities, variable lighting and viewing geometries and optionally a range of surface temperatures and pressures. To generate SSA in a CRISM scene, we interpolate the resulting table to derive the relationship between I/F and SSA for a given pixel, using MOLA-derived (Mars Orbiter Laser Altimeter) lighting geometry at 128 pixels per degree and a map of surface temperature values. CRISM has previously been used to direct the Opportunity rover to areas of scientific interest [e.g., *Arvidson et al.*, 2014; *Fraeman et al.*, 2016] and is currently being used to guide Curiosity's campaign at Vera Rubin Ridge [*Fraeman et al.*, 2018].

Chapter 2 extends our knowledge of the Burns formation with a study of Iazu Crater, a 6.8 km-diameter impact crater located ~20 kilometers south of Endeavour Crater. The Iazu-forming impact postdates all or most of the Burns formation deposition. Iazu's northern wall exposes a thick sequence of sulfate-bearing Burns formation overlying basalts with limited alteration to smectite, identified using CRISM images. This exposure of layered sulfate-bearing strata demonstrates that the Burns formation is >100 m thick in southern Meridiani Planum. These sulfates are in stratigraphic sequence with a detection of smectite beneath sulfates, thus in a stratigraphically consistent position to detections at Endeavour. Therefore the sequence exposed

at Iazu lends additional support to the sequence of events hypothesized for the Endeavour region. Eroded areas of the crater rim contain aeolian deposits that show an enhanced hematite signature, consistent with the presence of hematite-bearing sands similar to those observed by Opportunity.

In Chapter 4 we use CRISM observations in tandem with other remote sensing data sets to characterize sulfate-bearing strata in Mt. Sharp, Gale Crater. We map the layered sulfate section in detail and suggest mechanisms for the emplacement and erosion of these layers. We focus on areas that are intended for future Curiosity traverses. Our observations will be used to provide guidance for the Curiosity team on specific sites to visit in order to maximize our understanding of the layered sulfate section, including chemistry, mineralogy, surface exposure of minerals, and stratigraphic relations.

At $\lambda > 2.65$ μm, CRISM I/Fs of Mars contain both reflectance and emission components. Even with proper modeling of surface reflectance and emission, and atmospheric extinction and emission, without knowledge of the surface temperature the problem is underdetermined. Chapter 3 of this work outlines a method to simultaneously retrieve surface albedo and temperature from this wavelength region using a neural network. We apply the results to fully model CRISM spectra from 0.4-4 μm and measure the 3 μm hydration absorption. These results are applied to CRISM scenes over Gale Crater in Chapters 3 and 4.

All of the work contained in this dissertation was led by Kathryn Powell with guidance from Professor Raymond Arvidson. The following collaborators contributed in various ways to individual chapters:

Chapter 2 is published as *Powell et al.* [2017]. Dr. Michael Zanetti, now at the University of Western Ontario, contributed many helpful discussions of crater and ejecta morphology and created the HiRISE DEM of Iazu Crater. Dr. Edward Guinness of WUSTL assisted with CRISM

image processing. Dr. Scott Murchie from the Applied Physics Laboratory provided additional information about the CRISM instrument.

Chapter 3 is not intended for publication as an independent work. The method developed and validated here informs Chapter 4, and parts of it will be used in an upcoming method-focused publication led by Linyun He. The neural network code was developed by WUSTL Professor Joseph O'Sullivan and students Linyun He and Daniel Politte. Dr. Richard Morris of the NASA Johnson Space Center contributed dozens of laboratory spectra for the neural network training set as well as helpful feedback about spectral characteristics.

Chapter 4 is intended for future publication. Professor Christopher Edwards from Northern Arizona University provided THEMIS thermal inertia and HiRISE color mosaics that aided analysis.

References

Andrews-Hanna, J. C., Phillips, R. J., and Zuber, M. T. (2007), Meridiani Planum and the global hydrology of Mars, Nature, 446, 163–166, http://doi.org/10.1038/nature05594.

Andrews-Hanna, J. C., and Lewis, K. W. (2011), Early Mars hydrology: 2. Hydrological evolution in the Noachian and Hesperian epochs, J. Geophys. Res.: Planets, 116, E02007, doi:10.1029/2010JE003709.

Arvidson, R.E., et al. (2014), Ancient aqueous environments at Endeavour Crater, Mars, Science, 343, doi:10.1126/science.1248097.

Barnhart, C. J., Howard, A. D., and Moore, J. M. (2009), Long- term precipitation and late- stage valley network formation: Landform simulations of Parana Basin, Mars, Journal of Geophysical Research: Planets, 114, E01003, doi:10.1029/2008JE003122.

Bibring, J.-P., et al. (2006). Global mineralogical and aqueous mars history derived from OMEGA/Mars Express data, Science, 312, 400–404, http://doi.org/10.1126/science.1122659.

Christensen, P. R., Morris, R. V., Lane, M. D., Bandfield, J. L., and Malin, M. C. (2001), Global mapping of Martian hematite mineral deposits: Remnants of water-driven processes on early Mars, Journal of Geophysical Research: Planets, 106, 23873-23885.

Clark, R. N. (1999), Chapter 1: Spectroscopy of Rocks and Minerals, and Principles of Spectroscopy, in Manual of Remote Sensing, Volume 3, Remote Sensing for the Earth Sciences, (A.N. Rencz, ed.) John Wiley and Sons, New York, p 3- 58.

Edgett, K.S. (2005), The sedimentary rocks of Sinus Meridiani: Five key observations from data acquired by the Mars Global Surveyor and Mars Odyssey orbiters, Mars, 1, 5-58, doi:10.1555/mars.2005.0002.

Ehlmann, B. L., Mustard, J. F., Murchie, S. L., Bibring, J. P., Meunier, A., Fraeman, A. A., and Langevin, Y. (2011), Subsurface water and clay mineral formation during the early history of Mars, Nature, 479, 53.

Fox, V.K. et al. (2016), Smectite Deposits in Marathon Valley, Endeavour Crater, Mars, Identified Using CRISM Hyperspectral Reflectance Data, GRL, 43, 4885–4892, doi: 10.1002/2016GL069108.

Fraeman, A. A., et al. (2016), The stratigraphy and evolution of lower Mount Sharp from spectral, morphological, and thermophysical orbital data sets, J. Geophys. Res.: Planets, 121, 1713-1736.

Fraeman, A.A., et al. (2018), Curiosity's Investigation at Vera Rubin Ridge, Abstract 1557 presented at the 49th Lunar and Planet. Sci. Conf., The Woodlands, Tex., 19-23 March.

Gendrin, A. et al. (2006), Sulfates in Martian Layered Terrains: The OMEGA/Mars Express View, Science, 307, 1587-1591, doi: 10.1126/science.1109087.

Griffes, J.L., R.E. Arvidson, F. Poulet, A. Gendrin (2007), Geological and spectral mapping of etched terrain deposits in northern Meridiani Planum, J. Geophys. Res., 112, E08S09, doi:10.1029/2006JE002811.

Grotzinger, J. P., et al. (2015), Deposition, exhumation, and paleoclimate of an ancient lake deposit, Gale crater, Mars, Science, 350, aac7575.

Hapke, B. (2012), Theory of Reflectance and Emittance Spectroscopy, Cambridge Univ. Press, New York.

Hynek, B.M. and R. J. Phillips (2008), The stratigraphy of Meridiani Planum, Mars, and implications for the layered deposits' origin, Earth and Planetary Science Letters, 274, 214-220, doi:10.1016/j.epsl.2008.07.025.

Johnson, J. R., and Grundy, W. M. (2001). Visible/near- infrared spectra and two- layer modeling of palagonite- coated basalts, Geophysical Research Letters, 28, 2101-2104.

Milliken, R. E., Grotzinger, J. P., and Thomson, B. J. (2010), Paleoclimate of Mars as captured by the stratigraphic record in Gale Crater, Geophysical Research Letters, 37, L04201, doi:10.1029/2009GL041870.

Murchie, S., et al. (2007), Compact reconnaissance imaging spectrometer for Mars (CRISM) on Mars reconnaissance orbiter (MRO), J. Geophys. Res.: Planets, 112, E05S03, doi:10.1029/2006JE002682.

Noe Dobrea, E. Z., Wray, J. J., Calef, F. J., Parker, T. J., and Murchie, S. L. (2012). Hydrated minerals on Endeavour Crater's rim and interior, and surrounding plains: New insights from CRISM data, Geophysical Research Letters, 39, L23201, doi:10.1029/2012GL053180.

Powell, K. E., Arvidson, R. E., Zanetti, M., Guinness, E. A., and Murchie, S. L. (2017), The structural, stratigraphic, and paleoenvironmental record exposed on the rim and walls of Iazu Crater, Mars, J. Geophys. Res.: Planets, 122, 1138-1156.

Squyres, S.W. et al. (2004), In Situ Evidence for an Ancient Aqueous Environment at Meridiani Planum, Mars, Science, 306, 5702, doi:10.1126/science.1104559.

Squyres, S.W. et al. (2009), Exploration of Victoria Crater by the Mars Rover Opportunity, Science, 324, 5930, 1058-1061, doi:10.1126/science.1170355.

Squyres, S.W. et al. (2012), Ancient Impact and Aqueous Processes at Endeavour Crater, Mars, Science, 336, 570-576, doi:10.1126/science.1220476.

Stamnes, K., Tsay, S. C., Wiscombe, W., and Jayaweera, K. (1988), Numerically stable algorithm for discrete-ordinate-method radiative transfer in multiple scattering and emitting layered media, Applied Optics, 27, 2502-2509.

Stepinski, T. F., and Stepinski, A. P. (2005). Morphology of drainage basins as an indicator of climate on early Mars, Journal of Geophysical Research: Planets, 110, E12S12, doi:10.1029/2005JE002448

Viviano-Beck, C. E., et al. (2014), Revised CRISM spectral parameters and summary products based on the currently detected mineral diversity on Mars, J. Geophys. Res.: Planets, 119, 1403-1431.

Wiseman, S. M., et al. (2010), Spectral and stratigraphic mapping of hydrated sulfate and phyllosilicate-bearing deposits in northern Sinus Meridiani, Mars, J. Geophys. Res.: Planets, 115, E00D18, doi:10.1029/2009JE003354.

Wray, J. J., et al. (2009), Phyllosilicates and sulfates at Endeavour Crater, Meridiani Planum, Mars, Geophysical Research Letters, 36, L21201, doi:10.1029/2009GL040734.

Chapter 2: The structural, stratigraphic, and paleoenvironmental record exposed on the rim and walls of Iazu Crater

Associated Publication: Powell, K. E., Arvidson, R. E., Zanetti, M., Guinness, E. A., and Murchie, S. L. (2017), The structural, stratigraphic, and paleoenvironmental record exposed on the rim and walls of Iazu Crater, Mars, J. Geophys. Res.: Planets, 122, 1138-1156.

Abstract

Iazu is a 6.8 km diameter crater located ~25 km south of Endeavour Crater in Meridiani Planum, Mars. The asymmetrical ejecta deposit and crater shape demonstrate that Iazu was formed by the impact of a projectile moving from west to east at 20 to 30° above the horizontal. The crater rim and walls expose an ~115 m thick section of intact banded bright and dark Burns formation polyhydrated sulfate deposits that overlie a lower section of basaltic crust of unknown thickness that has been slightly altered to Fe^{3+}-Mg^{2+} smectites. The lower section also exhibits several basaltic outcrops that are overlain by banded bright and dark layers similar in appearance to the bright and dark bands evident in the overlying Burns formation. We interpret the lower section as indicative of a transition from regional-scale fluvial activity to accumulation of sulfate-rich deposits, culminating in a thick overlying section of Burns formation strata. Banding in the Burns formation and underlying strata is inferred to be a consequence of periodic variations in sulfate-forming depositional environments.

2.1 Introduction

Iazu Crater is a 6.8 km diameter impact crater in southern Meridiani Planum. It is located ~25 km to the south of the Noachian-age Endeavour Crater and the surrounding plains that have been explored by the Opportunity rover (Figure 2.1). The Endeavour rim segments investigated by Opportunity are dominated by Noachian age basaltic rocks with some outcrops exhibiting

evidence for mild aqueous alteration, including formation of smectites [*Arvidson et al.*, 2014; *Fox et al.*, 2016]. Opportunity drove onto Endeavour's rim after discovering, naming, and extensively characterizing the Burns formation sulfate-rich sandstones that embay Endeavour's rim segments and underlie Meridiani Planum [e.g., *Grotzinger et al.*, 2005; *McLennan et al*. 2005; *Squyres et al.*, 2012]. In this paper an ensemble of orbital data is used to show that a ~115 m thick section of intact Burns formation banded bright and dark strata is exposed in Iazu's walls, i.e. Iazu formed after emplacement of most or all of the Burns formation rocks. The Burns formation strata overlie outcrops with spectral signatures indicative of basalts slightly altered to Fe^{3+}-Mg^{2+} smectites, with these outcrops interspersed with strata similar in appearance to the overlying Burns formation outcrops.

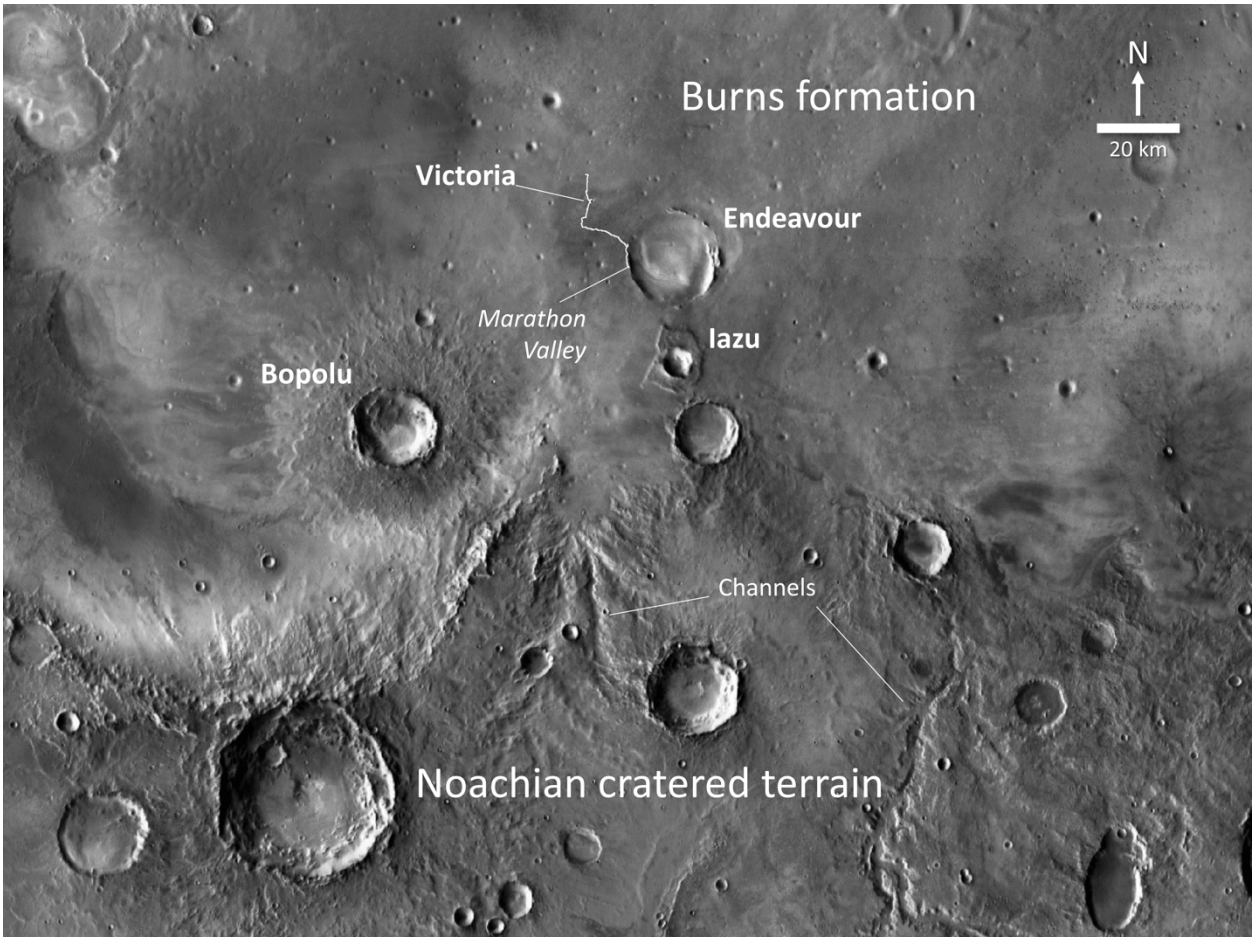

Figure 2.1: View of southern Meridiani Planum. Iazu and Endeavour Craters are located near the boundary between the Noachian cratered terrain, which has been dissected by fluvial channels, and overlain to the north by younger Burns formation sulfate-rich sandstone deposits. This view was created from THEMIS daytime thermal infrared mosaic [*Christensen et al.*, 2004a]. Opportunity's traverse from landing to Marathon Valley on the Cape Tribulation segment of Endeavour Crater is shown as a white line.

Iazu is the only crater in the vicinity of Opportunity's traverse and measurement campaigns that is large enough and young enough to expose both Burns formation and underlying rocks on its walls. Results presented in this paper extend characterization of the stratigraphic range of Burns formation rocks examined by Opportunity and allow characterization of the transition between basaltic and sulfate-rich rocks. Inferences are postulated at the end of this paper about regional-scale paleoenvironmental conditions inferred from the stratigraphy and vertical variations, thereby complementing Opportunity's observations of the ~10 m upper section of Burns formation strata.

2.2 Meridiani Planum Geologic Context

In this section of the paper a broad overview of the geology of the Meridiani area is presented to set the stage for how analyses of the strata exposed on Iazu's walls extend our understanding of processes operative in this region during the Noachian to early Hesperian Periods. From a global viewpoint the Martian rock record preserves evidence of diverse ancient environments with much greater water availability in the past. Phyllosilicate minerals have been identified, largely dating to the Noachian period (4.1-3.7 Gyr), that formed by alteration in relatively neutral pH aqueous environments [*Poulet et al.*, 2005; *Bibring et al.,* 2006; *Bishop et al.,* 2008; *Ehlmann et al.,* 2011; *Ehlmann and Edwards*, 2014; *Arvidson et al.*, 2014; *Fox et al.*, 2016]. Global environmental change beginning late in the Noachian and through the Hesperian (3.7-3.1 Gyr) led to decreased water availability, a change in fluvial channel morphology consistent with decreased erosion rates [*Andrews-Hanna and Lewis*, 2011], and the formation of hydrated sulfate-bearing deposits preferentially in low-lying areas [*Bibring et al.,* 2006].

Meridiani Planum preserves a record of several periods of aqueous processes based on extensive studies using orbital-based remote sensing observations [e.g., *Gendrin et al.,* 2005; *Hynek and Phillips*, 2008; *Wiseman et al.*, 2010; *Arvidson et al.,* 2015], and detailed measurements from Opportunity [e.g., *Squyres et al.,* 2004; 2006; 2009; *Grotzinger et al.*, 2005; *Arvidson et al.,* 2014; 2015; 2016; *Fox et al.*, 2016]. As described by *Hynek and Phillips* [2001], during the Noachian the Meridiani region was the site of extensive fluvial erosion, transporting sediment to the northwest. Ancient fluvial channels are evident to the south of the Meridiani plains that underlie Burns formation deposits (Figure 2.1). Fluvial erosion is also interpreted to have occurred in the portion of Meridiani explored by Opportunity. Endeavour Crater formed before emplacement of the Burns formation deposits based on embayment relationships [*Grant et al.*, 2015; *Crumpler et*

al., 2015]. *Grant et al.* (2015) interpreted the degradation state of Endeavour as being in large part due to fluvial erosion before the deposition of the Burns formation.

By the late Noachian to early Hesperian the hydrologic environment shifted to allow this region to become a depositional center, with Burns formation materials burying the fluvially dissected terrain [*Grotzinger et al.*, 2005; *Squyres et al.*, 2012] (Figure 2.1). Several origins for the Burns formation strata have been proposed. *Knauth et al.* [2005] interpreted the deposits as emplaced as a surge deposit from a giant impact event. *Niles and Michalski* [2009] postulated that the deposits formed as a giant ice-dust deposit. *McCollom and Hynek* [2005] argued that the Burns formation is an altered pyroclastic deposit. However, the origin best supported by in situ Opportunity observations of primary sedimentary features, facies changes, composition, and mineralogy is that sulfate-rich evaporites formed in a shallow playa environment, mixed with basaltic materials, and were then reworked and diagenetically altered to form the Burns formation deposits [e.g., *Grotzinger et al.*, 2005; *McLennan et al.*, 2005, *Squyres et al*., 2006]. Meridiani was a topographically low area for regionally-sourced groundwater upwelling and consequent evaporation [*Andrews-Hanna et al.*, 2010]. The rising and falling water table brought Fe^{2+} and other dissolved ions produced by corrosion of basalt to the surface into contact with an oxidizing atmosphere, resulting in the oxidation of aqueous Fe^{2+} ions to Fe^{3+}, and thereby lowering the pH of surface waters [*Hurowitz et al.*, 2010]. Sulfate-rich evaporite muds then formed from the evaporating acidic brines mixed with local basaltic materials, e.g., sands advected in by winds. The deposits were then reworked by wind and water, and cemented into Burns formation sulfate-rich sandstones, with later formation of hematitic concretions.

The Burns formation is up to ~800 m thick based on crater infill and superposition relationships, measured in areas up to hundreds of kilometers to the north and east of Iazu Crater

[*Edgett et al.*, 2005; *Griffes et al.,* 2007; *Hynek and Phillips*, 2008]. Deposit thicknesses near Iazu are estimated to be ~200 m [*Edgett et al.,* 2005], up to ~300 m [*Wiseman et al.,* 2010], or up to ~400 m [*Griffes et al.,* 2007]. In addition, *Grant et al.* [2015] estimated that the Burns formation deposits within Endeavour Crater are ~100-200 m thick. Opportunity explored the ~7-meter-high Burns Cliff in Endurance Crater [*Grotzinger et al.*, 2005; *Squyres et al.*, 2006], a ~5 m thick section of Burns formation rocks at Erebus Crater [*Metz et al.,* 2009], and a ~10 m thick section at Victoria Crater (~750 m in diameter) [*Squyres et al.*, 2009]. Thus, only a limited stratigraphic section has been characterized in detail using rover-based observations and the estimates of total thickness based on inferences from orbital data vary considerably.

With regard to Burns formation mineralogy, linear unmixing of emission spectra from Opportunity's Mini-TES instrument indicates that the Burns formation outcrops are composed of plagioclase feldspar, hematite, Mg-, Ca-, and Fe-bearing sulfates and opaline silica [*McLennan et al.,* 2005; *Glotch et al.*, 2006]. The Fe-bearing mineralogy of Burns outcrops, derived from Mössbauer spectrometer measurements, is 36% hematite, 29% jarosite, 20% Fe3D3 (an unidentified ferric phase), 14% pyroxene, and 2% olivine [*Morris et al.*, 2006]. A surficial deposit of basaltic sands interspersed with hematitic concretions overlies most of the Burns formation outcrops [*Squyres et al.*, 2004]. The hematite concretions have been concentrated onto the surface as the relatively friable Burns formation sandstones were eroded by wind [*McLennan et al.,* 2005; *Soderblom et al.*, 2004]. *Morris et al.* [2006] classified soils at Meridiani Planum using the Mössbauer Spectrometer onboard Opportunity. In basaltic soils with a low density of hematitic spherules, the distribution of Fe-bearing minerals was 39% pyroxene, 33% olivine, 18% nanophase Fe oxides, 6% magnetite and 4% hematite. Surface deposits of hematitic concretions are inferred to have 21% pyroxene, 20% olivine, 12% nanophase Fe oxides, 4% magnetite and 43% hematite

[*Morris et al.*, 2006]. Hematitic concretions are typically 1-2 mm in diameter, whereas grain sizes of basaltic sands are 50-125 μm [*Sullivan et al*., 2005]. Hematitic concretions tend to be concentrated at the crests of wind-blown ripples by wind-induced surface creep [*Jerolmack et al.*, 2006].

2.3 Data Set Descriptions

Data sets from three orbital imaging systems were used in our study to investigate the morphology, structure, and stratigraphy of Iazu Crater and to make a comparison to the less degraded Yar Crater (Table 2.1). The High Resolution Stereo Camera (HRSC) onboard the Mars Express Orbiter acquires images with a spatial resolution of ~10 m/pixel, and the panchromatic stereo capabilities of the instrument have been used to produce digital terrain models (DTMs) with ~50 m/pixel sampling [*Jaumann et al.*, 2007]. The Context Imager (CTX) aboard the Mars Reconnaissance Orbiter (MRO) acquires panchromatic context images at ~6 m/pixel [*Malin et al.*, 2007]. High-resolution (~0.25 m pixel) panchromatic and multispectral images are acquired by the HiRISE instrument (High Resolution Imaging Science Experiment) on MRO [*McEwen et al.,* 2007]. Iazu Crater is covered by two overlapping sets of HiRISE stereo pairs. DTMs were constructed at ~2 m/pixel postings from these stereo pairs using the Ames Stereo Pipeline [*Moratto et al.,* 2010].

Table 2.1: HiRISE, CTX and HRSC Data Descriptions

	Image	Target	Acquisition date	Center latitude	Center longitude	Solar longitude	Solar incidence angle
HiRISE	ESP_022525_1775	Iazu	17 May 2011	-2.692°	354.791°	294.29°	40.48°
	ESP_022670_1775	Iazu	28 May 2011	-2.693°	354.882°	301.08°	37.69°
	ESP_023092_1775	Iazu	30 June 2011	-2.684°	354.882°	320.23°	34.97°
	ESP_023237_1775	Iazu	12 July 2011	-2.685°	354.789°	326.57°	32.54°
CTX	G11_022525_1776	Iazu	17 May 2011	-2.427	354.75	294.3°	40.59
	D10_031005_2025	Yar	08 March 2013	22.307	320.88	278.2°	60.47
HRSC	H2064_0000_DT4	Iazu	23 August 2005	-4.038	354.74	274°	-

	H5210_0000_DT4	Yar	19 May 2011	22.499	321.418	295°	-

Mineral identifications on Iazu's northern rim and wall were inferred based on analysis of hyperspectral data from the CRISM (Compact Reconnaissance Imaging Spectrometer for Mars) instrument on MRO [*Murchie et al.,* 2007] (Table 2.2). CRISM covers a wavelength range 0.36 – 3.92 μm with 544 spectral channels. The motion of the instrument's gimbaled optical system allows it to acquire targeted images while moving from south to north along MRO's orbit, with the southernmost image row acquired first. The changing distances between CRISM and the targeted surface feature throughout the observation result in the characteristic hourglass shape when the image data are map-projected scenes acquired in a mode in which the gimbaled optics are commanded to acquire data while passing over the targeted feature [*Murchie et al.*, 2007]. Nominal spatial resolution of map-projected full-resolution targeted (FRT) observations is 18 m/pixel. Since 2011, CRISM has also operated in along-track oversampled (ATO) mode, acquiring overlapping pixels in the along-track direction to achieve improved spatial resolution [*Fraeman et al.*, 2013; *Arvidson et al.*, 2014; *Kreisch et al*., 2016]. Mapping to smaller pixel sizes using ATOs (~12 m/pixel) is possible in regions with dense oversampling. CRISM scenes ATO00037D74, ATO0003C0A2 and FRT0001E2AA (Table 2.2), which cover the northern rim and center of Iazu, are used in analyses presented in this paper (Figure 2.2a). Note that FRT0001E2AA is in fact an ATO, but has an FRT prefix because the nomenclature changed after acquisition of this scene. The wavelength ranges between ~0.40–1.0 μm (CRISM 'S' data) and ~1.0–2.65 μm (CRISM 'L' data) were used for this paper, thereby avoiding the thermal contributions at longer wavelengths. To provide a regional-scale view FRT0001F098 and FRT0001E4BE acquired using only the S detector are also used in this paper (Table 2.2).

Table 2.2: CRISM Data Descriptions. Note that FRT0001F098 and FRT0001E4BE I/F cubes were used without DISORT processing and are employed for color context only.

	FRT0001E2AA	ATO00037D74	ATO0003C0A2	FRT0001F098	FRT0001E4BE
Acquisition date	2011-05-17	2015-08-23	2016-05-13	2011-07-12	2011-05-28
Center latitude	-2.633°	-2.654°	-2.674°	-2.811	-2.854
Center longitude	354.819°	354.829°	354.841°	354.821	354.918
Solar longitude	294.3°	31.38°	151.85°	326.5°	301.1°
Dust aerosol opacity	0.50	0.67	0.50	-	-
Ice aerosol opacity	0.10	0.10	0.10	-	-
Incidence angle	40.47°	43.95°	50.73°	32.5°	37.7°
T detector	-144°	-148°	-148°	-57°	-53°
Delta λ	0.4338 nm	-0.9 nm	-0.296 nm	-	-

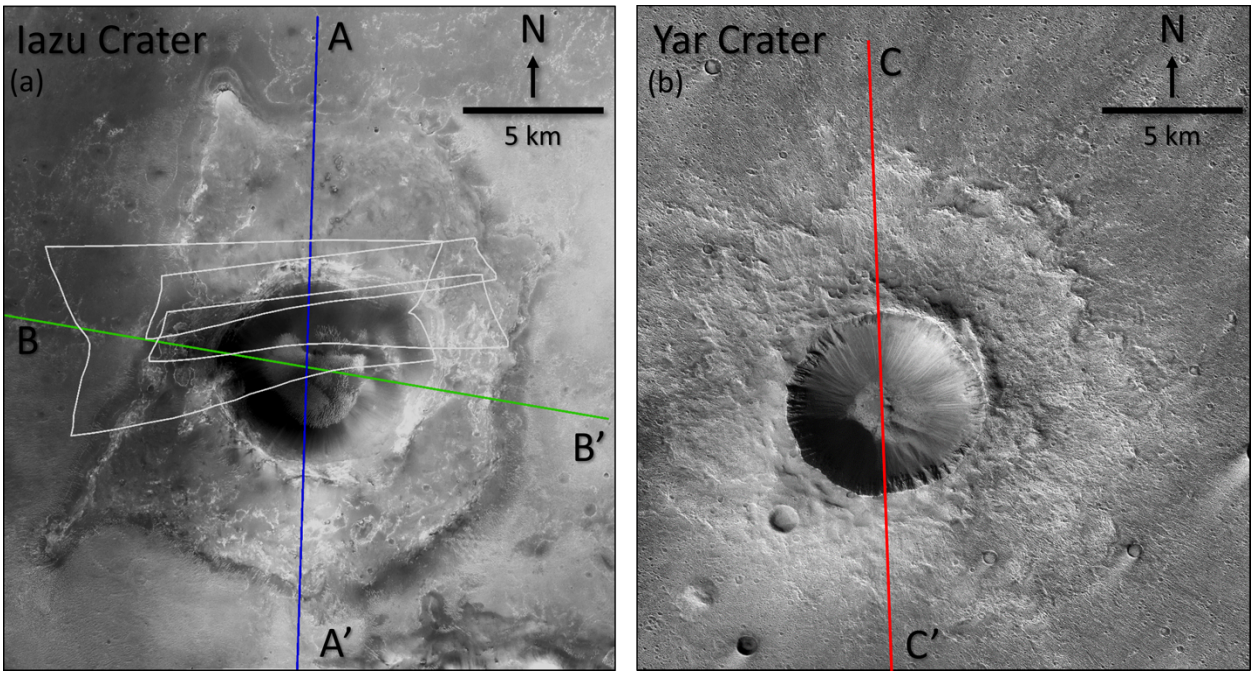

Figure 2.2: Iazu and Yar are two impact craters of similar size with different morphologic characteristics. Colored lines correspond to topographic profiles plotted in Figure 2.3. (a) Iazu Crater and its raised, butterfly-shaped ejecta deposit and relatively subdued, irregular rim. Iazu is located at 2.71°S, 354.8°E. CTX G11_022525_1776 with footprints of CRISM scenes FRT0001E2AA, ATO00037D74 and ATO0003C0A2 overlaid. (b) Yar crater with its symmetrical ejecta deposit, raised rim, and bowl-shaped interior (CTX D10_031005_2025). Yar is located at 22.27°N, 320.85°E.

CRISM data were converted to single scattering albedos (SSA), defined as the ratio of power scattered to total power removed by both scattering and absorption [*Hapke*, 2012], following a processing procedure similar to *Arvidson et al.* [2014]. SSA estimates were retrieved from CRISM I/F (radiance on sensor divided by solar radiance at the heliocentric distance for the observation of interest) data using the DISORT radiative transfer code [*Stamnes et al.,* 1988] to model aerosol scattering and absorption. The Hapke model was used for surface scattering with a modestly forward-scattering two-term Henyey-Greenstein single particle phase function that best removed shading variations between incoming and outgoing portions of the scene for FRT0001E2AA. Specifically, the asymmetry factor was set to 0.09 and the forward fraction to 0.0. Gas bands were removed using the volcano scan correction procedure [e.g., *McGuire et al*., 2009]. SSA values are dependent on the optical constants of materials and physical properties such as grain size, and are independent of lighting and viewing conditions. Initial atmospheric dust and ice aerosol optical depths were derived from climatology estimates and adjusted until plains terrain to the west of Iazu showed similar SSA spectra for the overlapping areas in the three scenes. Details are provided in Table 2.2. Local incidence and emergence angles used in the SSA retrievals are based on MOLA-generated topography, with corrections for atmospheric path lengths and opacities.

Retrieved SSAs for the ATO observations were regularized using a log maximum likelihood method (MLM) detailed in *Kreisch et al.* [2016]. A median filter was first applied to remove large spikes that correspond to extreme noise excursions. The MLM procedure uses the CRISM spatial and spectral transfer functions to retrieve the best estimates of SSA values in the presence of Poisson-dominated noise. The images were regularized using a convex penalty

function to deemphasize local deviations from surrounding values, given that inversion of transfer functions is inherently unstable. The regularized images were map projected to 12 m/pixel.

2.4 Impact Cratering Mechanics and Morphology

Iazu falls morphologically into the simple crater class, but with an eastern side that bulges outward (Figure 2.2a). To illustrate some of the unusual morphological features of Iazu, we compare it to Yar Crater (Figure 2.2b), a fresh Martian crater ~6.1 km in diameter in Chryse Planitia (22.27°N, 320.85°E). Yar was selected for comparison by examination of a global Martian crater database [*Robbins and Hynek,* 2012a] for fresh-appearing, simple morphology craters that are approximately the same diameter as Iazu, and covered with sufficient orbital data to facilitate detailed morphologic and topographic comparisons. Both craters have diameters near the Martian simple-complex crater transition [*Robbins and Hynek*, 2012b]. HRSC-based DTMs (Figure 2.3) show that both craters lack a central peak, terraced walls, and flattening of the crater floor. Iazu's northern, western, and southern rim stand at a relatively constant elevation, varying between approximately -1720 to -1750 m. In contrast, Iazu's northwest rim exhibits a 50° wide, saddle-shaped gap that is ~150 m lower than the rim segments to the north and south (Figure 2.4). On the other hand, Yar has a well-defined and continuous rim with little topographic deviation.

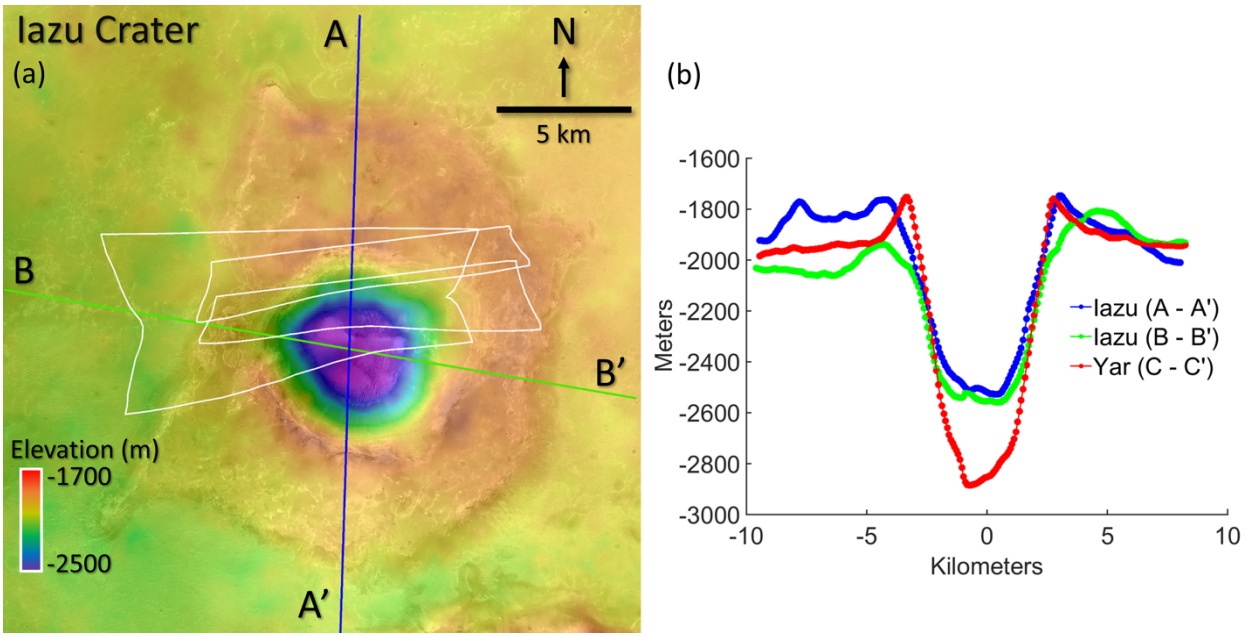

Figure 2.3: (a) Color-coded elevations over CTX image G11_022525_1776, showing Iazu and its elevated ejecta deposit. (b) Topographic profiles of Iazu Crater compared to Yar Crater, which is ~700 m smaller in diameter, and 350 m deeper. Blue: Iazu profile aligned approximately north to south (see Figure 2.2a), showing the maximum height of the crater rim. Green: Iazu profile aligned approximately west to east, showing lower elevations resulting from the western rim gap and eastern bulge of the crater (see Figure 2.2a). Red: Yar Crater profile aligned approximately north to south (see Figure 2.2b). Elevations were offset so that the rim of Yar is shown at the same elevation as the rim of Iazu. Profiles were derived from HRSC DTMs h2064_0000_dt4 (Iazu) and h5210_0000_dt4 (Yar) (Table 2.1). Elevations are relative to the MOLA-based areoid.

Iazu is surrounded by an ejecta deposit that stands 60-150 m above the surrounding plains (Figures 2.2a; 2.3a). The ejecta deposit is higher to the north of the crater than to the south, forming sharp cliffs on some of the deposit's distal edges. The deposit is a rugged plateau, likely formed as a consequence of a more resistant surface than that of the surrounding Burns formation outcrops that dominate the rocks underlying the Meridiani plains. Differential wind erosion is interpreted to have formed the ejecta plateau, with erosion of the plains rocks occurring at a faster rate than in to the materials dominating the ejecta deposit.

The planform of Iazu's raised ejecta is strongly asymmetrical, in that it is sharply truncated on the western side and elongated in the northern and southern directions (~3.7 and 3.1 km from the crater rim, respectively) compared to the eastern to western directions (~2.0 km) (Figure 2.2a).

Although crater shapes remain circular (rather than elliptical) for impact angles above 10-15 degrees above the surface, ejecta patterns show distinct asymmetries at higher angles. *Herrick and Hessen* [2006] studied the statistics of inferred oblique impact populations on Mars, and concluded that a preferential deposition of ejected material in the cross-range direction occurs for impact angles below ~35 degrees from horizontal, thereby indicating direction of impact. A "forbidden zone" of ejecta develops uprange at angles less than 30 degrees [*Poelchau and Kenkmann*, 2008]. At angles less than 20 degrees, an additional forbidden zone forms downrange, resulting in a "butterfly" pattern [*Poelchau and Kenkmann*, 2008]. In this context we infer that Iazu was formed by an impactor entering from the west at an angle between 20-30 degrees above the surface (Figure 2.4). The unusual shape of the crater, with its eastern bulge, may be the result of an impactor that broke apart late in its low-angle entry, forming part of a second, almost co-located crater. By way of contrast, Yar has a radially symmetric ejecta deposit consistent with formation by a high angle impactor.

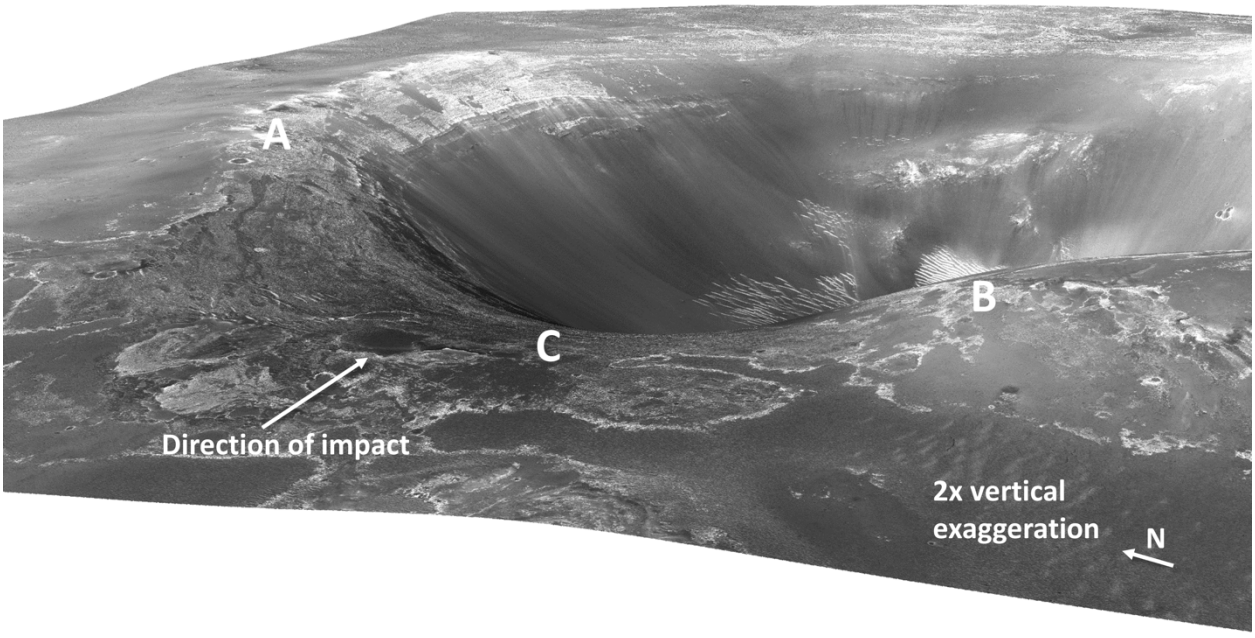

Figure 2.4: Perspective view looking east through the rim gap of Iazu crater, constructed from HiRISE data (Table 2.1) covering the eastern and western sides of the crater. Elevations are 2x vertically exaggerated. Note the bright outcrops on the northern rim and wall. The distance between points A and B is 3.4 km. The change in elevation between points A and B is 150 m, and between points B and C is 120 m.

Comparisons of topographic profiles for Iazu and Yar shows that Iazu's rim is more subdued and rounded as compared to Yar's rim (Figure 2.3b). The height of Iazu's rim relative to the surrounding ejecta deposit is ~80 m, whereas Yar's rim rises up to ~150 m above its ejecta deposit. This comparison suggests that up to a ~70 m of erosion have lowered and rounded Iazu's rim since its formation. This is, of course, a crude estimate because the rock properties may be quite different between the two craters. Also, Iazu is 750 m deep as measured from highest rim segment to floor, with a depth-diameter ratio of ~1:9. Although Yar has a slightly smaller diameter than Iazu, it is 1100 m deep, with a depth-diameter ratio of ~1:5.5. Iazu is thus ~32% shallower than Yar, consistent with the presence of rim erosion and deposition of material by mass wasting and wind within the interior of Iazu. The sets of streaks extending from the walls into the interior of Iazu are consistent with downhill transport, and the presence of wind-blown ripples on the crater

floor indicates wind has also been involved in depositing materials within the crater (Figures 2.4, 2.5).

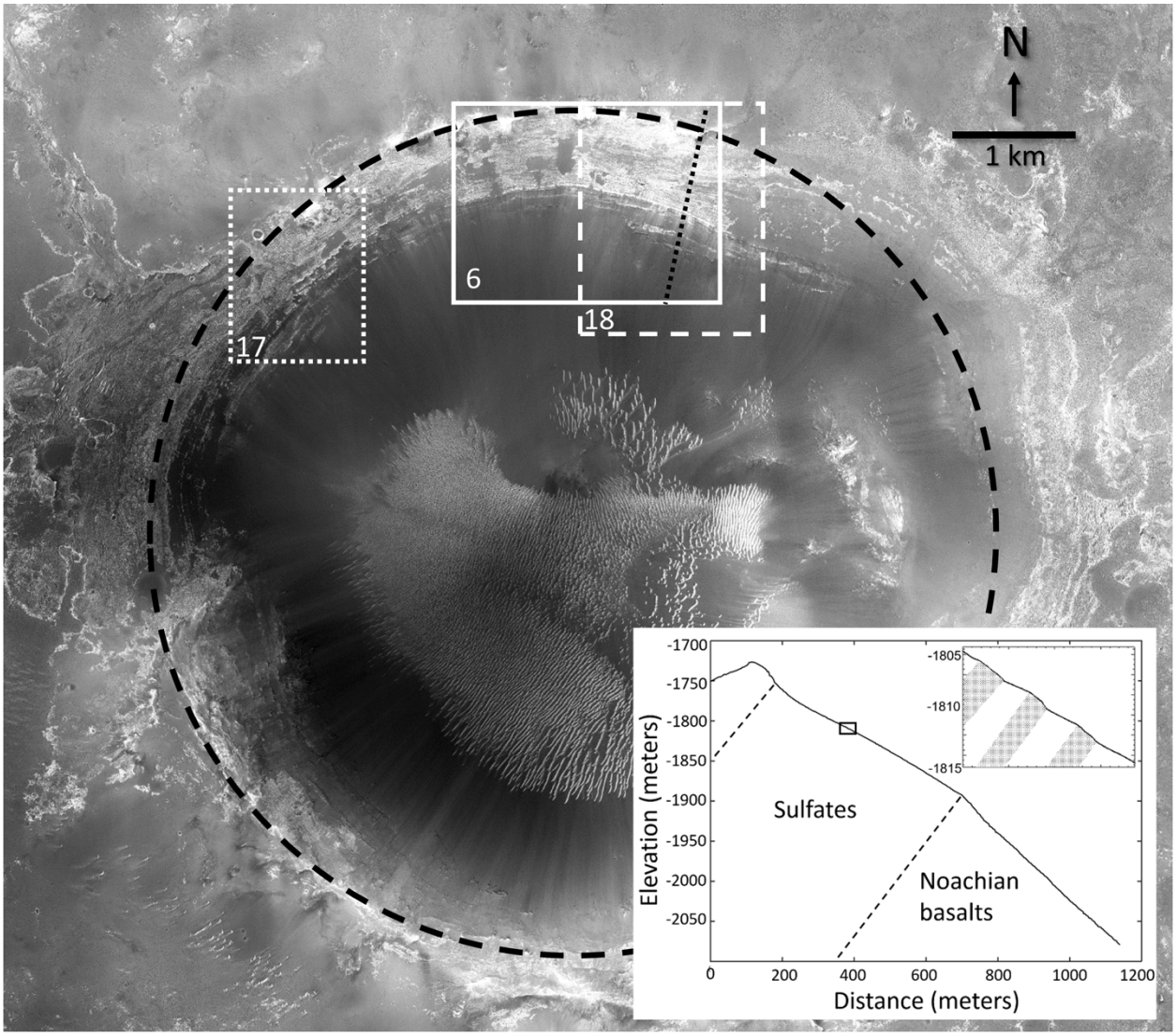

Figure 2.5: Mosaic of HiRISE observations ESP_022525_1775 and ESP_022670_1775 showing that Iazu Crater has a bulged eastern wall, interpreted to be a consequence of an oblique impact. The crater walls show streaks indicative of downhill movement of material, and the partially infilled crater floor is covered by wind-blown ripples. Boxes show the locations of Figures 2.6, 2.17 & 2.18, and the dashed line is a circle centered on Iazu with a diameter of 6.8 km. The dotted line shows the location of the topographic profile in the inset. Inset: HiRISE-derived topographic profile of Iazu's upper wall. A change in slope occurs at the base of the bright outcrops. As shown in Figure 2.6, in HiRISE the bright outcrops can be resolved into banded bright and dark layers. The dark layers have steeper exposures than bright layers based on detailed examination of elevation data.

The northern wall of Iazu exposes a section of banded bright and dark strata with an outcrop slope of 15˚ from the horizontal and a vertical relief of ~150 m (Figures 2.5, 2.6). The lower section

of the banded strata terminates at a break in slope with a 20˚ value below the break and an onset of a set of dark ridges with isolated banded bright and dark strata just above the ridges. The lower section of banded strata and underlying rocks are interpreted to consist of uplifted, relatively intact layers, whereas the upper section is interpreted to be overturned ejecta deposits [*Melosh*, 1989]. The hinge line defines the lower extent of overturned materials, allowing an estimate of the thickness of the section before the impact. Locating the hinge line for Iazu is challenging. The strike and dip of the strata cannot be determined from orbital data alone because 3D exposures of bedding planes are lacking. In addition, there are sets of faults cutting through the deposits (Figure 2.6). Consideration of cratering mechanics and examination of terrestrial examples, such as Meteor Crater, Arizona [*Shoemaker et al.*, 1963] indicate that the hinge line should be located approximately equidistant between the rim and bottom of the intact and uplifted strata. Because it is impossible to completely define the extent of rim erosion the hinge line is assumed to be located at the boundary above which strata are disrupted (Figure 2.6), which is roughly in the middle of the bright strata. Assuming a dip of 40˚ for the intact strata, based on measurements at Meteor Crater [*Kumar and Kring*, 2008], the dip-corrected thickness of the intact portion of the bright outcrops would be ~115 m from the inferred hinge line to the underlying dark ridge and associated increased wall slope.

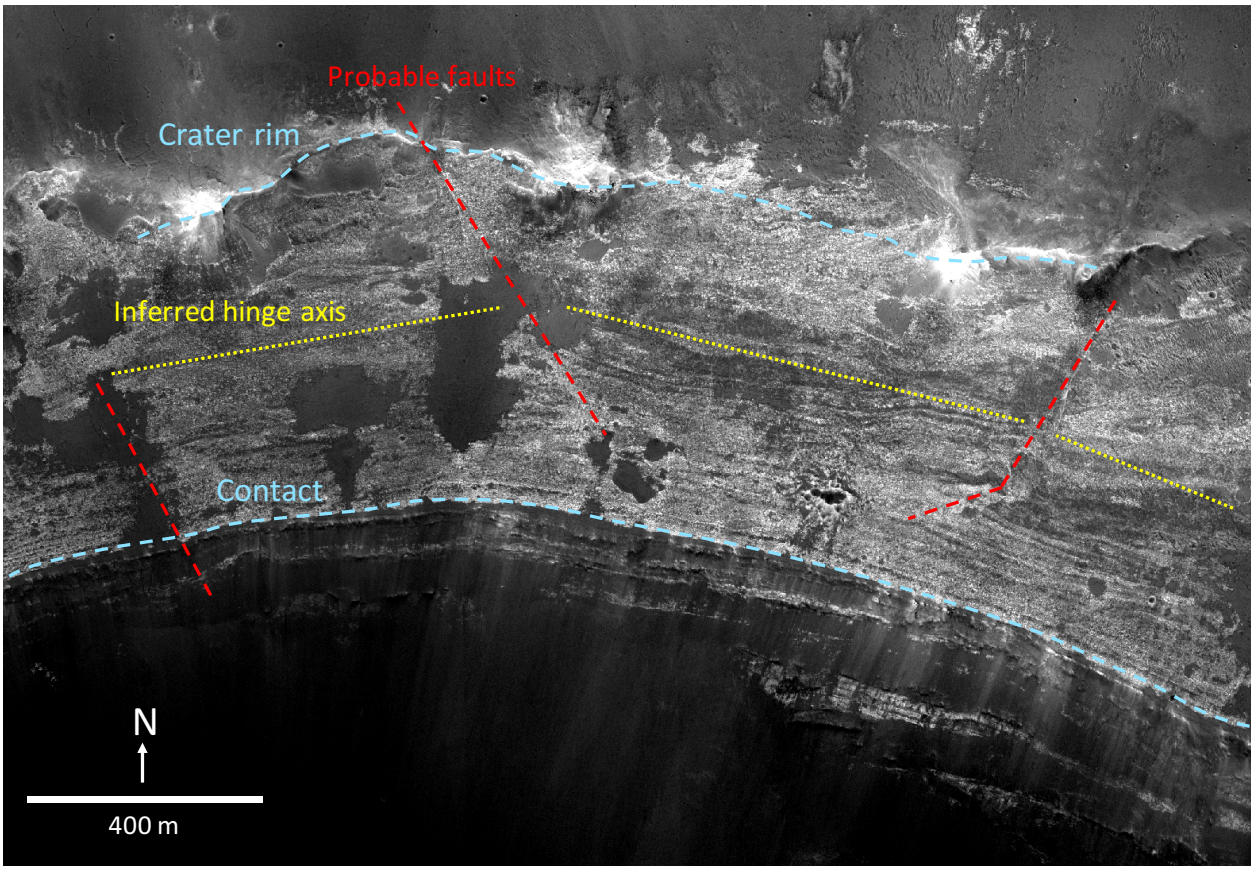

Figure 2.6: Section of the northern wall of Iazu Crater (see Figure 2.5 for location), showing inferred hinge line (yellow) demarcating overlying overturned ejecta deposits above uplifted but relatively intact strata. Contiguous layers are traceable below this line. Major inferred fault locations and the rim crest are also shown. The contact between bright layers and underlying darker materials is also noted.

2.5 Mineralogy of Iazu's Rim and Wall Deposits

As noted, FRT0001F098 and FRT0001E4BE were acquired in the normal sampling mode over Iazu using the S spectrometer only. These two scenes shown as false color composites provide an overview of the color patterns for Iazu and the surrounding plains, together with showing the locations of the ATOs used in this paper (Figure 2.7). The ATO that covers the greatest areal extent with the full CRISM wavelength region is FRT0001E2AA (Figure 2.8). We examined this scene in conjunction with HiRISE data to compare the mineralogy of the rim and wall deposits exposed within Iazu with the mineralogy of the ejecta deposits and surrounding plains. We then used the two highly oversampled and thus high spatial fidelity ATOs to investigate in more detail the

mineralogy of Iazu's northern rim and walls. A powerful method of mapping mineralogy is the use of spectral parameters, as detailed by *Viviano-Beck et al.*, [2014]. For our work we generated indices that map the presence and relative strengths of absorptions indicative of hematite, low calcium pyroxene, high calcium pyroxene, hydrated phases, hydrated sulfate minerals, and smectites, as detailed in Table 2.3. In each case, parameter ranges were set to show the range of values evident in the data. Parameter maps for FRT0001E2AA are shown in Figures 2.9-2.13. ATO00037D74 and ATO0003C0A2, projected to 12 m/pixel, show detailed color and morphologic patterns that are not as evident in FRT0001E2AA (Figure 2.15). Type spectra from FRT0001E2AA for spatial regions with high parameter values are shown in Figure 2.14; spectra with absorptions indicative of hydrated sulfates and smectites from ATO00037D74 are shown in Figure 2.16. Spectra were retrieved from spatially contiguous regions, drawn from pixels with parameter values in the upper 10% of the total range.

Table 2.3: CRISM Spectral Parameters. Formulations from *Viviano-Beck et al.*, 2014. R- reflectance; RC-continuum-removed reflectance; RB= (RC-R)/RC; a = 1-b; b= $(\lambda_c-\lambda_s)/(\lambda_L-\lambda_s)$, where λ_c is the center wavelength and λ_L and λ_s are used to fit a continuum.

Parameter name	Formula	Parameter measured	Rationale
BD860_2	$1-\left(\frac{R860}{a*R755+b*R977}\right)$	Band depth at 0.86 μm	Select crystalline ferric minerals (especially hematite)
LCPINDEX2	$R1690*0.20 + RB1750*0.20 + RB1810*.030 + RB1870*0.30$	Broad absorption centered at 1.81 μm	Pyroxene, favoring low-Ca pyroxene
HCPINDEX2	$RB2120*0.10 + RB2140*0.10 + RB2230*0.15 + RB2250*0.30 + RB2430*0.20 + RB2460*0.15$	Broad absorption centered at 2.12 μm	Pyroxene, favoring high-Ca pyroxene
BD1900R2_2	$1-\frac{\left(\frac{R1908}{RC1908}+\frac{R1914}{RC1914}+\frac{R1921}{RC1921}+\frac{R1928}{RC1928}+\frac{R1934}{RC1934}+\frac{R1941}{RC1941}\right)}{\left(\frac{R1862}{RC1862}+\frac{R1869}{RC1869}+\frac{R1875}{RC1875}+\frac{R2112}{RC2112}+\frac{R2120}{RC2120}+\frac{R2126}{RC2126}\right)}$	Band depth at 1.9 μm	Hydrated minerals

SINDEX_2	$1-\left(\frac{a*R2120+b*R2400}{2*R2290}\right)$	Convexity near 2.3 µm	Hydrated sulfates
D2300	$1 - \left(\frac{\frac{R2290}{RC2290}+\frac{R2320}{RC230}+\frac{R2330}{RC2330}}{\frac{R2120}{RC2120}+\frac{R2170}{RC2170}+\frac{R2210}{RC2210}}\right)$	Dropoff at 2.3 µm	Fe-OH and Mg-OH absorptions in smectites

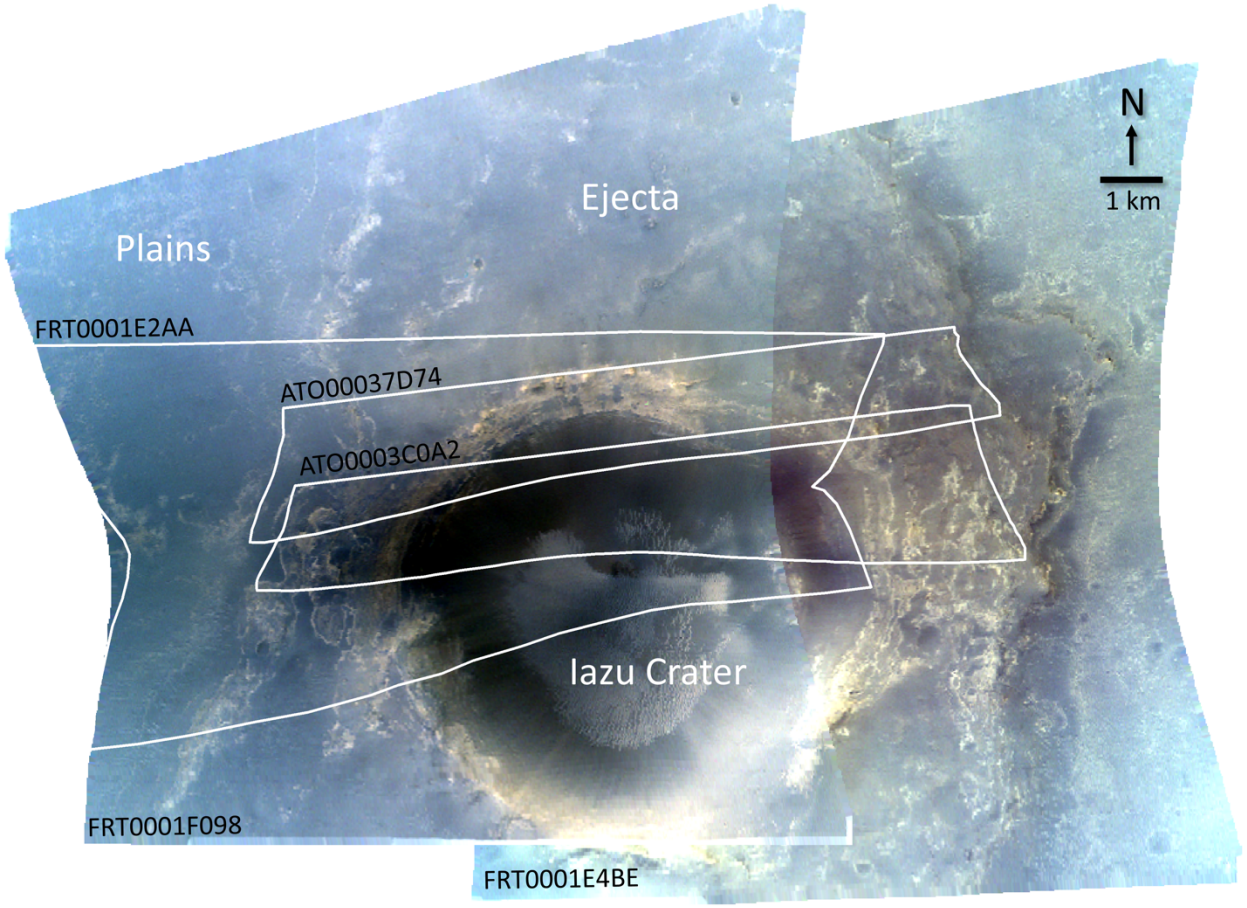

Figure 2.7: CRISM S data mosaic of FRT0001F098 and FRT0001E4BE projected at 18 m/pixel, showing Iazu Crater in its entirety and a portion of its ejecta deposit and surrounding Meridiani plains (R = 0.71, G = 0.60, B =0.53 µm). White lines are footprints of CRISM along-track oversampled observations FRT0001E2AA, ATO00037D74 and ATO0003C0A2, also shown in Figure 2.9-2.13.

The plains color signature is similar to what is found on Meridiani plains in general with relatively dark surfaces interspersed with bright outcrops (Figure 2.8). The plains spectral

signature has a positive slope from 1-1.6 μm, is relatively featureless at longer wavelengths, and has the same overall shape as the spectral signature of the plains to the west of Endeavour (Figure 2.4) [*Arvidson et al.,* 2006, Figure 2.7]. The plains deposits surrounding Iazu are interpreted to be equivalent to what Opportunity has found covering large portions of Meridiani Planum, i.e., basaltic sands mixed with hematitic concretions and a minor amount of dust, with dispersed outcrops of Burns formation rocks [*Arvidson et al.,* 2006].

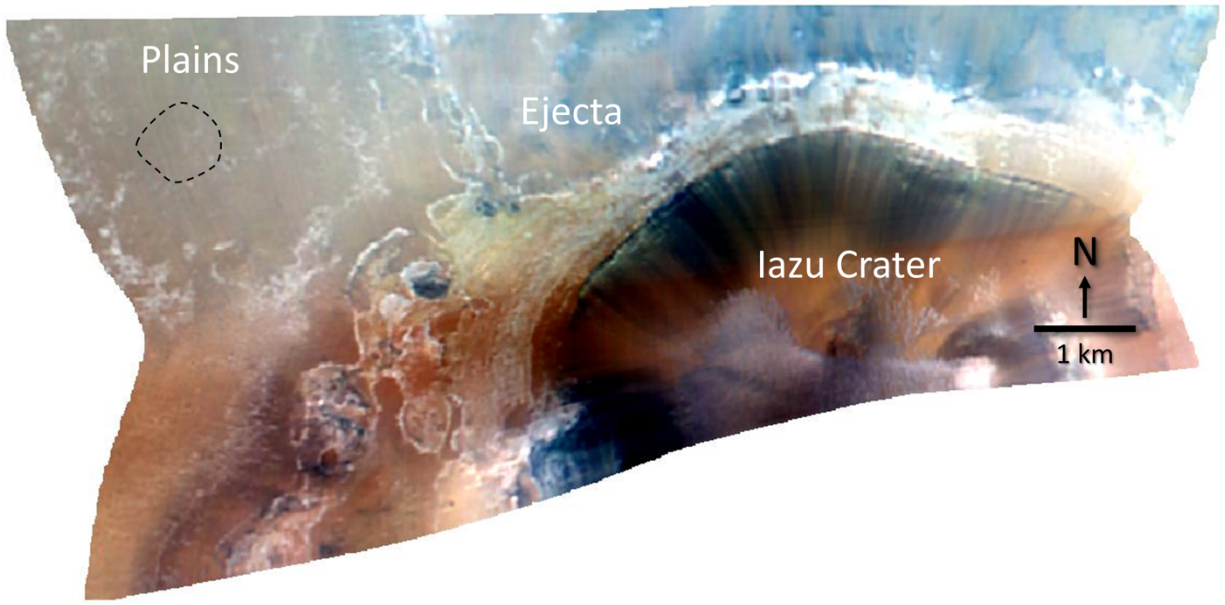

Figure 2.8: FRT0001E2AA 'L' data (R =2.53, G=1.51, B=1.06 μm) covering part of the crater interior, ejecta, and surrounding plains. This observation was used to generate parameter maps in Figures 2.9-13. Dashed region is the source of the plains type spectrum shown in Figure 2.14.

The materials concentrated in the western saddle-shaped gap in Iazu display a particularly strong positive slope towards from ~1 to 1.6 μm (Figure 2.14), in addition to showing high values in the BD860_2 parameter map (Figure 2.9). Continuum-removed spectra illustrate the hematite absorption centered near ~0.86 μm. These materials are interpreted to be hematitic concretions concentrated within the gap by differential transport as winds have blown Meridiani sands into the crater.

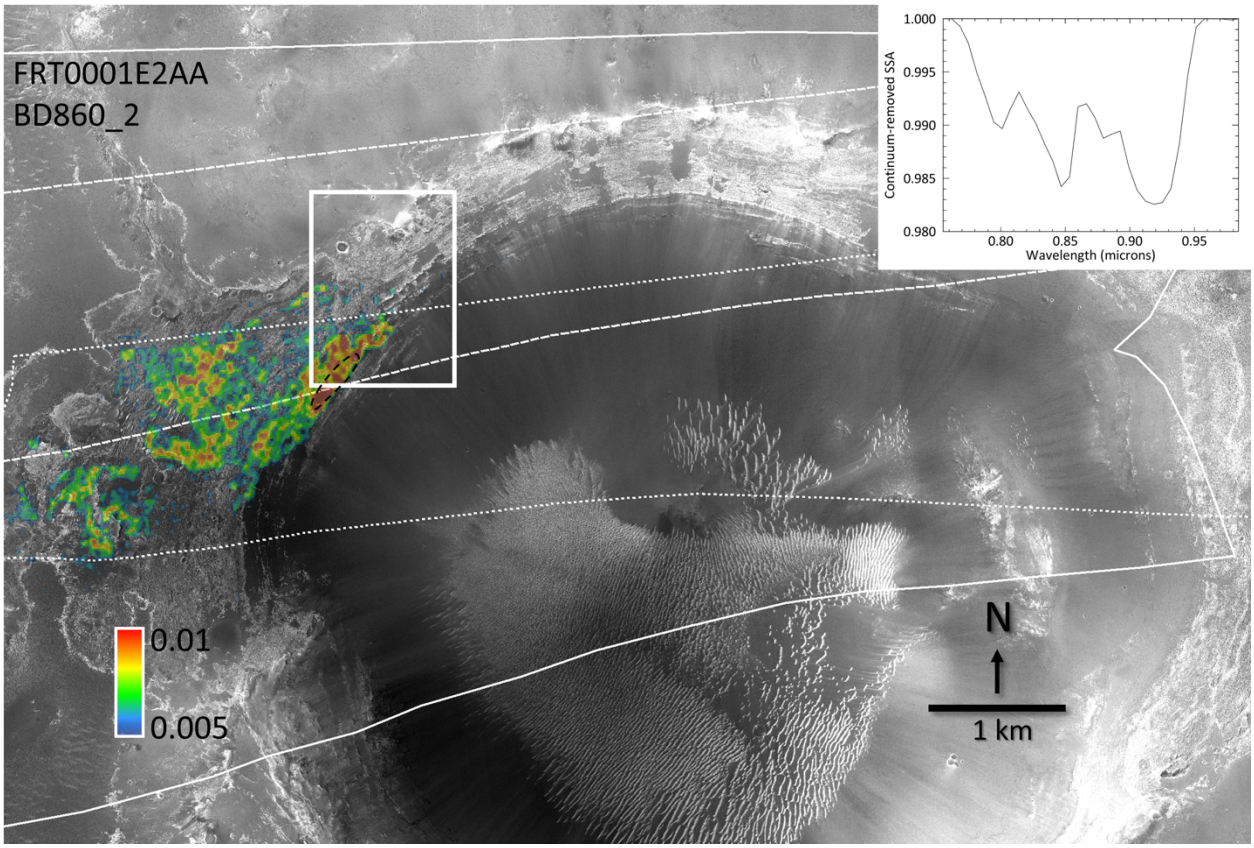

Figure 2.9: BD860_2 parameter map indicative of hematite and derived from FRT0001E2AA overlaid onto HiRISE-based mosaic. This parameter measures an absorption at 0.86 µm. The relatively high hematite concentrations show an affinity for the rim gap. White box indicates the area shown in Figure 2.17. Dashed line is the high concentration area from which the rim gap type spectrum in Figure 2.14 is derived. This type spectrum is shown continuum-removed in the upper right of this figure.

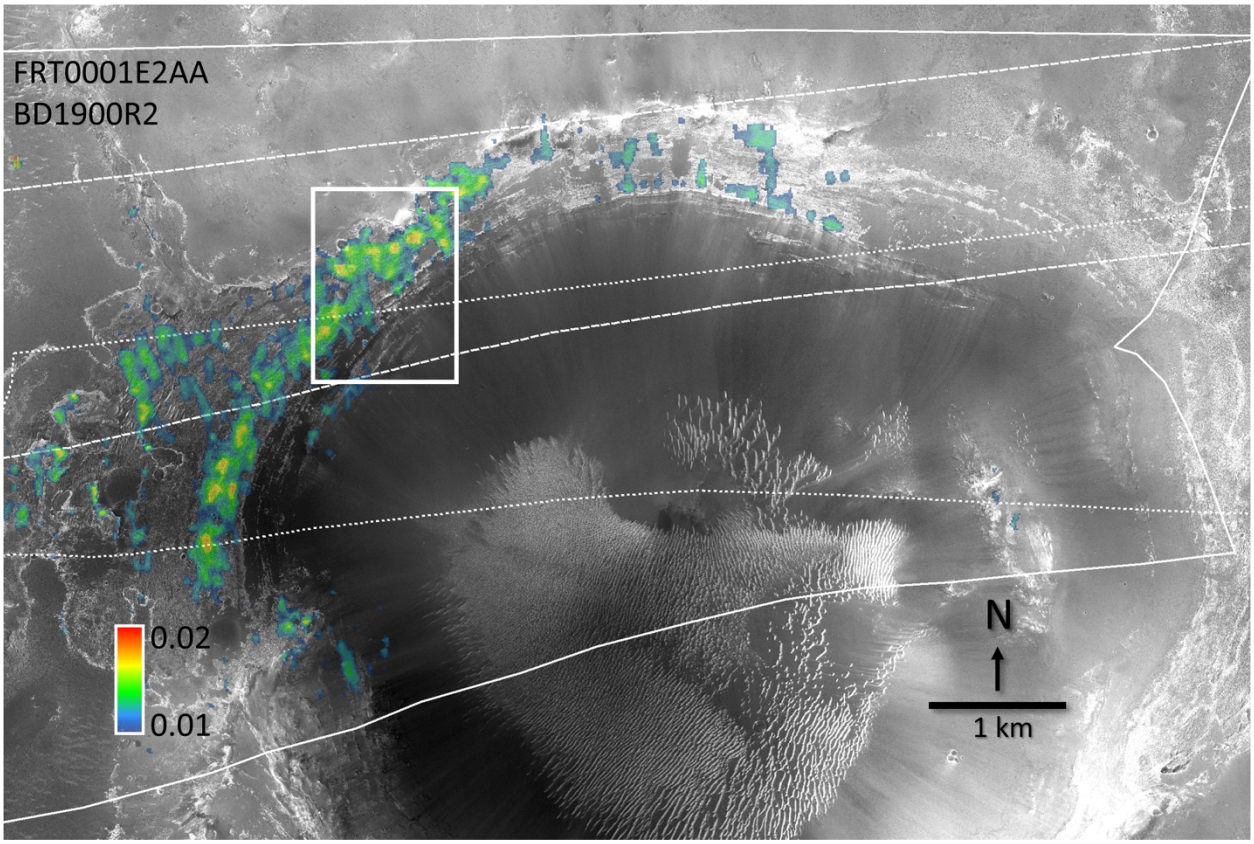

Figure 2.10: BD1900R2 parameter map indicative of surface hydration and derived from FRT0001E2AA overlaid on HiRISE-based mosaic. The absorptions are due to OH and H_2O combination bands and correspond to regions interpreted to be Burns formation strata. White box indicates the area shown in Figure 2.17.

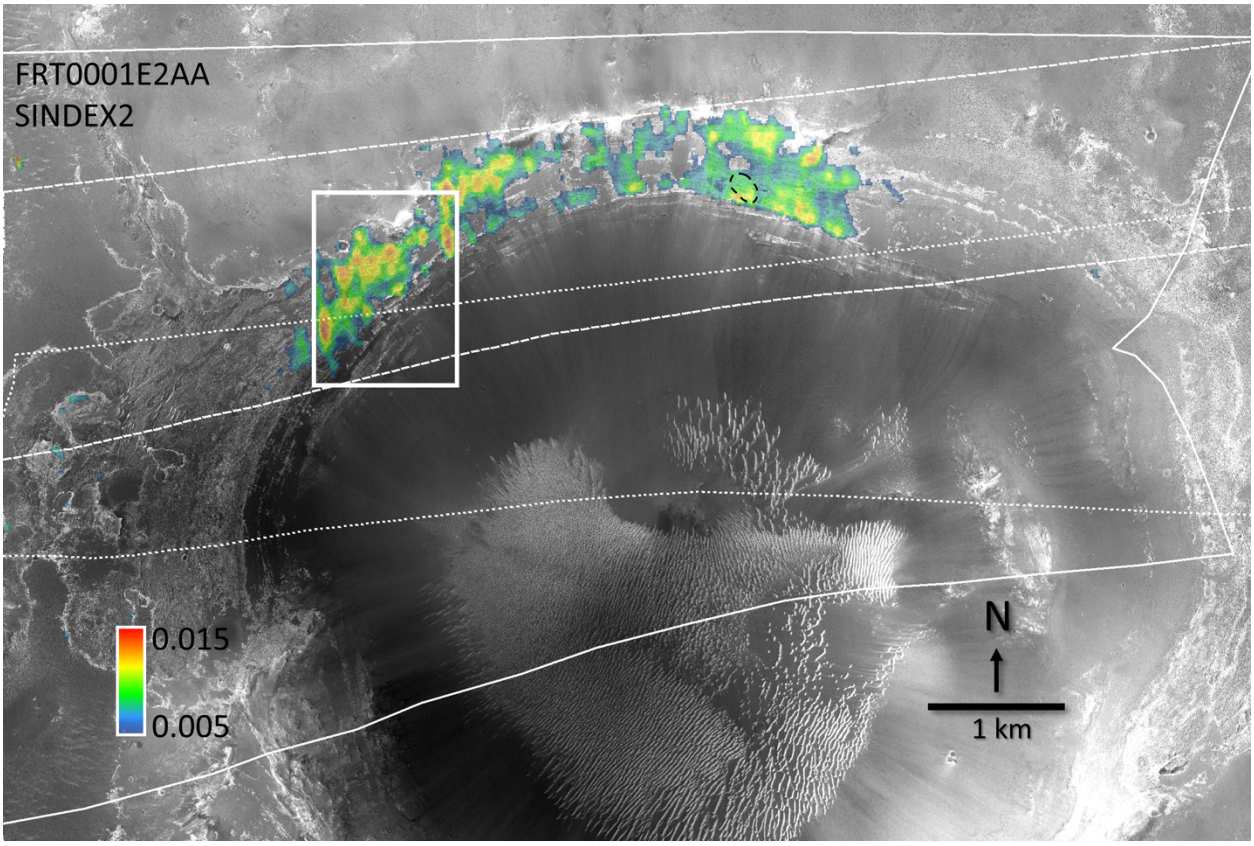

Figure 2.11: SINDEX2 parameter map indicative of hydrated sulfate minerals and derived from FRT0001E2AA overlaid on HiRISE-based mosaic. This parameter measures a convexity between 2.1 µm and 2.4 µm and maps to exposures of Burns formation outcrops. White box indicates the area shown in Figure 2.17. Dashed line is the high concentration area from which the Burns formation type spectrum shown in Figure 2.14 is derived.

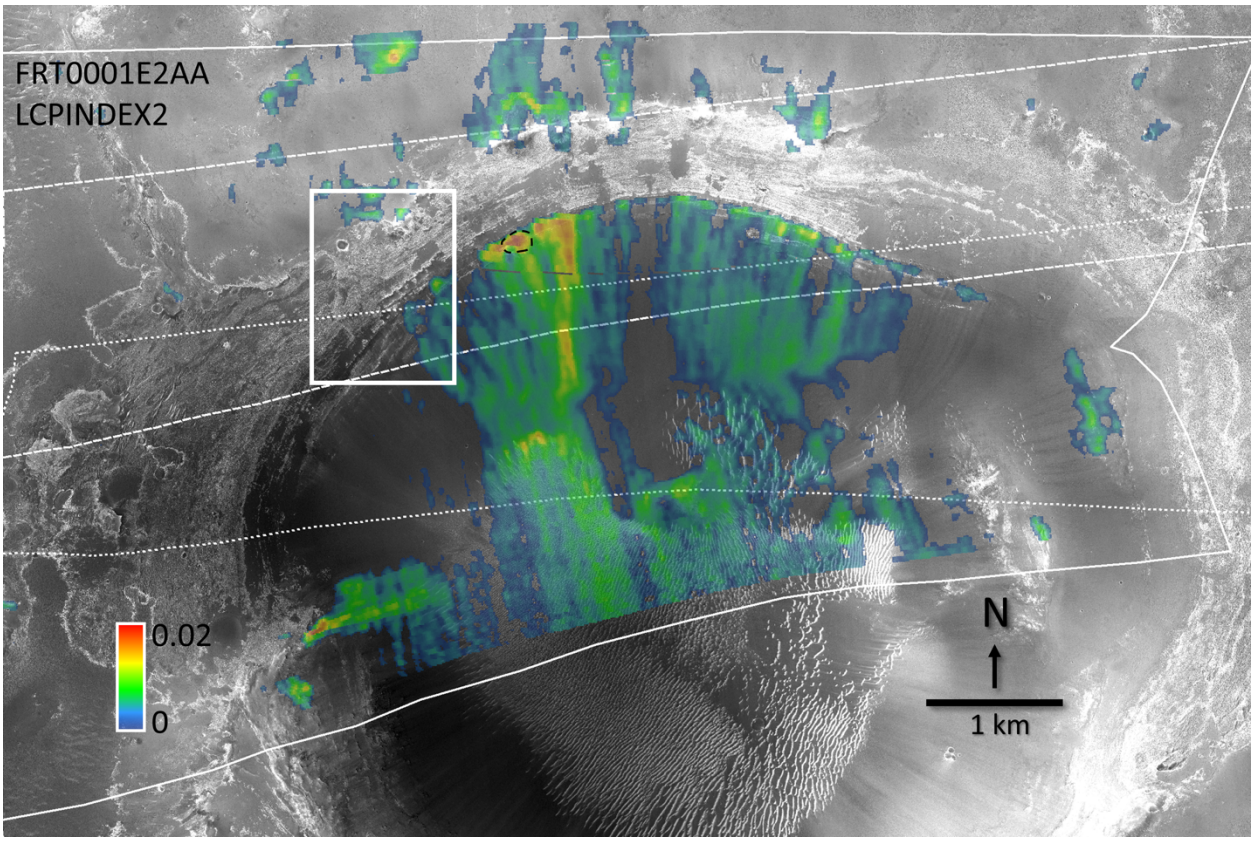

Figure 2.12: LCPINDEX2 parameter map indicative of low-calcium pyroxene. LCP is present in the crater interior and ejecta and avoids the bright strata on the upper part of the walls. Relatively high concentrations are associated with exposed bedrock on steep surfaces near the contact with the overlying hydrated sulfate strata. White box indicates the area shown in Figure 2.17. Dashed line is the high concentration area from which the type spectrum associated with outcrops beneath the contact, shown in Figure 2.14, is derived.

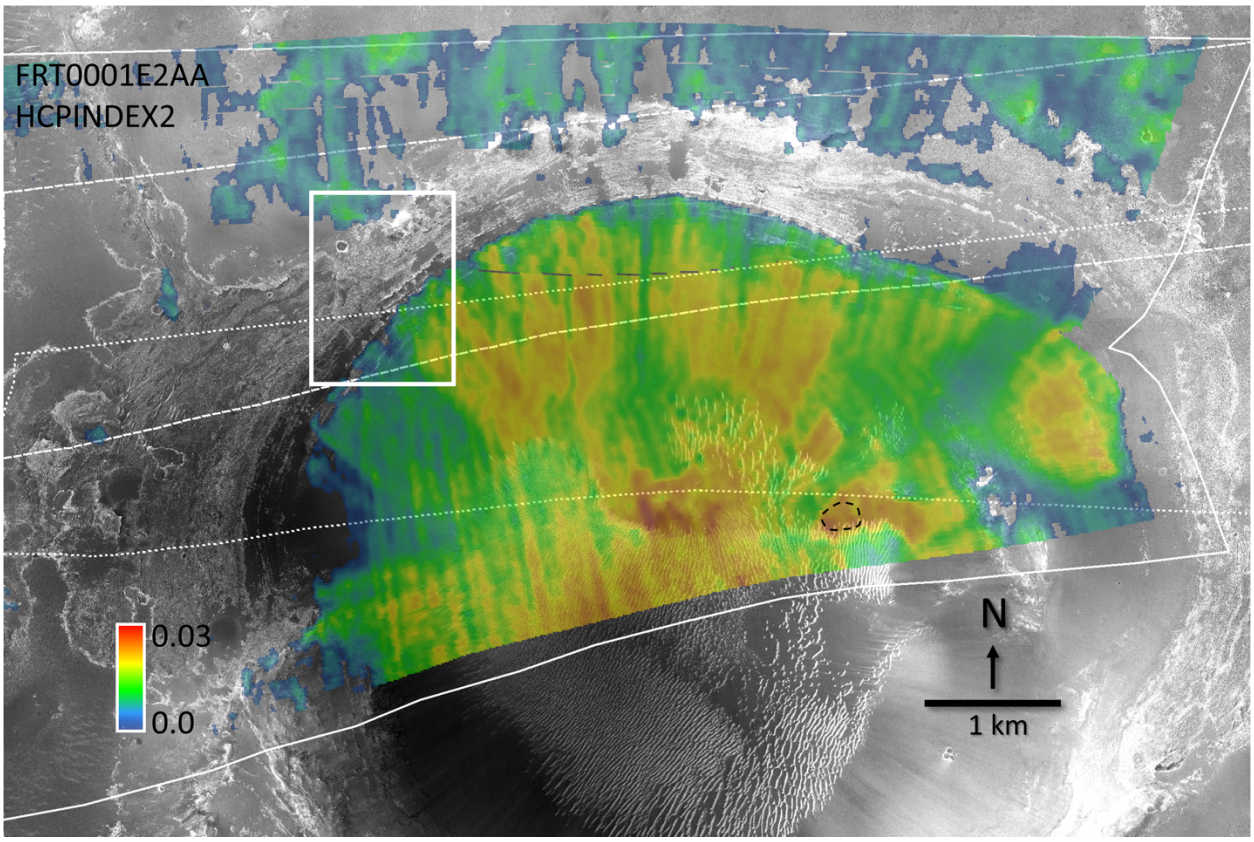

Figure 2.13: HCPINDEX2 parameter map indicative of high-calcium pyroxene. HCP is concentrated within the crater walls and floor and avoids the hydrated sulfate strata interpreted to be Burns formation outcrops. White box indicates the area shown in Figure 2.17. Dashed line is the high concentration area from which the crater floor debris type spectrum in Figure 2.14 is derived.

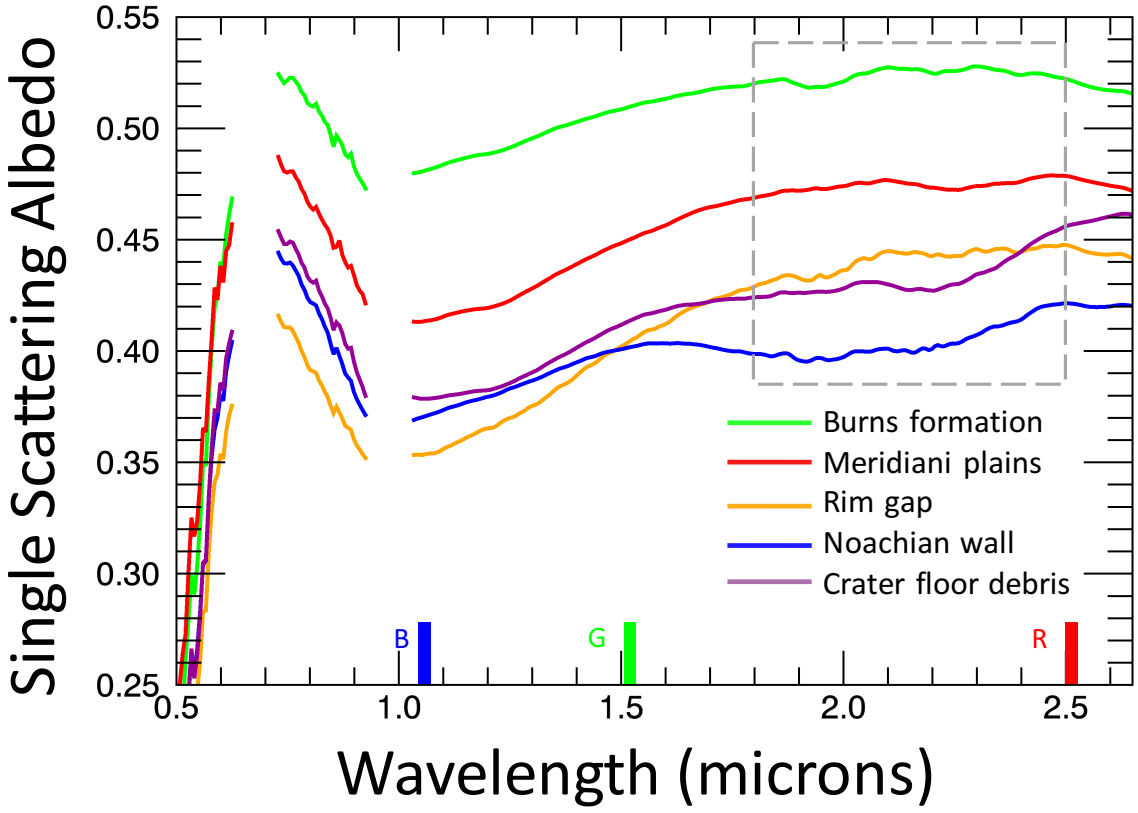

Figure 2.14: CRISM type spectra of major lithologic units in and near Iazu Crater. Green – sulfate-bearing Burns formation, upper wall of Iazu Crater. Red – Meridiani plains west of Iazu. Orange – hematite-bearing rim gap. Purple – HCP-bearing debris on Iazu's floor. Blue – LCP in the Noachian wall of Iazu. See text for further description of units. Lines on the bottom axis indicate R,G,B bands used in Figure 2.8. White box delineates spectral range for Burns formation outcrops show in detail in Figure 2.16.

As noted in the previous section of this paper, banded outcrops dominate the upper wall and rim of Iazu, and a break in slope and ridge delineates the change to relatively dark ridges with isolated banded strata below (labelled as 'Contact' in Figure 2.6). The banded outcrops exhibit a strong negative slope beyond 2 μm and show relatively high values in the BD1900R2 and SINDEX2 parameter maps [*Viviano-Beck et al.*, 2014] (Table 2.3). BD1900R2 measures the band depth at 1.9 μm, an indicator of OH/H_2O combination absorptions. SINDEX2 identifies hydrated sulfates (monohydrated and polyhydrated) based on convexity at 2.3 μm due to H_2O and OH absorptions at shorter and longer wavelengths [*Viviano-Beck et al.,* 2014].

The SINDEX2 parameter maps derived from ATO00037D74 and ATO0003C0A2 are shown in Figure 2.15. Retrieving spectra from BD1900R2 and SINDEX2 parameter maps with high values shows the presence of polyhydrated sulfates, based on a 1.9 μm absorption due to the bending and stretching combination absorptions of H_2O and OH, as well as a 2.4 μm absorption due to S-O bending or OH/H_2O combinations or overtones (Figure 2.16) [*Cloutis et al.*, 2006]. The spectra also exhibit a downturn beyond 2.5 μm due to OH and H_2O stretching fundamentals near 3 μm [*Cloutis et al.*, 2006]. We cannot attribute this signature to one or more specific polyhydrated sulfates. Possibilities include several varieties of Mg sulfates, which are difficult to distinguish from one another using this wavelength region alone [*Crowley*, 1991]. We do not observe a 2.1 μm absorption that would indicate monohydrated sulfates such as kieserite ($MgSO_4 \cdot H_2O$) or szomolnokite ($FeSO_4 \cdot H_2O$) [*Cloutis et al.*, 2006]. Further, evidence is lacking for Fe-rich polyhydrated sulfates, which would show Fe-related electronic features at shorter wavelengths, or for Ca-rich hydrated sulfates (namely gypsum or bassanite) which would show additional vibrational features between 1.5-2.5 μm. Given that Opportunity found Burns formation sulfate-rich sandstones ~25 km to the north as the rocks that underlie the Meridiani plains, and Iazu impacted into the plains and exposed banded hydrated sulfate-rich strata, it is concluded that the banded upper wall exposes a complete section of Burns formation strata.

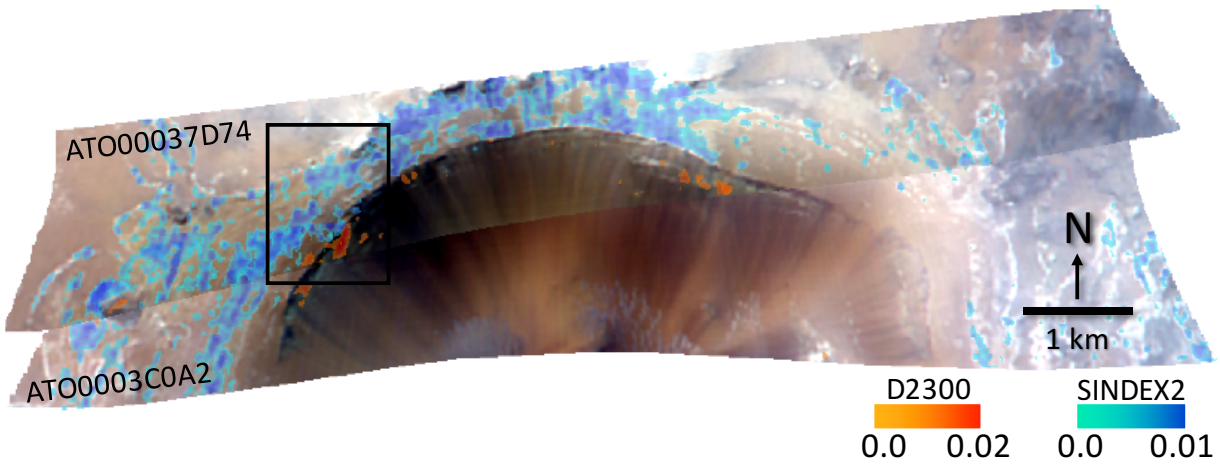

Figure 2.15: Mosaic of CRISM scenes ATO00037D74 and ATO0003C0A2 projected to 12 m/pixel and covering the interior and northern rim of Iazu Crater (R =2.53, G=1.51, B=1.06 μm). SINDEX2 derived from both observations is overlaid in blue and D2300_2 is overlaid in red; darker colors indicate higher values. Black box indicates the area shown in Figure 2.17.

The lower walls of Iazu are covered by debris shed from rocks above, likely combined with materials advected into the crater by wind. Low-calcium pyroxene is concentrated on the ridge and underlying exposed bedrock near the top of the section (Figure 2.12), consistent with the presence of Noachian-aged or older crust [*Mustard et al.*, 2005]. Both the debris-covered walls and the sand ripples on the floor of the crater display broad but relatively shallow absorptions at ~1 and 2.2 μm, consistent with a mixture of low- and high-calcium pyroxene (Figure 2.12 & 2.13). We interpret these interior materials as a mixture of bedrock and material eroded downslope from the bedrock having mainly basaltic provenance. The ejecta materials nearest to the rim are dominated by high-calcium pyroxenes, again likely as aeolian deposits.

We also examined parameter map D2300 (Table 2.3), which measures an absorption at 2.3 μm due to the combination of OH stretching and metal-OH bending, a feature of Fe^{3+} and/or Mg^{2+}-bearing smectites [*Clark et al.*, 1990]. The Fe^{3+}-bearing smectite nontronite displays a 2.29 μm absorption (Fe-OH), whereas Mg^{2+}-bearing saponite displays a 2.31 μm absorption (Mg-OH) (Figure 2.16) [*Clark et al.*, 1990]. We use the D2300 parameter to map smectites using the two

higher-resolution ATOs, ATO00037D74 and ATO0003C0A2. Smectites were found in a relatively narrow area of the crater wall, largely beneath the banded Burns formation outcrops (Figure 2.17). Individual spectra retrieved show how the existence of Fe^{3+}-Mg^{2+} smectites is inferred from the presence of 1.9, 2.3 and 2.4 μm absorptions (Figure 2.16). The average depth of the 2.3 μm absorption in the pixels shown is 0.0145 ± 0.005, comparable to that in detections in Marathon Valley [*Fox et al.*, 2016]. This feature is broader than absorptions seen in laboratory measurements for nontronite or saponite and positioned at an intermediate wavelength. We suggest this indicates smectite of mixed Fe^{3+}-Mg^{2+} composition, although it could also indicate an intimate mixture of nontronite and saponite. The two primary detection areas are located a similar distance below the rim, but widely separated. We did not detect any evidence for smectites in the overturned flap or ejecta. There are a number of possible explanations; it may be that smectites are present but not concentrated enough for orbital detection, erosion has removed them, or aeolian deposits on the shallower slopes mask them.

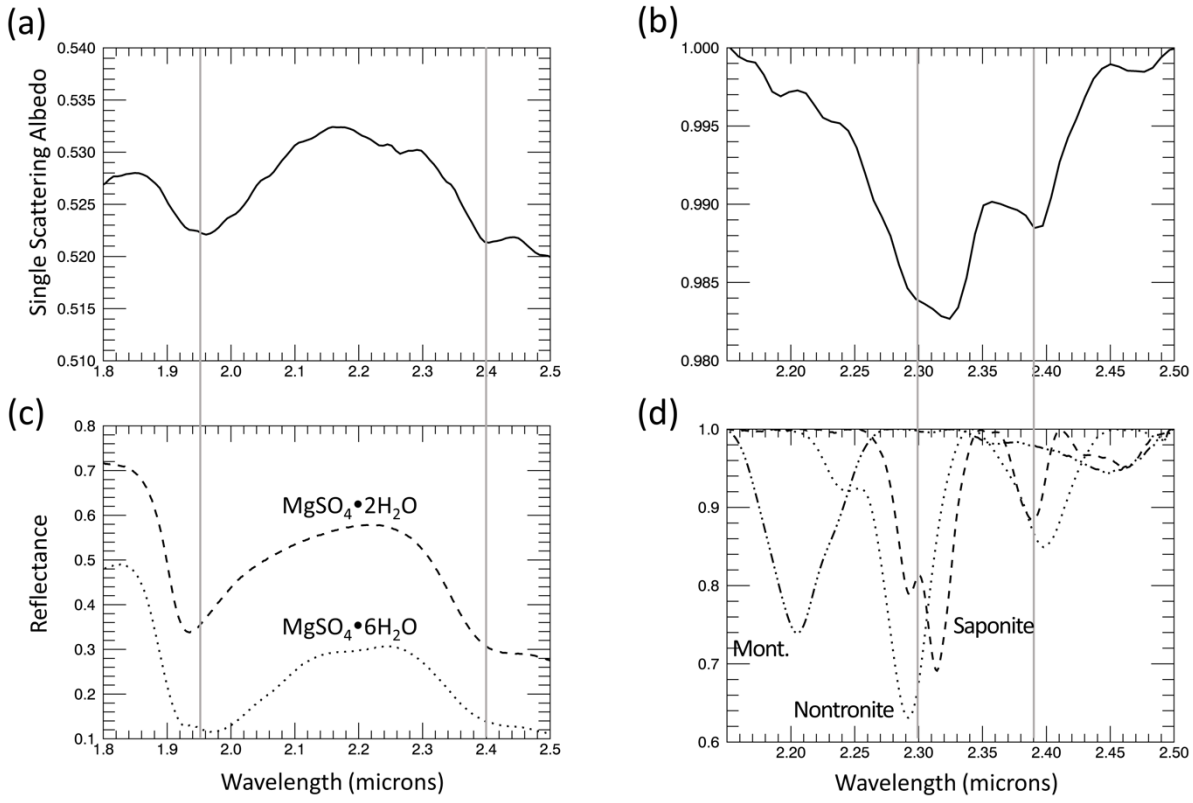

Figure 2.16: (a) CRISM spectra from ATO00037D74 from mean of 27 pixels in sulfate-rich areas shown in Figure 2.17. Vertical lines have been placed at the central wavelength of the absorption features for comparison. (b) Mean of ATO00037D74 SSA spectra of smectite detection areas, averaged over 28 pixels. Vertical lines have been placed at the central wavelength of the absorption features for comparison. (c) Laboratory spectra of hydrated Mg sulfates, courtesy of Alian Wang, Washington University in St. Louis. The 1.9 μm absorption is due to the bending and stretching combination absorptions of structural H_2O and OH. The 2.4 μm absorption is due to S-O bending or OH/H_2O combinations/overtones [*Cloutis et al.*, 2006]. (d) Laboratory spectra of smectites: nontronite (NAu-2), saponite (SapCa-1) and montmorillonite (SWy-2). Smectites have absorptions in the at 2.2-2.4 μm range due to the combination of OH stretching and metal-OH bending [*Clark et al.*, 1990]. Montmorillonite displays an Al-OH combination absorption at 2.21 μm. Fe^{3+}-bearing nontronite displays 2.29 μm and 2.39 μm absorptions whereas Mg^{2+}-bearing saponite displays 2.31 μm and 2.40 μm absorptions.

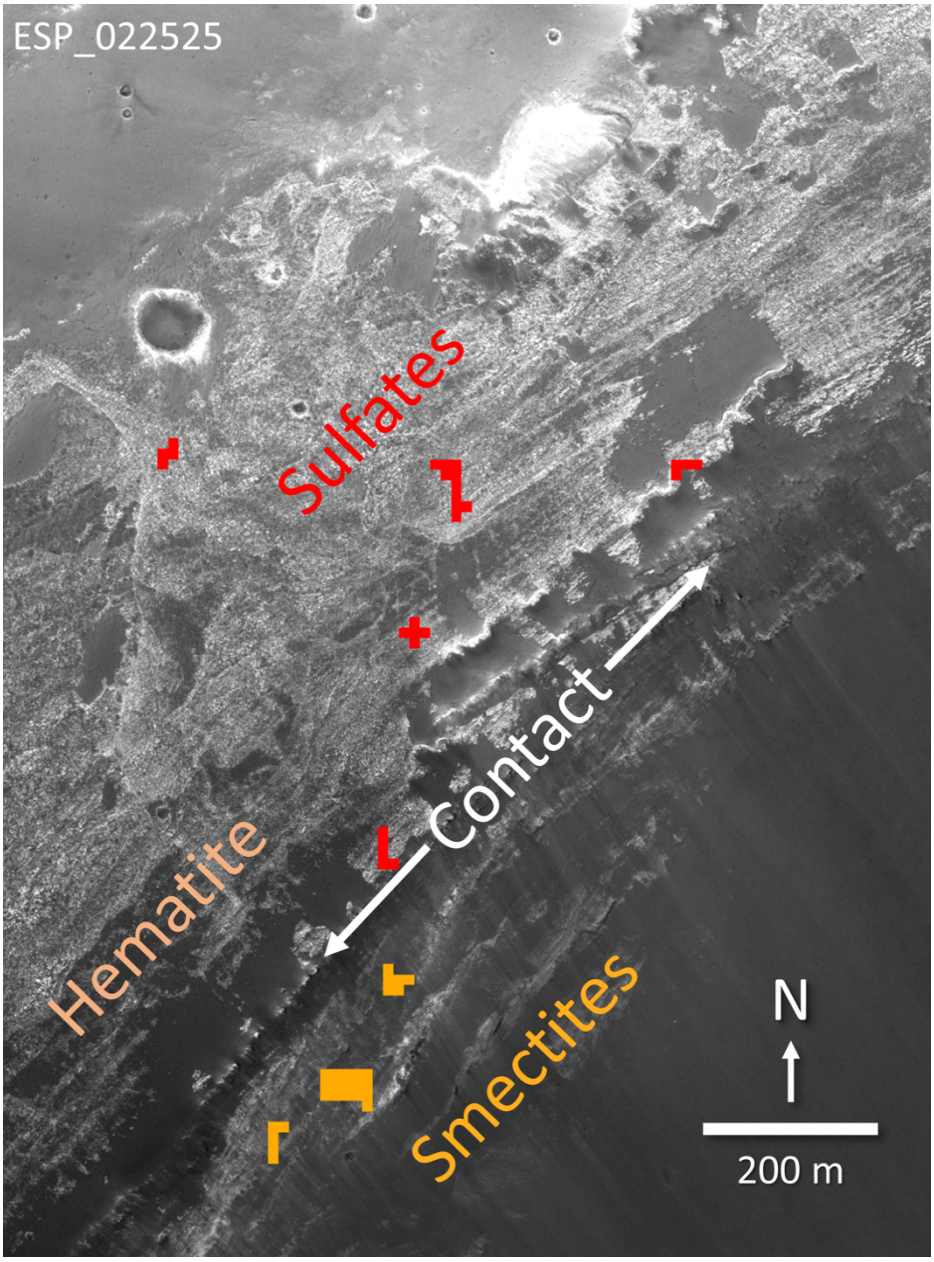

Figure 2.17: Subset of HiRISE ESP_022525_1775. Sulfate-rich Burns formation outcrops dominate Iazu's upper wall. These rocks are in contact with what are interpreted to be Noachian basaltic rocks that have been slightly altered in places to smectites. On the western side of the crater, these rocks are partially covered with hematite-rich Meridiani sands. Pixels used to extract Burns formation (Figure 2.16a) are shown in red. Pixels used to extract spectra for slightly altered basaltic rocks (Figure 2.16b) are shown in orange. Individual pixels were chosen by examining the areas of highest concentrations in SINDEX and D2300 parameter maps (Figure 2.15) and were selected by visual examination based on the shape and depths of absorption features that are at least 2x deeper than background noise.

2.6 Environmental Transitions in Meridiani Planum

The structural, stratigraphic, and spectral characteristics of Iazu's walls along with previous studies in the region allow reconstruction of the depositional environments for Burns formation and underlying strata. Burns formation strata crop out on the upper walls whereas basaltic rocks crop out lower in the section. In HiRISE images and associated DTM data, the contact between these two units is a continuous ridge several kilometers long that correlates well with (1) the abrupt spectral changes evident in CRISM data, (2) the sub-parallel trend of the layers and (3) a change in overall wall slope from relatively shallow to relatively steep. Specifically, the edges of Burns formation strata are less steeply sloped than the underlying rocks, consistent with more easily eroded sulfate-rich materials.

It would be of interest to correlate the complete Burns formation stratigraphic section exposed in Iazu with the sections examined by Opportunity in Endurance (~7 m) and Victoria (~10 m) craters [*Grotzinger et al.*, 2005; *Squyres et al.*, 2006, *Metz et al.,*2009, *Squyres et al.*, 2009]. The ~25 km distances and the ~150 m increase in elevation from these craters to Iazu prohibit a reliable projection of the strata to the section exposed in Iazu. Given the extensive evidence for formation of the Burns formation derived from Opportunity observations we interpret the boundary between the Burns formation outcrops and underlying strata as a major environmental transition. Meridiani Planum changed from an environment conducive to smectite formation, as also observed at Endeavour, to a largely evaporative and aeolian environment that produced the Burns formation sulfate-rich sandstones under generally acidic and oxidizing conditions, as observed elsewhere along the Opportunity traverse. In the walls of Iazu, the multiple stratigraphic levels of the dark ridges and associated banded deposits below the main contact suggest that the dark material is a sedimentary deposit buried by sulfate-rich rocks. These dark ridge deposits may

be fluvial in origin, giving way to short periods of evaporite formation, although HiRISE data do not allow conforming evidence of cross bedding, gravel bars, and cut and fill structures.

The Burns formation banded bright and dark strata beneath the inferred hinge line are traceable for tens to hundreds of meters around the circumference of the crater before encountering faults, and each exposed layer is typically 1 to 2 m in thickness (not accounting for dip introduced by the impact). In one of the best-preserved, least-faulted sections, four sets of bright-dark bands are in evidence, alternating to create a section that spans 14 m vertically (Figure 2.18b). Dark strata are more steeply sloped than brighter strata (Figure 2.5). This suggests that the dark strata are not the result of a dark soil coating, which would be concentrated on shallower slopes. Unfortunately, individual strata are too thin to be distinguished in CRISM data even after regularization to 12 m/pixel.

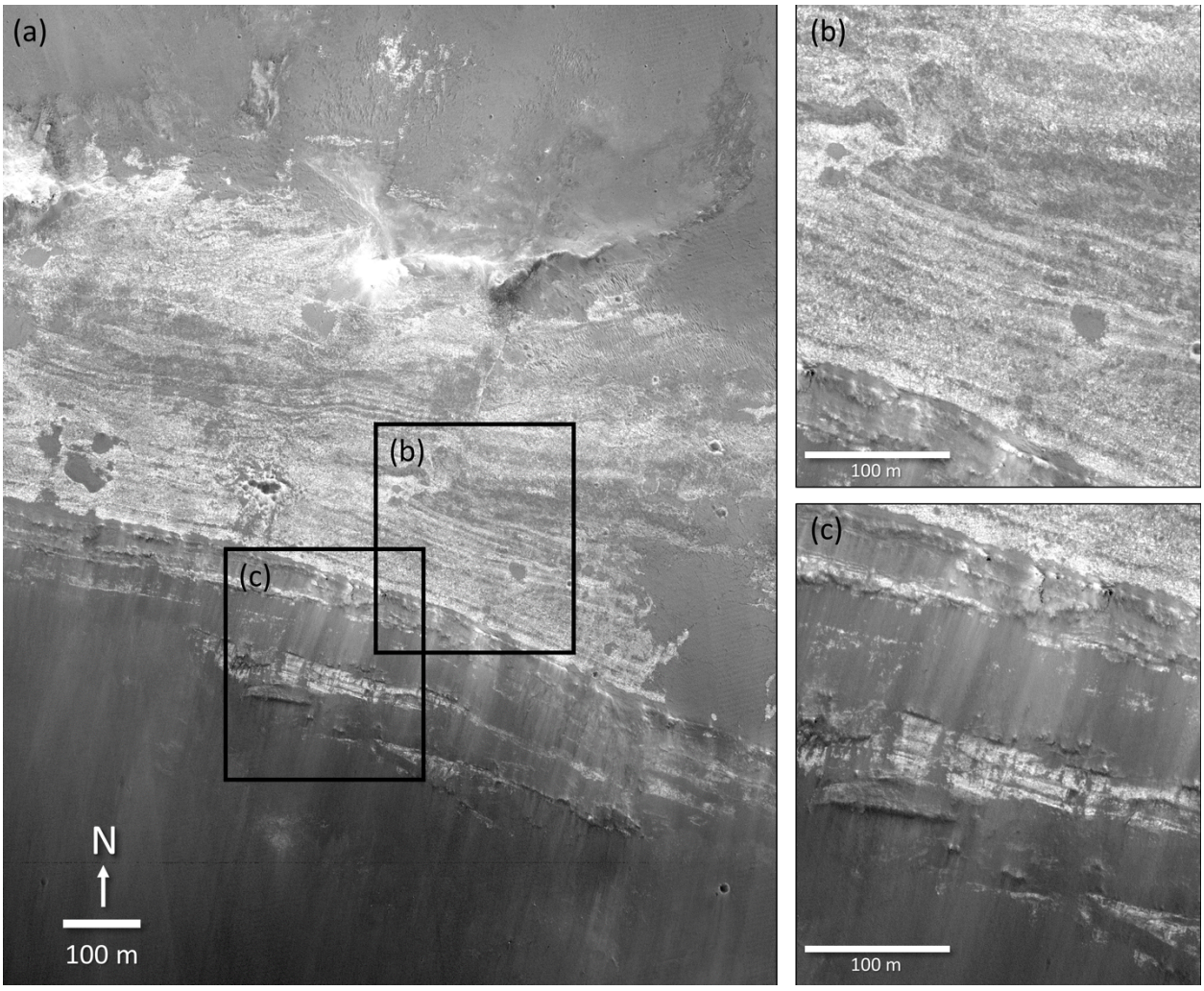

Figure 2.18: (a) Subset of HiRISE ESP_022670_1775 covering Iazu's northeast wall showing alternating bright and dark layers that can be traced for hundreds of meters around the circumference of the crater before being truncated by faults. (b) Detailed view of alternating bright and dark layered strata within the Burns formation strata. (c) Similar banded bright and dark layers below the contact with underlying basaltic strata, which suggest additional Burns-formation-like strata.

There are several possible origins for the banded bright and dark strata. Darker units may contain a greater proportion of intrinsically darker basaltic, clastic material than the brighter units. Alternately, bright and dark banding may represent periodic changes in the depositional environment of sulfates. *Lewis and Aharonson* [2014] describe a number of locations on Mars with periodic sedimentary bedding, with thicknesses ranging from a few meters at Schiaparelli Crater to 130 m in Juventae Chasma. These layered sections likely encompass multiple depositional

methods including playa/lacustrine and dust accumulation from air fall. They interpret these occurrences as arising from Milankovitch cycles, which arise from variations in Mars's orbital eccentricity and axial inclination that altered the annual cycle of insolation and resulted in periodic changes in climate. Additionally, stratigraphic sections that include interbedded mono- and polyhydrated sulfate strata are found in Valles Marineris [e.g., *Mangold et al.,* 2008; *Chojnacki and Hynek,* 2008; *Murchie et al.,* 2009b; *Bishop et al.*, 2009], Aram Chaos [*Lichtenberg et al.*, 2010] and northern Meridiani Planum [*Griffes et al.*, 2007]. In several locations dark and light sulfate strata thick enough to be resolved with CRISM exist (~18 m/pixel), specifically in eastern Candor Chasma [*Roach et al*., 2009], and Melas Chasma [*Liu et al.,* 2012]. The spectral signature of kieserite is associated with the darker layers and polyhydrated sulfates with the brighter layers. On the other hand, in western Candor Chasma polyhydrated sulfates are associated with darker strata and monohydrated sulfates with brighter strata [*Murchie et al*., 2009b], suggesting regional differences in depositional environments. In both sections of Candor Chasma the kieserite spectral signature also corresponds to steeper slopes, indicating differential resistance to erosion [*Roach et al*., 2009; *Murchie et al*., 2009b]. The banded nature of the Burns formation strata at Iazu is suggestive of such periodic processes, although, as stated above, we do not see spectral evidence for monohydrated sulfates.

Several bright and dark banded strata are visible in HiRISE images below the contact between the continuous Burns formation strata and underlying basaltic rocks. The banded strata are discontinuous and locally overlie the basaltic rocks (Figure 2.18). These layers are visually similar and comparable in thickness to banded strata visible in the overlying Burns formation outcrops. In one section below the contact three continuous pairs of strata are preserved, that are 14-18 m wide and span 5-7 m in elevation. These isolated banded strata do not show spectral

evidence of hydrated sulfates, possibly because of a partial cover of slope materials. The HiRISE-based similarity in banding characteristics for these lower strata and the continuous overlying Burns formation strata suggest that the lower bright strata are also sulfate materials. Their occurrence interspersed with dark strata suggests a gradual, rather than abrupt, transition from basaltic rocks of the lower unit to the Burns formation evaporative deposits above.

2.7 Conclusions and Implications

Our interpretation of the history of Iazu Crater is summarized in Figure 2.19. The stratigraphic section in Iazu's walls exposes basaltic rocks altered to smectites overlain by Burns formation hydrated sulfates, a transition inferred to represent a change from a regional-scale fluvial environment to an evaporative and wind-dominated depositional environment. As noted, the aqueous history of the Meridiani Planum region began with the fluvial transport of material from the adjacent southern highlands during the Noachian [*Hynek and Phillips,* 2001]. Fluvial systems eroded the Noachian cratered terrain and deposited sediments in fluvial and possibly deltaic and lacustrine environments. Minor alteration produced smectites in these deposits, either in place or before they were eroded and re-deposited at the Iazu site. The area continued to be dominated by fluvial activity until environmental change took place on a regional or global scale [*Bibring et al.*, 2006; *Andrews-Hanna et al.*, 2010]. Afterwards, Meridiani became an acidic, oxidizing playa environment, i.e. a depositional center likely due to rising ground waters sourced from the southern cratered highlands. Iazu formed after ~115 m of Burns formation strata were deposited. The low-angle Iazu impact ejected and overturned buried strata, both exposing banded Burns formation hydrated sulfates and forming an erosionally-resistant ejecta deposit. The plains materials were then preferentially eroded, leaving behind an elevated ejecta surface surrounding the crater. Aeolian processes have also transported and concentrated basaltic and hematite-rich sands in low-

lying areas and eroded the crater rim. Thus, Iazu's rim and walls provide a stratigraphic record that straddles Noachian basaltic crust through evaporative environments and finally the current anhydrous environment dominated by aeolian processes.

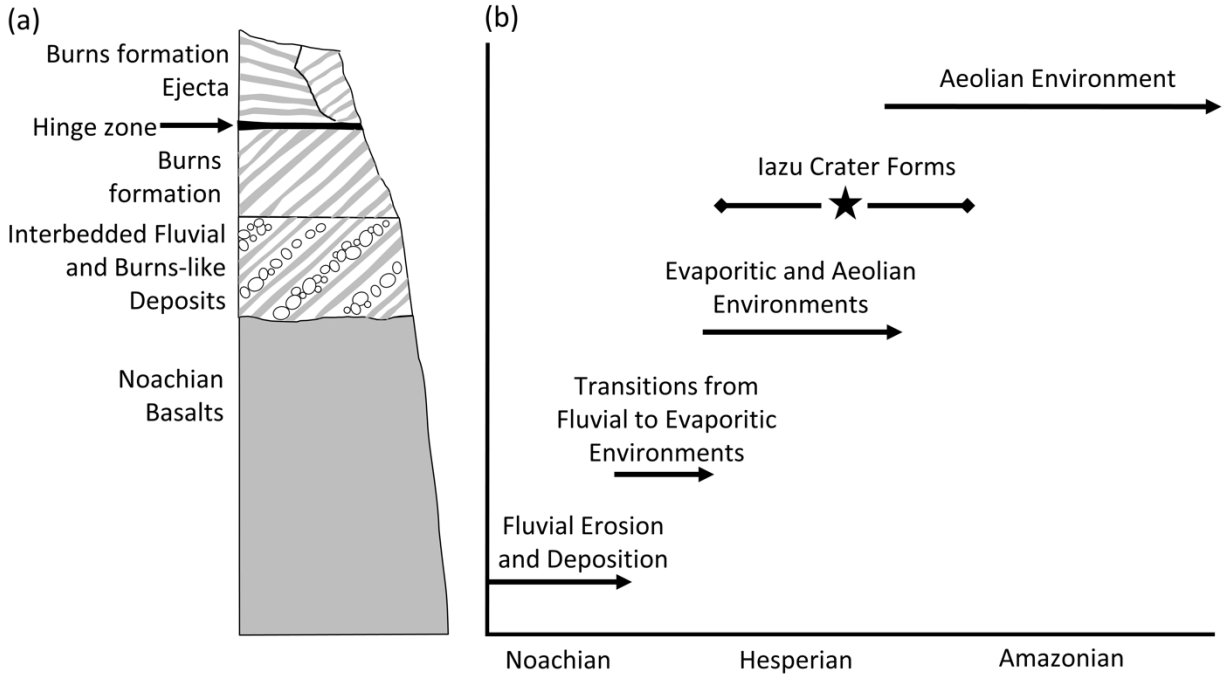

Figure 2.19: (a) Schematic stratigraphic section of Iazu's wall. The base of the section is interpreted to be Noachian basaltic crust, overlain by fluvial and sedimentary deposits, including the Burns formation deposits. The base is not exposed in Iazu's walls. The crater hinge zone and Burns formation ejecta are represented higher in the crater wall. (b) Schematic showing events in the vicinity of Iazu Crater. During the Noachian period, fluvial processes dominated the southern Meridiani region. In the late Noachian and early Hesperian period, there was a transition to a depositional center as rising groundwater led to an evaporitic environment. Iazu Crater formed after a significant amount of Burns formation sulfate-rich sandstones were deposited. Since the cessation of Burns formation deposition, aeolian processes of erosion, transport and deposition have dominated shaping the crater and surroundings.

References

Andrews-Hanna, J.C., M.T. Zuber, R.E. Arvidson, and S.M. Wiseman (2010), Early Mars hydrology: Meridiani playa deposits and the sedimentary record of Arabia Terra, *J. Geophys. Res. Planets*, *115*, E, doi:10.1029/2009JE003485.

Andrews-Hanna, J.C. and K.W. Lewis (2011), Early Mars hydrology: 2. Hydrological evolution in the Noachian and Hesperian epochs, *J. Geophys. Res. Planets*, *116*, E02007, doi:10.1029/2010JE003709.

Arvidson, R.E., et al. (2006), Nature and origin of the hematite-bearing plains of Terra Meridiani based on analyses of orbital and Mars Exploration rover data sets, *J. Geophys. Res. Planets*, *111*, E12S08, doi:10.1029/2006JE002728.

Arvidson, R.E., et al. (2014), Ancient aqueous environments at Endeavour Crater, Mars, *Science*, *343*, doi:10.1126/science.1248097.

Arvidson, R.E., et al. (2015), Mars Reconnaissance Orbiter and Opportunity Observations of the Burns Formation: Crater-Hopping at Meridiani Planum, *J. Geophys. Res. Planets*, *120*, doi:10.1002/2014JE004686.

Arvidson, R.E., et al. (2016), High concentrations of manganese and sulfur in deposits on Murray Ridge, Endeavour Crater, Mars, *American Mineralogist*, *101*, doi:10.2138/am-2016-5599.

Bibring, J.P. et al. (2006), Global mineralogical and aqueous Mars history derived from OMEGA/Mars express data, *Science*, *312*, 400–404, doi:10.1126/science.1122659.

Bishop, J.L. et al. (2008), Phyllosilicate Diversity and Past Aqueous Activity Revealed at Mawrth Vallis, Mars, *Science*, *321*, 830-833, doi:10.1126/science.1159699.

Bishop, J. L. et al. (2009) Mineralogy of Juventae Chasma: Sulfates in the Light-toned Mounds, Mafic Minerals in the Bedrock, and Hydrated Silica and Hydroxylated Ferric Sulfate on the Plateau, *J. Geophys. Res.*, *114*, doi:10.1029/2009JE003352.

Chojnacki, M. and B.M. Hynek (2008), Geological context of water-altered minerals in Valles Marineris, Mars, *J. Geophys. Res.: Planets*, *113*, doi:10.1029/2007JE003070.

Christensen, P. R., et al. (2004a), The Thermal Emission Imaging System (THEMIS) for the Mars 2001 Odyssey mission, *Space Sci. Rev.*, *110*, 85– 130.

Clark, R.N. et al. (1990), High Spectral Resolution Reflectance Spectroscopy of Minerals, *J. Geophys. Res. Solid Earth*, *95*, 12653-12680, doi:10.1029/JB095iB08p12653.

Cloutis, E.A. et al. (2006), Detection and discrimination of sulfate minerals using reflectance spectroscopy, *Icarus*, *184*, 121-157.

Crowley, J.K. (1991), Visible and near-infrared (0.4-2.5 μm) reflectance spectra of playa evaporite minerals, *J. Geophys. Res*. *96*, 16231-16240, doi:10.1029/91JB01714.

Crumpler, L.S. et al. (2015), Context of ancient aqueous environments on Mars from in situ geologic mapping at Endeavour Crater, *J. Geophys. Res. Planets*, *120*, 538-569, doi:10.1002/2014JE004699.

Edgett, K.S. (2005), The sedimentary rocks of Sinus Meridiani: Five key observations from data acquired by the Mars Global Surveyor and Mars Odyssey orbiters, Mars 1, 5-58, doi:10.1555/mars.2005.0002.

Ehlmann, B.L., et al. (2011), Subsurface water and clay mineral formation during the early history of Mars, *Nature*, *479*, 53–60, doi:10.1038/nature10582.

Ehlmann, B.L. and C.S. Edwards (2014), Mineralogy of the Martian surface, *Annual Review of Earth and Planetary Sciences*, *42*, 291-315, doi:10.1146/annurev-earth-060313-055024.

Fox, V.K. et al. (2016), Smectite Deposits in Marathon Valley, Endeavour Crater, Mars, Identified Using CRISM Hyperspectral Reflectance Data, *GRL*, *43*, 4885–4892, doi: 10.1002/2016GL069108.

Fraeman, A.A., et al. (2013), A hematite-bearing layer in Gale Crater, Mars: Mapping and implications for past aqueous conditions, *Geology*, *41*, 1103-1106, doi:10.1130/G34613.1.

Gendrin, A., et al. (2005), Sulfates in Martian Layered Terrains: The OMEGA/Mars Express View, *Science*, *307*, 1587-1591, doi: 10.1126/science.1109087.

Glotch, T.D., and J.L. Bandfield (2006), Determination and interpretation of surface and atmospheric Miniature Thermal Emission Spectrometer spectral end-members at the Meridiani Planum landing site, *J. Geophys. Res.*, *111*, E12S06, doi: 10.1029/2005JE00267.

Grant, J.A. et al. (2015), The degradational history of Endeavour Crater, Mars, *Icarus*, *280*, 22-36, doi:10.1016/j.icarus.2015.08.019.

Griffes, J.L., R.E. Arvidson, F. Poulet, A. Gendrin (2007), Geological and spectral mapping of etched terrain deposits in northern Meridiani Planum, *J. Geophys. Res.*, *112*, E08S09, doi:10.1029/2006JE002811.

Grotzinger, J.P. et al. (2005), Stratigraphy and sedimentology of a dry to wet eolian depositional system, Burns formation, Meridiani Planum, Mars, *Earth and Planetary Science Letters 240*, doi:10.1016/j.epsl.2005.09.039.

Hapke, B. (2012), Theory of Reflectance and Emittance Spectroscopy, Cambridge Univ. Press, New York.

Herrick, R.R. and K.K. Hessen (2006), The planforms of low-angle impact craters in the northern hemisphere of Mars, *Meteoritics and Planetary Science,* 41(10), 1483-1495, doi: 10.1111/j.1945-5100.2006.tb00431.x.

Hurowitz, J.A., W.W. Fischer, N.J. Tosca, and R.E. Milliken (2010), Origin of acidic surface waters and the evolution of atmospheric chemistry on early Mars, *Nat. Geosci.*, *3*, 323–326, doi:10.1038/ngeo831.

Hynek B.M. and R.J. Phillips (2001), Evidence for extensive denudation of the Martian highlands. *Geology*, *29*, 407-410, doi:10.1130/0091-7613.

Hynek, B.M. and R.J. Phillips (2008), The stratigraphy of Meridiani Planum, Mars, and implications for the layered deposits' origin, *Earth and Planetary Science Letters*, *274*, 214-220, doi:10.1016/j.epsl.2008.07.025.

Jaumann, R., et al. (2007), The high-resolution stereo camera (HRSC) experiment on Mars Express: Instrument aspects and experiment conduct from interplanetary cruise though the nominal mission, *Planetary and Space Science*, *55*, 928-952.

Jerolmack, D.J. et al. (2006), Spatial grain size sorting in eolian ripples and estimation of wind conditions on planetary surfaces: Application to Meridiani Planum, Mars, *J. Geophys. Res*., *111*, E12S02, doi:10.1029/2005JE002544.

Knauth, L. P., D. M. Burt, K. H. Wohletz (2005), Impact origin of sediments at the Opportunity landing site on Mars, *Nature*, *438*, 1123-1128, doi:10.0138/nature04383.

Kreisch, C. D., J.A. O'Sullivan, R.E. Arvidson, D.V. Politte, L. He, N.T. Stein, J. Finkel, E.A. Guinness, M.J. Wolff, M.G.A. Lapotre (2016), Regularization of Mars Reconnaissance Orbiter CRISM Along-Track Oversampled Hyperspectral Imaging Observations of Mars, *Icarus*, doi: 10.1016/j.icarus.2016.09.033.

Kumar, P.S. and D.A. Kring (2008), Impact fracturing and structural modification of sedimentary rocks at Meteor Crater, Arizona, *J. Geophys. Res.*, *113*, E09009, doi:10.1029/2008JE003115.

Lewis, K.W. and O. Aharonson (2014), Occurrence and origin of rhythmic sedimentary rocks on Mars, *J. Geophys. Res.: Planets*, *119*, 1432-1457, doi:10.1002/2013JE004404.

Lichtenberg, K.A. et al. (2010), Stratigraphy of hydrated sulfates in the sedimentary deposits of Aram Chaos, Mars, *J. Geophys. Res.: Planets*, *115*, E6, doi:10.1029/2009JE003353.

Liu, Y., R.E. Arvidson, R. Li, and W. Wang (2012), Hydrated minerals associated with interior layered deposits near the southern wall of Melas Chasma, Valles Marineris, Mars. Abstract 2572 presented at the 43th Lunar and Planetary Science Conference, The Woodlands, Tex., 19-23 March.

Malin, M.C., et al. (2007), Context Camera Investigation on board the Mars Reconnaissance Orbiter, *J. Geophys. Res.*, *112*, E05S04, doi:10.1029/2006JE002808.

Mangold, N. et al. (2008), Spectral and geological study of the sulfate-rich region of West Candor Chasma, Mars, *Icarus*, *194*, 519-543, doi:10.1016/j.icarus.2007.10.021.

McCollom, T.M. and B.M. Hynek (2005), A volcanic environment for bedrock diagenesis at Meridiani Planum on Mars, *Nature*, 1129-31, doi:10.1038/nature04390.

McEwen, A.S., et al. (2007), Mars Reconnaissance Orbiter's High Resolution Imaging Science Experiment (HiRISE), *J. Geophys. Res.*, *112*, E05S02, doi:10.1029/2005JE002605.

McGuire, P.C. (2009), An improvement to the volcano-scan algorithm for atmospheric correction of CRISM and OMEGA spectral data, *Planetary and Space Science*, *57*, 809-815, doi:10.1016/j.pss.2009.03.007.

McLennan, S.M. et al. (2005), Provenance and diagenesis of the evaporite-bearing Burns formation, Meridiani Planum, Mars, *Earth Planet. Sci. Lett., 240*, 95-121.

Melosh, H.J. (1989). Impact cratering: A geologic process, New York, Oxford University Press (Oxford Monographs on Geology and Geophysics, No. 11).

Metz, J.M. et al. (2009), Sulfate-rich eolian and wet interdune deposits, Erebus Crater, Meridiani Planum, Mars, *Journal of Sedimentary Research*, *79*, 247-264, doi:10.2110/jsr.2009.033.

Moratto, Z.M. et al. (2010), Ames Stereo Pipeline, NASA's Open Source Automated Stereogrammetry Software. Abstract 2364 presented at the 41th Lunar and Planetary Science Conference, The Woodlands, Tex., 1-5 March.

Morris, R.V. et al. (2006), Mössbauer mineralogy of rock, soil, and dust at Meridiani Planum, Mars: Opportunity's journey across sulfate-rich outcrop, basaltic sand and dust, and hematite lag deposits, *J. Geophys. Res. Planets*, *111*, E12S15, doi:10.1029/2006JE002791.

Murchie, S., et al. (2007), Compact Reconnaissance Imaging Spectrometer for Mars (CRISM) on Mars Reconnaissance Orbiter (MRO), *J. Geophys. Res. Planets*, *112*, E05S03, doi: 10.1029/2006JE002682.

Murchie, S., et al. (2009), Evidence for the origin of layered deposits in Candor Chasma, Mars, from mineral composition and hydrologic modeling, *J. Geophys. Res. Planets*, *114*, doi:10.1029/2009JE003343.

Mustard, J.F. et al. (2005), Olivine and pyroxene diversity in the crust of Mars, *Science*, *307*, 1594-1597, doi:10.1126/science.1109098.

Niles, P.B. and J. Michalski (2009), Meridiani Planum sediments on Mars formed through weathering in massive ice deposits, *Nature Geoscience*, 215-220, doi:10.1038/ngeo438.

Poelchau, M.H., and T. Kenkmann (2008), Asymmetric signatures in simple craters as an indicator for an oblique impact direction, *Meteoritics and Planetary Science*, *43*, 2059-2072, doi:10.1111/j.1945-5100.2008.tb00661.x.

Poulet, F., et al. (2005), Phyllosilicates on Mars and implications for early martian climate, *Nature*, *438*, 623-627, doi:10.1038./nature04272.

Roach, L.H., J.F. Mustard, S.L. Murchie, J-P. Bibring, F. Forget, K.W. Lewis, O. Aharonson, M. Vincendon, and J. L. Bishop (2009), Testing evidence of recent hydration state changes in sulfates on Mars, J. *Geophys. Res.*, *114*, E00D02, doi:10.1029/2008JE003245.

Robbins, S.J. and B.M. Hynek (2012a), A new global database of Mars impact craters ≥1 km: 1. Database creation, properties, and parameters, *J. Geophys. Res.*, *117*, E05004, doi:10.1029/2011JE003966.

Robbins, S.J., and B. M. Hynek (2012b), A new global database of Mars impact craters ≥1 km: 2. Global crater properties and regional variations of the simple-to-complex transition diameter, *J. Geophys. Res.*, *117*, E06001, doi: 10.1029/2011JE003967.

Shoemaker, E.M. (1963), Impact mechanics at Meteorite Crater, Arizona, in: Middlehurst, B.M and Kuiper, G.P. (eds) *The Moon Meteorites and Comets*, University of Chicago Press, Chicago, 301-336.

Soderblom, L.A., et al. (2004), Soils of Eagle Crater and Meridiani Planum at the Opportunity Rover Landing Site, *Science*, *306*, 5702, 1723-1726, doi:10.1126/science.1105127.

Squyres, S.W. et al. (2004), In Situ Evidence for an Ancient Aqueous Environment at Meridiani Planum, Mars, *Science*, *306*, 5702, doi:10.1126/science.1104559.

Squyres, S.W. et al. (2006), Overview of the Opportunity Mars Exploration Rover Mission to Meridiani Planum: Eagle Crater to Purgatory Ripple, *J. Geophys. Res.*, *111*, E12S12, doi:10.1029/2006JE02771.

Squyres, S.W. et al. (2009), Exploration of Victoria Crater by the Mars Rover Opportunity, *Science*, *324*, 1058-1061, doi:10.1126/science.1170355.

Squyres, S.W. et al. (2012), Ancient Impact and Aqueous Processes at Endeavour Crater, Mars, *Science*, *336*, 570-576, doi:10.1126/science.1220476.

Stamnes, K., S.C. Tsay, W. Wiscombe, and K. Jayaweera (1988), Numerically stable algorithm for discrete-ordinate-method radiative transfer in multiple scattering and emitting layered media, *Appl. Opt.*, *7*, 2502–2509, doi:10.1364/AO.27.002502.

Sullivan, R. et al. (2005), Aeolian processes at the Mars Exploration Rover Meridiani Planum landing site, *Nature*, *436*, 58-61, doi:10.1038/nature03641.

Viviano-Beck, C.E., et al. (2014), Revised CRISM spectral parameters and summary products based on the currently detected mineral diversity on Mars, *J. Geophys. Res.: Planets*, *119*, 1403–1431, doi:10.1002/2014JE004627.

Wiseman, S.M. et al. (2010), Spectral and stratigraphic mapping of hydrated sulfate and phyllosilicate-bearing deposits in northern Sinus Meridiani, Mars, *J. Geophys. Res.: Planets*, *115*, E7, doi: 10.1029/2009JE003354.

Chapter 3: A Neural Network Approach to Thermal Correction of CRISM Data

Abstract

The CRISM instrument measures spectral radiances from 0.36-3.92 μm, which includes terms from both the Mars atmosphere and surface. For $\lambda >\sim 2.6$ μm and typical Mars temperatures, retrieving surface reflectance is an underdetermined problem because both reflectance and emission terms comprise the radiance. Using the radiative transfer code DISORT, we model observed I/F to surface single scattering albedo (SSA) using the bidirectional Hapke function for solar terms and the directional-hemispherical form for emission. We include radiative terms for atmospheric gases and aerosols. We employ a neural network method to solve simultaneously for SSA and T, using DISORT results and training the system with a dataset of hundreds of spectra of Mars analog materials. This allows us to map the broad absorption feature centered near 3 μm caused by OH and H_2O in hydrated minerals, and adsorbed and absorbed water on mineral surfaces. For initial implementation of this method we focus on observations of Gale Crater, which is covered by multiple scenes from CRISM, and other orbital instruments, as well as independent ground-based temperature measurements from the MSL Curiosity rover. The retrieved temperatures, SSA spectra, and hydration features are consistent with independent measurements of surface properties.

3.1 Introduction

The Compact Reconnaissance Imaging Spectrometer for Mars (CRISM) onboard the Mars Reconnaissance Orbiter (MRO) began operating in 2006 and has acquired thousands of targeted hyperspectral image cubes of the Martian surface [*Murchie et al.,* 2007]. Two gimballed imaging spectrometers capture nominally 18 m/pixel observations from 0.36-1 μm ('S' spectrometer) and

1-3.92 μm ('L' spectrometer). The standard archived product created at the CRISM Science Operations Center (SOC) is I/F, the radiance on sensor divided by solar irradiance at the Martian surface and π. The spectra of Mars are complex and variable over small spatial areas. The spatial resolution of CRISM allows characterization of small outcrops that highlight the diversity of past environments on Mars. CRISM has been used to make many important contributions to the study of the Martian surface [*Murchie et al.,* 2009], but its full potential has not yet been realized, particularly for longer wavelength data with both solar and thermal contributions.

We present the results of a new method to model thermal effects in CRISM data [*He et al.,* 2018]. The wavelength region > 2.6 μm has been utilized in relatively few previous CRISM studies because the presence of thermal effects make spectral retrievals an underdetermined problem. In the visible and very near infrared (0.3-2.6 μm) region, emission is negligible; at these wavelengths the observed radiance is contributed by atmospheric and surface scattering and absorption. At temperatures typical of the daytime Martian surface, thermal emission becomes significant for λ> ~2.6 μm (Figure 3.1). This makes it impossible to uniquely separate the contributions of mineralogy and textural properties versus surface temperature; for instance, a higher measured radiance value could be the result of truly higher surface albedo or a slightly warmer surface (Figure 3.2). We leverage a machine learning technique, specifically a neural network, to simultaneously solve for temperature and surface albedo using our prior knowledge of laboratory spectra. We then use these temperatures to fully model the reflection and emission components of each CRISM spectrum, taking into account atmospheric extinction, and produce surface single scattering albedo.

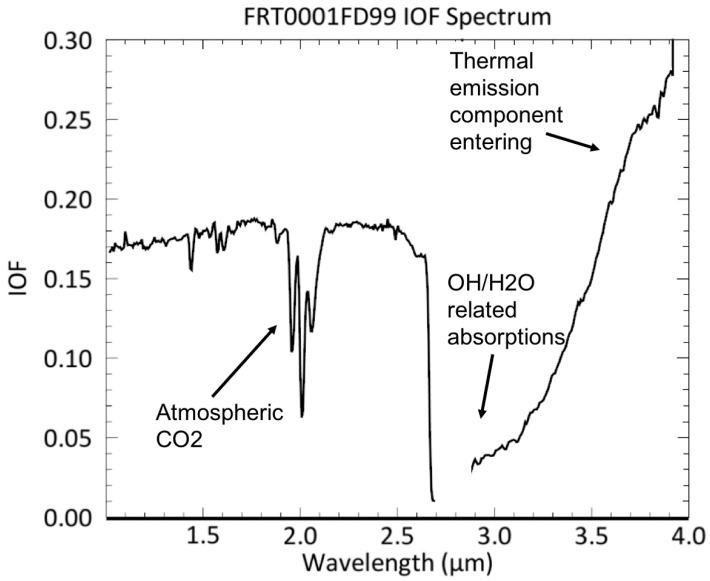

Figure 3.1: CRISM I/F spectra from the 'L' detector (1-3.8 μm). The three absorptions centered at ~2μm are due to CO2 absorptions in the atmosphere. The broad absorption centered at ~3μm is due to overlapping OH and H2O absorptions in the atmosphere, structurally bound in minerals, and adsorbed/absorbed on surfaces. At short wavelengths the observed I/F is dominated by reflectance. Beyond ~2.6 μm, the increasing I/F values with increasing wavelength are due to the effects of thermal emission, which become more significant at longer wavelengths.

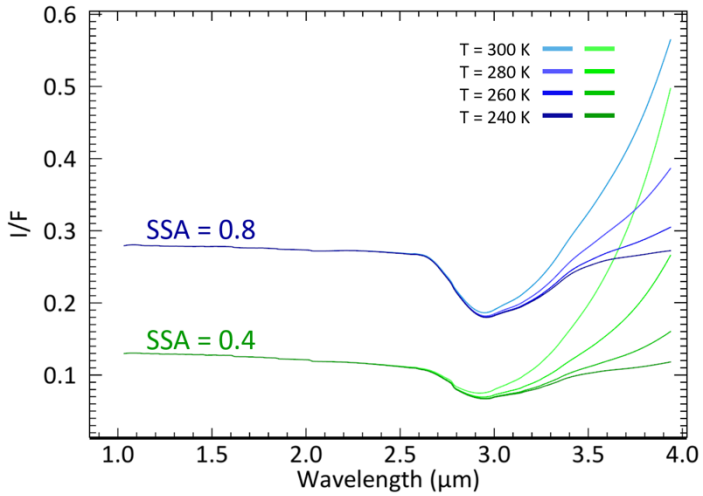

Figure 3.2: Simulated I/F spectra produced by DISORT for four temperatures and two SSA values. In each example SSA is a fixed value for all wavelengths. Emission effects become more important at higher temperatures until a small change in temperature can result in drastically different I/F values measured for the same SSA.

Fully modeling CRISM spectra from 0.4-3.8 μm allows retrieval of SSA values near 3 μm, which has important implications for the water content of the surface. The fundamental OH

stretches in liquid water occur at 3320 cm^{-1} (3.106 μm) and 3445 cm^{-1} (2.903 μm), whereas the fundamental H_2O bend in liquid water occurs at 1630 cm^{-1} (6.135 μm) [*Aines and Rossman*, 1984]. The first overtone of the 6 μm fundamental H_2O bend overlaps the stretch fundamentals near 3280 cm^{-1} (3.049 μm) [*Bayly et al*., 1963, *Falk and Ford*, 1966]. The position of these features in minerals varies with the type of bond structures. A broad absorption feature near 3 μm has been observed in spectra of Mars since the early days of Earth-based observing and Mariner flyby measurements [*Houck et al.,* 1973; *Pimentel et al.,* 1974]. This feature is observed in all OMEGA [*Bibring et al.,* 2006, *Gendrin et al.*, 2005, *Poulet et al.*, 2005; *Joulet et al.*, 2007; *Milliken et al.*, 2007] and CRISM spectra of Mars. Without accurately accounting for thermal emission, the depth and shape of the 3 μm absorption features cannot be rigorously measured.

We test our new capabilities using targeted CRISM observations over Gale Crater, the site of the Mars Science Laboratory Curiosity rover's landing site in 2012 and its subsequent traverses [*Grotzinger et al.*, 2012]. Gale's location near the equator (5.4ºS) means it experiences afternoon surface temperatures >240 K, even during the winter [*Vasavada et al.*, 2017], allowing us to determine temperatures using the CRISM spectral range. Landing sites such as Gale offer a unique opportunity to compare surfaces at the scale of outcrops and in broader context from orbit. Gale Crater has the dual advantage of being well characterized by orbital thermal emission spectroscopy and having available in situ surface temperature measurements. Curiosity is currently exploring the ~5 km high sedimentary mound Aeolis Mons, informally termed Mount Sharp. The lower layers of Mount Sharp were formed in ancient fluvial and lacustrine environments [*Grotzinger et al.*, 2015] and contain diverse mineralogical evidence of aqueous alteration including hematite, clays, and hydrated sulfates [*Milliken et al.*, 2010; *Fraeman et al.*, 2016]. This location provides a diversity of materials to examine with the full CRISM wavelength region. The CRISM

observations in this study were chosen from those that overlap the Curiosity traverse and have low dust atmospheric opacities; they include HRL0000BABA, FRT0000B6F1, FRT000248E9, and FRT0001FD99 (Table 3.1).

Table 3.1: CRISM Observations

CRISM ID	Earth Date	Mars Year	Solar Longitude(L_s)	Local Solar Time (LST)
FRT0000B6F1	2008-07-09	29	96.3°	15:24
HRL0000BABA	2008-07-20	29	101.3°	15:21
FRT0001FD99	2011-08-25	30	350.6°	14:09
FRT000248E9	2012-04-24	31	101.2°	15:12

3.2 Previous Work

Numerous previous attempts have been made to derive the thermal component and remove it from I/F spectra of Mars, but none of these previous studies have fully modeled SSA with reflection and emission properly included. Any approach that makes broad assumptions about the expected mineralogy of the surface runs the risk of being ill-suited to Mars, as the Martian surface exposes a great diversity of localized exposures of minerals. Additionally, the Martian seasonal and diurnal weather cycles limit the applicability of fine-scale thermal modeling to predict surface temperature independently.

Remote sensing observations necessarily capture radiance in a particular direction. Bidirectional reflectance is a measure of the ratio of incident collimated radiance that is scattered in a given direction, and is a function of the incidence, emergence, and phase angle. Hemispherical reflectance is instead the radiance scattered over an entire hemispherical surface, divided by the incoming irradiance [*Hapke*, 2012]. For a surface in thermal equilibrium, the reflection and emission terms are related by Kirchhoff's law as $r + \varepsilon = 1$. This expression is only valid for reflectance and emissivity with the same observation geometry. Emission is a directional-

hemispherical quantity by nature, and by definition the equivalent in reflectivity must have the same geometry. A remote sensing bidirectional reflectance must therefore be converted to directional-hemispherical to compare directly to hemispherical emissivity.

Erard and Calvin [1997] used Mariner 6/7 and Phobos 2 near-IR spectra of Mars to approximate the reflectance component at long wavelengths as a linear combination of dark and light type spectra. They assumed a Lambertian surface, a simple form of directional-hemispherical albedo where the scattered radiance only varies with incidence angle:

$$r_L = \frac{1}{\pi} A_L \mu_0 \qquad (3.1)$$

where r_L is the hemispherical reflectance, AL is the Lambert albedo, and μ_0 is the cosine of the incidence angle [*Hapke*, 2012]. They estimate the atmospheric transmission using a modeled spectrum scaled to fit the 2 μm CO2 absorptions. This linear spectral behavior was a fairly good approximation considering the large spatial resolution of these instruments, but is not appropriate for CRISM-scale measurements, which typically contain much greater spectral variation. *Jouglet et al.* [2007] and *Milliken et al.*, [2007] presented a method for thermally correcting observations taken by OMEGA onboard Mars Express [*Bibring et al.*, 2004], also assuming a Lambertian surface, first having applied the volcano scan atmospheric correction. They used the Lambert albedo at 2.3-2.5 μm to predict the Lambert albedo at 5 μm, assuming that it can be approximated as a linear combination of bright and dark spectra from *Erard and Calvin* [1997]. They then subtracted this reflectance component and fit a blackbody to the remainder to estimate the temperature. Despite these approximations, their results were fairly reasonable because of the small reflectance component to be removed at 5 μm.

Milliken [2006] attempted to apply this same technique to CRISM data, but met with limited success, as CRISM data contains a much larger reflectance component even at its

maximum wavelengths of ~4 μm. Compared to CRISM, the greater wavelength range of OMEGA provides a better "lever arm" for temperature determination, i.e. greater separation between thermal emission curves in the acquired wavelength range. Surface temperature retrievals are especially inaccurate for low temperatures due to the small variation between blackbody curves at those wavelengths.

A neural network has been used previously in the realm of Earth-focused observing. For example, *Mao et al.*, [2008] used a neural network method to retrieve emissivity and temperature from multispectral ASTER TIR images, focusing on the thermal emission wavelength region only.

3.3 DISORT Processing to Single Scattering Albedo

In the case of mixed reflected solar radiation and thermally emitted radiation, the radiance from a surface in a direction is given as:

$$I(i,e,g) = Jr_d(i,e,g) + \varepsilon_d(e)U_0(T) \qquad (3.2)$$

where i, e, and g are the incidence, emergence, and phase angles, J is the irradiance, r_d is the bidirectional reflectance, ε_d is a directional emissivity, and U is a blackbody function [*Hapke*, 2012, p. 427]. However, light passing through an atmosphere is subject to absorption and scattering from gases and aerosols. On its path to the surface, a collimated beam of incident solar radiation is partially absorbed and scattered in other directions by the atmosphere. In addition, the atmosphere itself emits radiation. The remainder that reaches the surface has some fraction absorbed and reflected according to the surface scattering function. The surface and atmosphere emit hemispherically, depending on both the kinetic temperature and the albedo, but is observed in a directional mode. The combination of reflected and emitted surface radiation is absorbed and scattered away by the atmosphere on its path to the detector. In addition, for both incoming and

outgoing radiation, some fraction of light scattered and emitted from the atmosphere may also be received by the detector. Thus the measured radiance is a combination of all of these factors.

In the spectral region containing both reflection and emission, provided the incidence, emergence, and phase angles are known, and atmospheric extinction and emission are properly modeled, the problem is still one of a single measurement and two unknowns, i.e. surface albedo and kinetic temperature. Our goal in this work is to convert CRISM I/F spectra to single scattering albedo (SSA), a measure that is independent of lighting and viewing geometry and can be used to quantitatively model relative proportions of minerals. SSA is defined as the ratio of power scattered to power scattered and absorbed [*Hapke*, 2012]. We use the DISORT radiative transfer code to model surface and atmospheric interactions and ultimately SSA. DISORT is a general-purpose discrete ordinates algorithm for radiative transfer calculations [*Stamnes et al.*, 1988]. It models scattering, absorption, and emission in a plane-parallel medium and scattering and emission at a surface.

The relationship between single scattering albedo and bidirectional reflectance (BRDF) is described by the Hapke function:

$$BRDF = \frac{w}{4\pi}\frac{\mu_0}{\mu+\mu_0}\{P(g)[1+B(g)] + H(\mu)H(\mu_0) - 1\} \qquad (3.3)$$

Here w is the single scattering albedo, μ_0 and μ are the cosines of the incidence and emergence angles, B is the opposition effect term, and H is the Chandrasekhar multiple scattering function. P is the phase function, which describes the angular distribution of reflected light. Here we use a Henyey-Greenstein two-term, two-parameter phase function:

$$P(g) = \frac{(1+f)}{2}\frac{(1-a^2)}{[1+a^2-2a\cos g]^{3/2}} + \frac{(1-f)}{2}\frac{(1-a^2)}{[1+a^2+2a\cos g]^{3/2}} \qquad (3.4)$$

where a is the asymmetry factor and f is the forward fraction. For the scenes included in this chapter we chose f=0.1 and a=0, which corresponds to a moderately forward-scattering

function for all phase angles. Other choices of phase functions are reasonable, but detailed discussion of the theory is beyond the scope of this study. In DISORT, the emissivity is calculated by integrating the bidirectional reflectance over a hemisphere to obtain directional-hemispherical reflectance, at which point Kirchhoff's law is applied to obtain the directional-hemispherical emissivity.

DISORT has been adapted for the Martian environment [*Wolff et al.*, 2009]. The output of DISORT is a many-dimensional lookup table that can be queried to find SSA for a given I/F pixel. A new lookup table is generated for each CRISM scene and range of parameters of interest. Inputs include lighting and viewing geometry (i, e, g), dust and ice atmospheric opacities (τ_d, τ_i), atmospheric pressure at the surface, and temperature.

Lighting and viewing geometry (i, e, g) for each pixel in the CRISM scene are included in the SOC-generated Derived Data Record (DDR) file. DISORT can include a range of incidence angles, which allows modeling of topography. This dramatically increases the required computation time, so in some of our runs only a single incidence angle is used.

Atmospheric aerosols must be modeled, as scattering from them can brighten or darken the observed I/F as a function of wavelength. The distribution of dust and ice aerosols in the atmosphere varies with season [*Smith et al.*, 2013], and so is variable for each CRISM scene. Dust atmospheric opacities are derived from CRISM Emission Phase Function (EPF) observations at 900 nm, and where available may be compared to opacities derived by rover cameras on the same sol. Emission Phase Function images were taken in the early years of CRISM's mission; when paired with a targeted observation of the surface, they were taken on the approach and retreat from the target at a range of emission angles (30-70°) [*Murchie et al.*, 2007; *Smith et al.*, 2009]. The dust aerosol single scattering albedo was derived from CRISM EPF observations in *Wolff et al.*

[2009]. Ice atmospheric opacities are derived from MARCI observations at 320 nm [*Malin et al.*, 2008].

The atmospheric gases carbon dioxide, water vapor, and carbon monoxide are modeled; their effects are estimated from the depth of the 2 μm CO_2 features in the CRISM data themselves, as determined by *Smith et al.* [2009]. They are modeled using a correlated-k approach for absorption [*Lacis and Oinas*, 1991]. If significant topographic relief is involved, the atmospheric retrieval can differ significantly even within a single scene. The abundances of these gases vary throughout the year and this calculation must be performed independently for each CRISM scene. Optionally, this may be omitted from DISORT modeling to save computation time, in which case the input I/F was pre-processed with the volcano scan atmospheric correction. Volcano scan leverages the spatial homogeneity and large change in elevation between the summit and base of Olympus Mons to produce a transmission spectrum of atmospheric gases [*Langevin et al.*, 2005; *Bellucci et al.*, 2007; *McGuire et al.*, 2009]. This correction has been widely used on CRISM and OMEGA data.

The DISORT temperature range is chosen to encompass reasonable Mars daytime surface temperatures, e.g., 230 to 300 K. In order to solve for SSA at each pixel, we interpolate within the DISORT many-dimensional lookup table. At this stage we require a surface temperature value for each pixel in the scene, which we wish to derive from the CRISM data itself.

3.4 Neural Network Method Outline

We apply a neural network approach to the problem of non-unique emissivity and temperature retrievals. A detailed description of the method is outlined in *He et al*. [2018]. A neural network is a machine learning tool that uses a training set to learn rules about relationships. Here

we wish to develop a neural network that can learn to separate the effects of temperature and SSA in an I/F spectrum.

The neural network method consists of two steps: training and application. We first train the neural network with a set of laboratory spectra of Martian analog materials. The laboratory spectra are linearly combined in different proportions to generate a training set of 300,000 spectra. This training set is designed to span the parameter space of all possible Mars materials to avoid biasing what the neural network should find. Details of the origin of the training spectral library are presented in Section 5. We generate a simulated CRISM I/F cube for the network to learn from by using the DISORT lookup table for a specific scene in reverse: each training spectrum is assigned lighting and viewing conditions and a temperature from a range appropriate to the scene. Thereby an SSA spectrum is modeled to an "I/F".

To train the neural network, we choose a wavelength range for training that is appropriate for CRISM data. CRISM I/Fs do not include values for reflectance between 2.65-2.85 μm, as this region contains a saturated CO2 band. In addition, CRISM has low signal-to-noise from 2.85-2.9 μm and > 3.8 μm [Scott Murchie, personal communication]. Therefore our "short wavelength" or solar reflectance only range is 1.68-2.50 μm, and the "long wavelength" or combined emission and reflectance range is 2.90-3.70 μm.

The inputs to the neural network training routine are the short wavelength SSA training spectra, the I/F cube we generate, and incidence, emergence, and phase angles from the DDR (Figure 3.3). The goal is to accurately retrieve from the I/F cube the training simulated SSA spectra and the temperature. The neural network consists of a layer of interconnected nodes, initially with the same activation function weights. At the end of each iteration, the neural network adjusts these weights to assign more or less value to different input parameters. The neural network iterates,

back-propagating and computing the sums of squares of deviations between predicted and actual long wavelength SSA and T. It follows a gradient descent path to converge on the possible set of weights that best reproduces the input.

The trained neural network is then applied to a real CRISM I/F to retrieve the SSA cube and T maps (Figure 3.4). Each pixel is treated independently of its surroundings. We then use the temperature map as an input to our DISORT routine to solve for SSA from 1-3.8 μm. These SSA cubes are median filtered to remove extreme noise and then regularized and map-projected with a log-log maximum likelihood method [Kreisch et al., 2017; He et al., 2017].

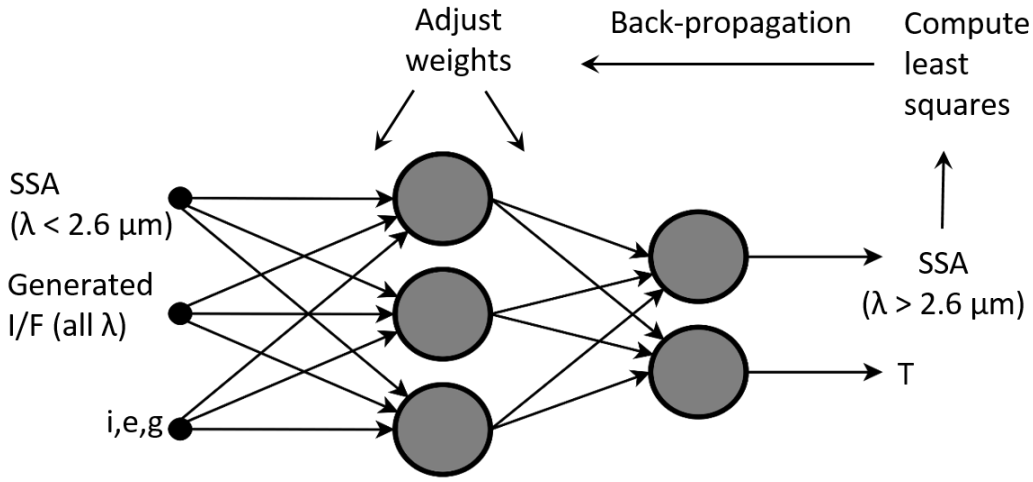

Figure 3.3: Schematic of our neural network approach. Inputs include the manufactured I/F cube, the spectral library SSA cube for λ<2.6μm, and lighting and viewing geometry. Outputs are the retrieved SSA cube for λ>2.6μm and temperature. Outputs are compared to the SSA and T values that were used to create the I/F, and the least squares values are computed. The neural network back-propagates and iterates, adjusting the internal weights until a sufficiently close solution is obtained.

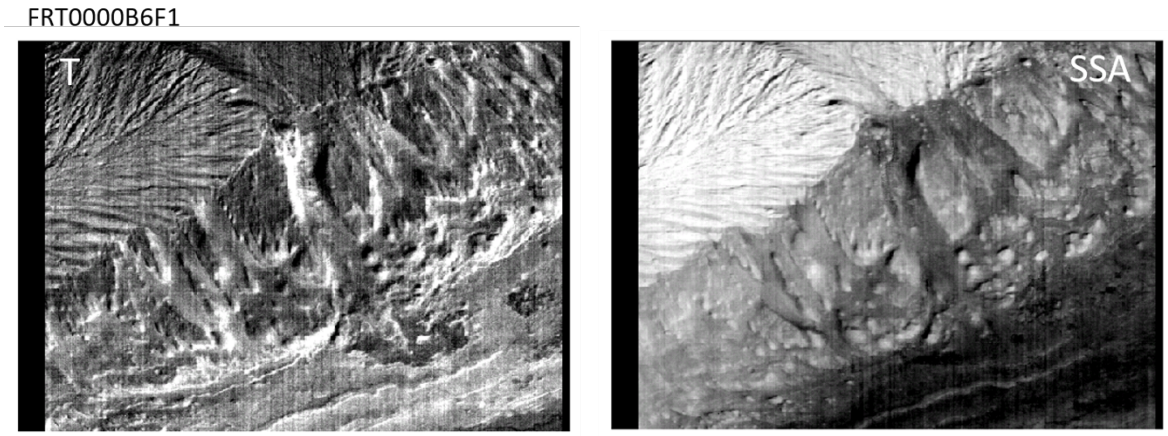

Figure 3.4: Example output of the neural network method for FRT0000B6F1 covering a portion of northwestern Mt. Sharp. Left: Temperature with range 245-270 K. Right: Single scattering albedo, displayed at 3.70 μm. Outputs are shown in sensor space and not map projected.

3.5 Training Set Spectral Library

The choice of training set is key to the success of the method, as the neural network can only learn from the information it is provided. Our input spectral libraries are derived from laboratory spectra of a variety of Mars analog materials. They are selected to encompass the range of minerals that have been observed or are expected on the Martian surface [*Ehlmann and Edwards*, 2014]. The spectra include pure mineral phases: pyroxenes, olivines, plagioclase, iron oxides, phyllosilicates, sulfates, silica, as well as natural rocks and soils. We deliberately do not include spectra of minerals and rocks that are highly unlikely to be exposed on Mars at CRISM spatial scales.

It is challenging to find laboratory spectra that match the CRISM wavelength range. Many libraries cover either the 1-2.6 μm region, or the thermal infrared only, omitting the 3-4 μm region. The sources of our spectra are the ASTER spectral library [*Baldridge et al.*, 2009], data collected at RELAB by various investigators [sources in Table 3.2], and FTIR data of Mars analog and meteorite samples collected at the Johnson Space Center [Richard Morris, personal communication]. Ideally we would use the full CRISM 'L' detector wavelength range for training.

However, the minimum wavelength for JSC FTIR data is 1.6 μm. These spectra are primarily derived from volcanic samples that are very good Mars analogues, and they make up a significant portion of our training data set. This more restricted wavelength range still captures the overall shape of the spectrum in the solar reflectance regime.

The spectra in our training library are used in their original reflectance values without being pre-converted to SSA. The key feature for neural network training is the shape of the overall spectrum. While the average value of albedo may change significantly, the general relationship between reflectance <2.5 μm and > 2.8 μm will remain similar, and therefore converting the set of laboratory spectra to SSA would not result in a significantly different training set with respect to the neural network. The laboratory spectra of pure minerals often have absorption features that are extremely deep compared to real Mars spectra. As necessary the absolute values are linearly scaled and/or shifted to more closely simulate reasonable SSA values, without changing the overall spectral shape.

Table 3.2: Neural Network Training Spectral Library

Sample Type	Sample Details	Grain size	Source	Reference
Rocks				
Basalt	Basalt_H1, Basalt_H2, Basalt_H5, Basalt_7, Basalt_H9, Basalt_H10	Solid and "fines" (unk)	ASTER spectral library/ rock_jhu_becknic	*Baldridge et al.*, 2009, *Kokaly et al.*, 2017
Basalt	PM-6	36-80 μm, 80-160 μm	RELAB	*Nair and Mathew*, 2014
	PM-13	36-80 μm, 80-160 μm	RELAB	*Nair and Mathew*, 2014
	PV-3	<63 μm, 63-200 μm, 200-500 μm, 500-3000 μm	RELAB	*Nair and Mathew*, 2014
Basalt	HWMU574	<1000 μm, 500-1000 μm		

Basaltic glass	HWKV340		JSC	
Basaltic andesite	Andesite_H4	Solid and "fines" (unk)	ASTER spectral library/ rock_jhu_beckni c	*Baldridge et al.*, 2009, *Kokaly et al.*, 2017
Gabbro	Gabbro_H1	Solid and "fines" (unk)	ASTER spectral library/ rock_jhu_beckni c	*Baldridge et al.*, 2009, *Kokaly et al.*, 2017
Gabbro	SJ-3	36-80 μm, 80-160 μm	RELAB	*Nair and Mathew*, 2014
Palagonite	HWHP301		JSC	
	HWMK011 (glass w/plag and hematite)	500-1000 μm, < 20μm	JSC	
	HWMK013 (devitrified glass)	Unk	JSC	
	HWMK020 (hematite-bearing volcanic tephra)	Unk	JSC	
	HWMK024 (naturally altered ash)	Unk	JSC	
	HWMK30	500-1000 μm, < 45μm	JSC	
	HWMK503	500-1000 μm, < 1000μm	JSC	
	HWMK504	500-1000 μm, < 1000μm	JSC	
	HWMK508	500-1000 μm, < 45μm	JSC	
	HWMK513	<1000 μm, 500-1000μm	JSC	
	HWMK515	500-1000 μm, < 45μm	JSC	
	HWMK530	500-1000 μm, < 45μm	JSC	
	HWMK600	500-1000 μm, < 45μm	JSC	
	HWMK720	Unk	JSC	
	HWMK740	500-1000 μm, < 45μm	JSC	
	HWMK741	500-1000 μm, < 45μm	JSC	
	HWMK742	Unk	JSC	
	HWMK919	500-1000 μm, < 45μm	JSC	

	HWMK940	500-1000 μm, < 45μm	JSC	
	PH-201	<1000 μm, 500-1000μm	JSC	
Tephra, acid sulfate-leached	HWKV051	<1000 μm, 500-100 μm	JSC	
Shergottite	EET79001	<5 μm, <45 μm, 45-90μm, 90-150 μm	JSC	
Dolomite	89 dolomite	Unk	JSC	
Synthetic				
Glass	Adirondack Glass	Unk	JSC	
Soils				
Sand/loam/silt/clay	85P4663, 87P3665, 87P3671, 87P3468, 87P2410, 88P4699, 87P337, 87P325, 87P313, 87P707, 87P706, 87P764, 86P4561, 85P5339, 87P473, 87P4264, 88P2535, 86P4603, 85P4569, 86P1994, 87P1087, 87P2376, 87P757, 87P4453, 85P3707	Mixed particles <2000 μm	ASTER spectral library/soil_jhu_becknic	*Baldridge et al.*, 2009, *Kokaly et al.*, 2017
Grey sand	HWWB100/B102/B104/B106	Unk	JSC	
Tephra/ash	HWSP801	Unk	JSC	
	HWSP903	Unk	JSC	
	HWSP905	Unk	JSC	
Mars regolith simulant	JSC Mars-1	<45 μm, 500-1000 μm	JSC	
Minerals				
Olivine	HW12HP006	<150 μm, 500-1000 μm	JSC	
Olivine	HW12HP012	<150 μm, 500-1000 μm	JSC	
Olivine	HW14MK001	<150 μm, 500-1000 μm	JSC	
Olivine	OLSC1	45-90μm, 500-1000 μm	JSC	
Olivine	OLV-SC	<25 μm, 25- 45 μm, < 45μm, 45-63 μm, 45-75 μm, 63-75 μm, 75-106	RELAB	*Ehlmann et al.*, 2008

		μm, 75-125 μm, 106-125 μm, 125-250 μm, 250-500 μm		
Olivine	Los Angeles	unk	RELAB	*Dyar et al.*, 2009
Olivine	EETA79001	Unsorted partic.	RELAB	*Dyar et al.,* 2005
Olivine	Chassigny	unk	RELAB	*Dyar et al.*, 2009
Olivine	Nakhla	unk	RELAB	*Dyar et al.*, 2009
Olivine	ALHA77005	<250 μm, unsorted partic.	RELAB	*Dyar et al.*, 2005
Olivine	DH-101	< 45 μm	RELAB	*Dyar et al.*, 2009
Olivine	KBH-94	<45 μm	RELAB	*Dyar et al.*, 2009
Pyroxene	LEW88516	unk	RELAB	*Dyar et al.*, 2005
Pyroxene	Shergotty	unk	RELAB	*Dyar et al.*, 2005
Pyroxene	Zagami	unk	RELAB	*Dyar et al.*, 2005
Pyroxene	ALHA77005	<250 μm, unsorted partic.	RELAB	*Dyar et al.*, 2005
Pyroxene	EETA79001	< 45 μm, unsorted partic.	RELAB	*Dyar et al.,* 2005
Pyroxene	RELAB MS-CMP-015	< 75 μm	RELAB	unk
Pyroxene	RELAB MS-CMP-043	< 75 μm	RELAB	unk
Pyroxene	PYX174	< 45 μm	RELAB	unk
Pyroxene	PYX185	< 45 μm	RELAB	unk
Diopside	DIHUQ1	45-90μm, 500-1000μm	JSC	
Enstatite	BAMNOR1	Unk	JSC	
Augite	AFOLQC1	500-1000μm	JSC	
Augite	HARAUG1	<45 μm, 500-1000μm	JSC	
Labradorite	GemLabr_1-12	45-75 μm, 45-125 μm	RELAB	unk
Labradorite	GemLabr_13	solid	RELAB	unk
Plagioclase	Miyake-jima plagioclase	45-75 μm, 45-125 μm	RELAB	unk
Plagioclase	PLAGWM1	45-90 μm, 500-1000 μm	JSC	
Anorthite	Split Rock anorthite, RELAB PA-CMP-060G/61-D	45-125 μm	RELAB	unk

Albite	BANAB1	45-90 μm, 500-1000μm	JSC	
Bytownite	CBBYT1	Unk	JSC	
Chabazite	CBZAZ	Unk	JSC	
Clinoptilolite	CPTTX1	<45 μm	JSC	
Clinoptilolite	CPTWY2		JSC	
Silica	CFQT21S1	<90 μm	JSC	
Hematite	HW13MK030		JSC	
Hematite	X01741-3	< 56 μm	RELAB	unk
Hematite	RELAB RH-CMP-007	500 – 1180 μm	RELAB	unk
Goethite	MIT #7122A	unk	RELAB	*Bishop et al.*, 1993
Chlorite	CHLCLV1	Unk	JSC	
Chlorite	MMQMI1	Unk	JSC	
Nontronite	API33A	Unk	JSC	
Saponite	Ballarat	Unk	JSC	
Montmorillo-nite	SAz-1	Unk	JSC	
Ferruginous smectite	SWa-1	Unk	JSC	
Epsomite		125-500 μm	ASTER spectral library/ mineral_usgs_perknic	*Baldridge et al.*, 2009, *Kokaly et al.*, 2017
Hexahydrite		125-500 μm	ASTER spectral library/ mineral_usgs_perknic	*Baldridge et al.*, 2009, *Kokaly et al.*, 2017
Anhydrite		125-500 μm	ASTER spectral library/ mineral_usgs_perknic	*Baldridge et al.*, 2009, *Kokaly et al.*, 2017
Bassanite		125-500 μm	ASTER spectral library/ mineral_usgs_perknic	*Baldridge et al.*, 2009, *Kokaly et al.*, 2017
Gypsum		125-500 μm	ASTER spectral library/ mineral_usgs_perknic	*Baldridge et al.*, 2009, *Kokaly et al.*, 2017
Carbonate	SIDCL02	45-90 μm, 500-1000 μm	JSC	

The ASTER spectral library was developed to assist with data analysis from the ASTER instrument onboard the Terra satellite and the ECOSTRESS mission onboard the International

Space Station. (Since the time of its inclusion in ENVI's spectral libraries, it has been renamed the ECOSTRESS spectral library.) It includes natural and manmade materials in solid form and in multiple grain sizes. Sources for spectra include contributions from the Jet Propulsion Laboratory, Johns Hopkins University, and the US Geological Survey. The Johns Hopkins University spectral library samples include basalts, basaltic andesites, and gabbros in solid and fine particle form, and soils. The USGS spectra included in our library are from hydrated sulfate samples.

The RELAB spectroscopy facility is located at Brown University. Spectral and sample documentation is available for download from their website (www.planetary.brown.edu/relab). We use samples of basalts and gabbros as well as olivine, pyroxene, plagioclase, and iron oxides, collected over a number of years by different investigators.

Observations were made at JSC by Richard Morris. The library samples coded 'HW' are samples that were collected from Hawaii. These include palagonitic tephra samples from Mauna Kea volcano, hematite-rich soils, and beach sand. JSC Mars 1 is a regolith simulant derived from volcanic ash from a Hawaiian cinder cone, deliberately chosen as its VNIR spectral properties are similar to bright regions on Mars [*Allen et al.*, 1998]. Also included are synthesized basaltic glass with composition similar to Adirondack-class rocks in Gusev Crater, the Spirit rover landing site [*Peretyazhko et al.*, 2015], Martian meteorite EET79001, a shergottite collected in Antarctica, and a number of pure mineral phases. The library includes materials that were artificially dehydrated using N_2, resulting in greatly reduced water-related band depths.

3.6 Blind Test of the Method

We conducted several "blind" tests to evaluate the ability of our neural network method to retrieve temperature and SSA. In these cases, we used the neural network to retrieve temperature maps and cubes of laboratory spectra that we generated. Temperatures were varied across the

scene. Spectra to be retrieved were chosen from by extracting a test set from a subset of the linear combinations of laboratory spectra that make up the training data. The neural network was first trained identically as if for a regular CRISM scene. The test set spectra were converted to produce a CRISM-like I/F using the DISORT lookup table. This I/F cube was constructed such that each pixel uses a spectrum combined with the temperature ramp value and i, e, and g from a real CRISM scene. The simulated I/F cube was then run through the trained neural network to try to reconstruct the input "SSA". The outputs were a temperature map and an SSA cube.

Results from one of these exercises using FRT0001FD99 are displayed in Figure 3.5. In this case the temperature map was generated randomly within a range of 250 to 300 K. For 95% of the retrieved temperatures, results are within 3.1 K of actual (Figure 3.5a). The effect of temperature differences on spectra is greater for higher temperatures (Figures 3.5b-d). We find that spectral retrievals are robust to ~3.4 μm except in extreme cases.

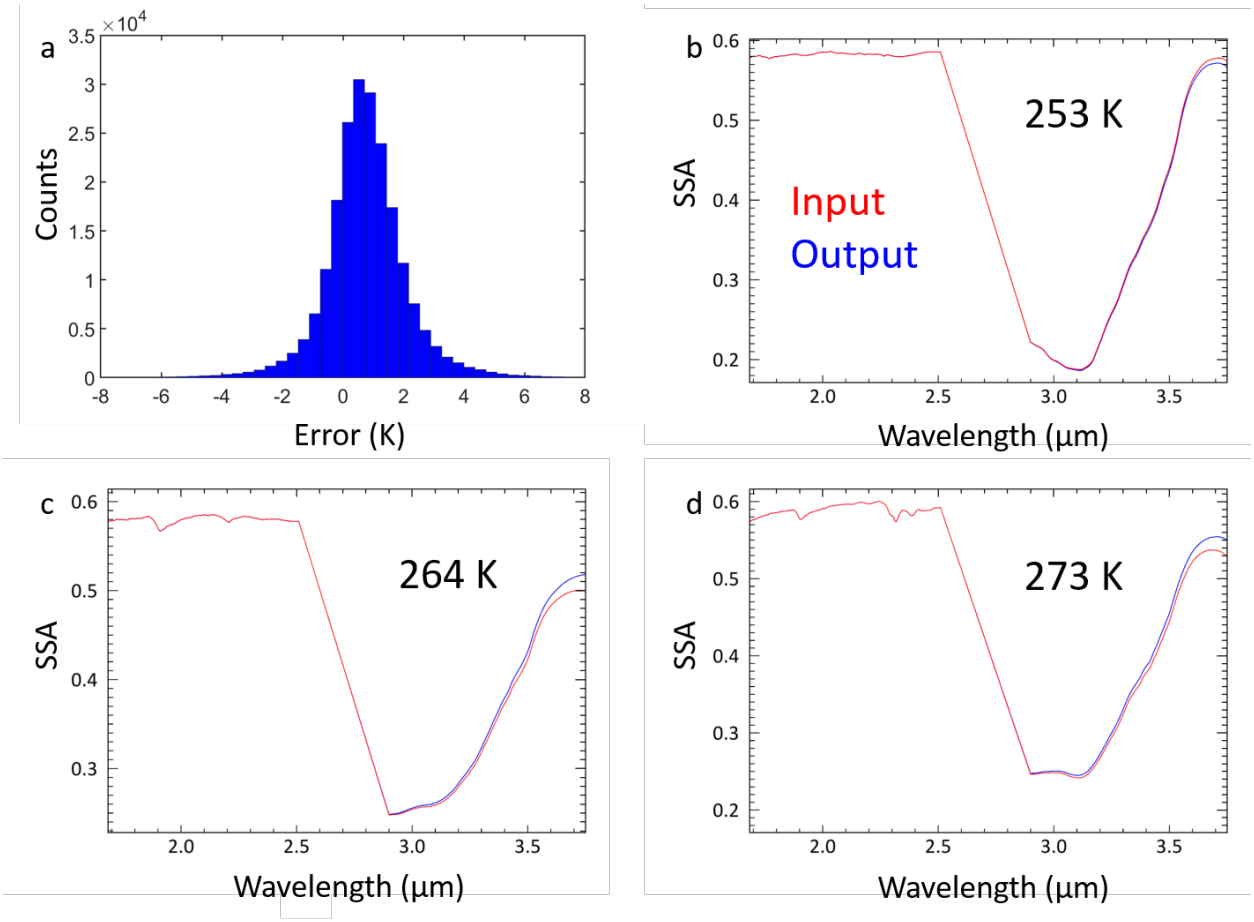

Figure 3.5: Results of one of the blind tests of the neural network. In a blind test, the neural network attempts to retrieve known SSAs and T so the error can be evaluated. In this case the SSAs are an extracted portion of the combined spectra from the training set. The temperature is randomly assigned within a range. a) Error in temperature for the generated scene, T(input) – T(output). 95% of the derived temperatures are within 3.1 K of actual. b) Input and output spectra with short wavelength albedos ~0.6 and derived temperature errors of ~2 K, for T(input) = 253. c) T(input) = 264 K. d) T(input) = 273 K. Temperature errors are more significant to long wavelength spectra for higher temperatures.

These do not give a quantitative assessment of the error in retrieving temperatures from CRISM data, in that they ask the neural network to retrieve laboratory spectra rather than real CRISM data. However, they provide a sense of the effect of temperature on retrievals and the overall utility of the method. We are consistently able to reconstruct known temperature values to within a few K of the true temperature.

3.7 Temperature Mapping

3.7.1 Previous Studies of Gale Crater Thermophysical Properties

Our neural network method produces a map of the temperature value at each pixel in the CRISM scene. When map projected to 12-36 m/pixel, these are the highest resolution temperature maps available of the Martian surface. We evaluate our derived CRISM temperatures with respect to measurements by other instruments. We aim to determine how well relative temperatures in the scene correspond to known physical properties for given locations, as well as how the absolute magnitude of the temperatures compares to those derived from other instruments.

Temperature patterns in the CRISM scene are affected both by the topography of the surface and by the thermophysical properties of materials (Figure 3.6). Thermal inertia is a measure of a material's ability to resist changes in temperature. It is defined as $TI = (k\rho c)^{1/2}$, where k is the thermal conductivity, ρ is the density, and c is the specific heat of the material. Observed temperatures can be used to model the thermal inertia of surfaces by comparison with a thermal model [*Christensen et al.*, 2003; *Fergason et al.*, 2006]. Thermal inertia was quantitatively derived for the MSL landing site and expected traverse on Mount Sharp using THEMIS nighttime IR by *Fergason et al*. [2012]. Most of the landing ellipse has moderate thermal inertias (250 to 410 J m^{-2} K^{-1} $s^{-1/2}$), with some areas reaching 555 J m^{-2} K^{-1} $s^{-1/2}$. This is interpreted as crater floor material variably overlain by mantling material, and is consistent with Curiosity's observations of surface properties [*Arvidson et al.*, 2014]. On Mount Sharp, the Greenheugh pediment has high thermal inertia (520-605 J m^{-2} K^{-1} $s^{-1/2}$) and the clay-rich and intermediate clay-sulfate units have thermal inertias in the range 385-455 J m^{-2} K^{-1} $s^{-1/2}$. The layered sulfates have moderate thermal inertias that range from 260-420 J m^{-2} K^{-1} $s^{-1/2}$and the dust stones exposed on the upper parts of Mount Sharp have low thermal inertia (120-260 J m^{-2} K^{-1} $s^{-1/2}$).

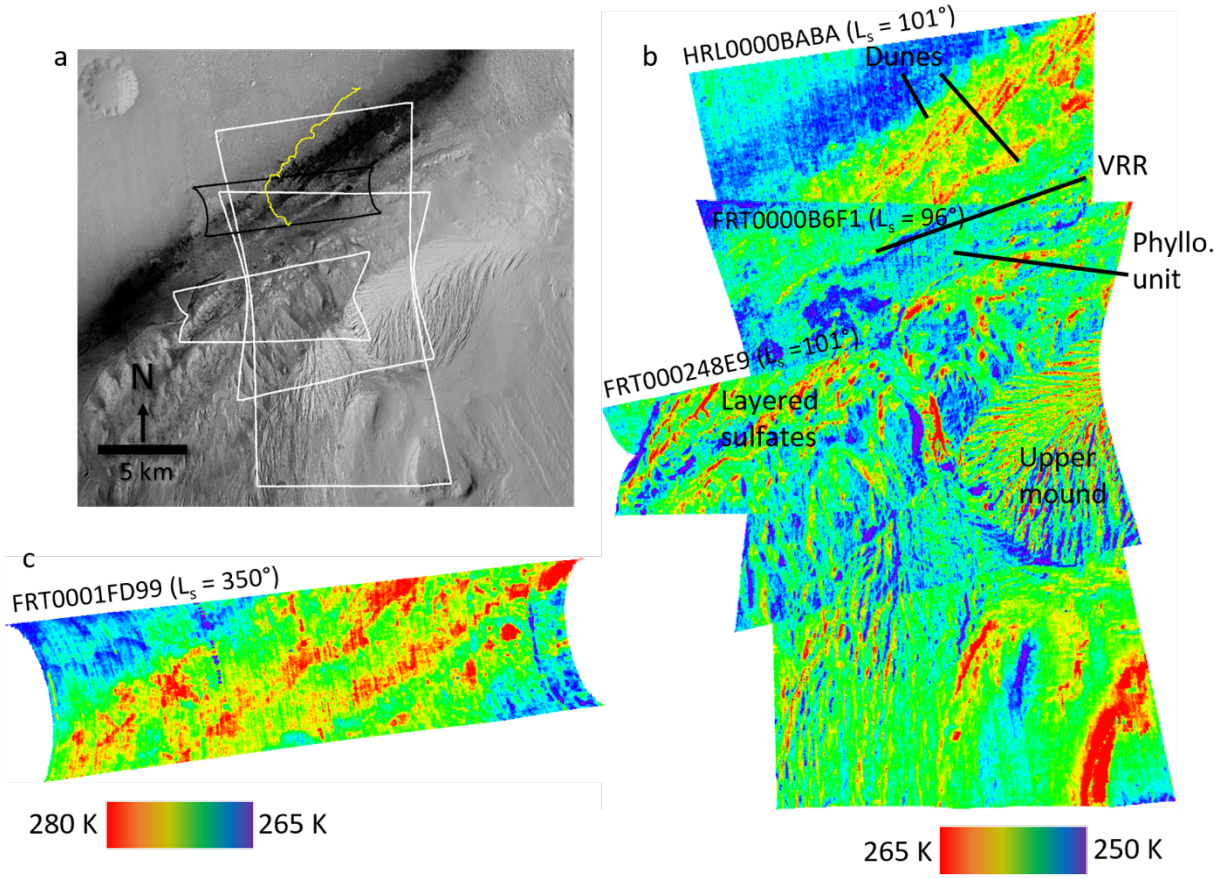

Figure 3.6: The four CRISM scenes used in this study and their neural network derived temperature maps. a) Footprints of the four CRISM scenes used in this study overlaid on a HiRISE mosaic. The four scenes outlined in white are winter scenes, while the scene outlined in black is a summer scene. b) Temperatures derived from HRL0000BABA, FRT0000B6F1, and FRT000248E9, all winter scenes. c) Temperatures derived from CRISM scene FRT0001FD99, a summer scene. Temperature maps for the same season are broadly consistent, with differences of a few K likely due to day-to-day temperature variations.

On the crater floor near Mount Sharp is a southwest-northeast trending unconsolidated deposit known as the Bagnold dunes, an active aeolian dune field [*Silvestro et al.*, 2013]. *Fergason et al.*, [2012] report thermal inertias (250- 315 J m^{-2} K^{-1} $s^{-1/2}$) for the dunes. *Edwards et al.* [2018] compare THEMIS-derived thermal inertias of the Bagnold dunes to thermal inertias derived from REMS. Using THEMIS nighttime IR data over the entire Bagnold dune field, they report a range of thermal inertias of 200-310 J m^{-2} K^{-1} $s^{-1/2}$with an average of 240 J m^{-2} K^{-1} $s^{-1/2}$. Their REMS-

derived thermal inertias, derived only from targets on Namib dune, range from 170-200 J m^{-2} K^{-1} $s^{-1/2}$.

3.7.2 CRISM Temperature Patterns

We have derived temperatures and SSA spectra for four CRISM scenes over Gale Crater (Table 3.1). While dozens of CRISM scenes have been acquired over Gale, we focus on those that substantially overlap the Curiosity traverse. We also require that scenes have a low dust opacity (~0.8 or less), as dust aerosols can interfere with the accuracy of surface temperature and albedo retrievals. Three of these CRISM observations were acquired during the southern hemisphere winter, at solar longitude (Ls) ≈ 100°. The fourth provides contrast as it was acquired during southern hemisphere summer.

Of the three winter scenes, FRT0000B6F1 and FRT000248E9 cover lower Mount Sharp while HRL0000BABA covers part of the crater floor and lower and upper Mount Sharp at lower spatial resolution. In temperature maps created from these three scenes, west-facing sunlit slopes are warmer than their surroundings, consistent with the ~15:15 LST observation times. The western faces of layered sulfate mounds, the western edge of Vera Rubin Ridge, and ridges in the upper Mount Sharp section are easily distinguished by their elevated temperatures. The Bagnold dunes have relatively high temperatures, as do more localized sand patches within small impact craters, consistent with low thermal inertias. In the area where all three scenes overlap (Figure 3.6b), temperature differences between scenes typically vary from 1-5 K, with more scatter for cooler temperatures. The three scenes were taken on different days, and some real temperature differences between them are expected.

The summer scene, FRT00001FD99 is an along-track oversampled CRISM observation and covers a smaller area than the other three scenes, centered on the Bagnold dunes. The

distribution of temperatures observed in FRT0001FD99 are consistently higher than the other three scenes, as expected for summer versus winter surface temperatures (Figure 3.6c). Peak temperatures for the dune surfaces are ~280 K versus ~265 K in HRL0000BABA. However, the overall patterns between FRT0001FD99 and the other scenes remain consistent. Overall, the temperature patterns in CRISM scenes are correlated with topographic and geologic features and appear consistent within and between individual scenes.

3.7.3 THEMIS

We also compared our CRISM-derived temperatures to products created from orbital thermal emission spectroscopy. THEMIS, the thermal emission spectrometer aboard the Mars Odyssey orbiter [*Christensen et al.*, 2004], has acquired dozens of daytime IR images over Mount Sharp. THEMIS has nine bands in the thermal emission wavelength region, from 6.8 to 14.9 μm, where the reflection component is completely negligible. The spatial resolution is 100 m/pixel and therefore THEMIS pixels are more likely to cover multiple materials with different thermal properties than CRISM's 12-36 m pixels.

THEMIS daytime IR spectral radiance patterns are a proxy for the temperature of the daytime surface. Daytime IR observations mimic visible imagery acquired at the same time, as topographic features are distinguishable by the variation in solar heating by azimuth. Thermophysical properties have a secondary effect.

We compare HRL0000BABA to THEMIS scenes from Ls ≈ 100°. The CRISM temperature patterns are broadly similar to patterns in daytime THEMIS IR calibrated radiance images. During the afternoon period when CRISM and THEMIS images are acquired, incident solar radiation has heated the surface to different degrees, allowing us to distinguish geologic features with different TI (Figure 3.7). In both data sets, the low-TI Bagnold dunes appear brighter

than the surrounding higher-TI bedrock. However, CRISM is able to resolve dune faces more clearly than THEMIS. In contrast to the dunes, the Greenheugh pediment, a high-TI surface, appears relatively cool, whereas unconsolidated material on its surface appears warmer. The higher spatial resolution of CRISM can more clearly resolve spatially smaller features such as Vera Rubin Ridge and the mounds of the layered sulfate unit.

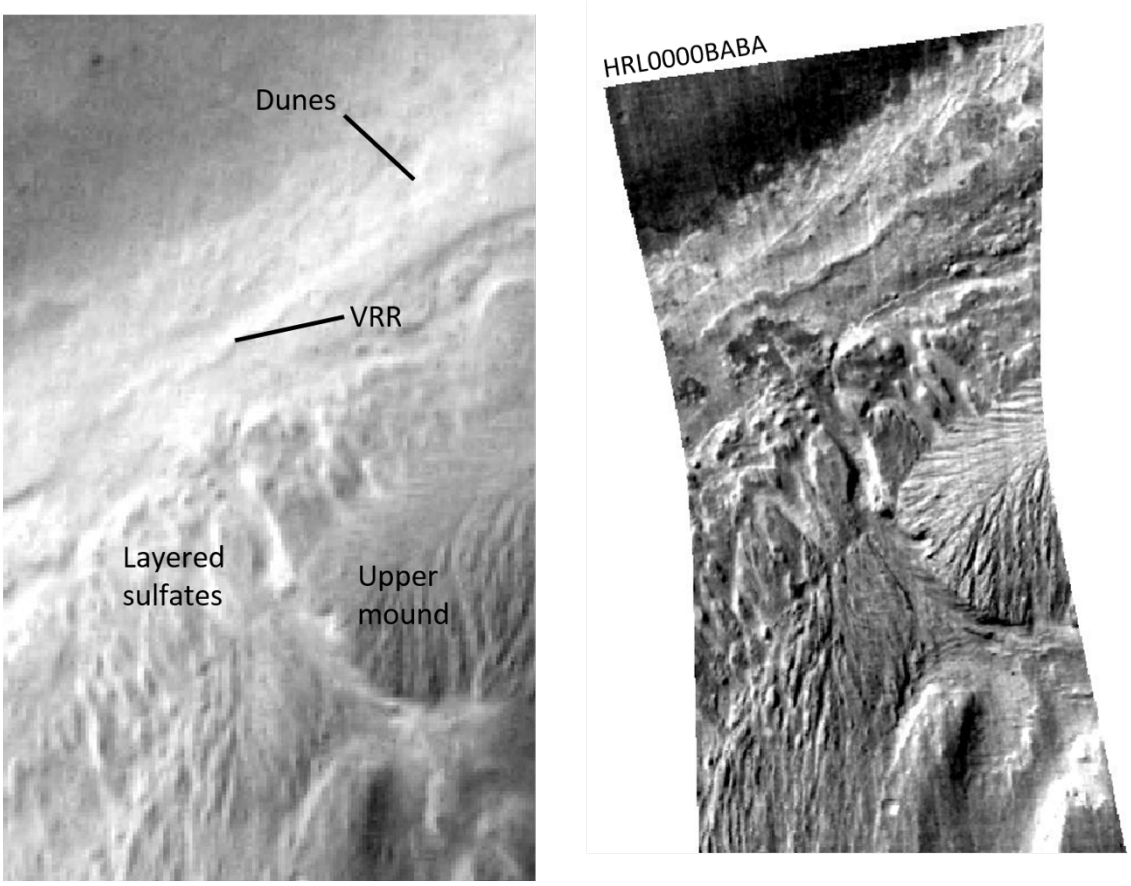

Figure 3.7: CRISM- and THEMIS-derived temperatures from L_s ≈100°. Left: THEMIS projected brightness temperature, PBT I54337024. Right: HRL0000BABA temperatures. Temperature patterns are broadly consistent between the two data sets. Low thermal inertia features, such as dunes, are bright, and sun-facing slopes are bright. CRISM is able to resolve smaller spatial features than THEMIS, such as Vera Rubin Ridge and the sulfate-bearing mounds of lower Mount Sharp.

THEMIS brightness temperatures approximate the surface kinetic temperature at the time of the observation. Brightness temperatures are derived by fitting a Planck curve to radiance from Band 9 (12.57 μm), which has high signal-to-noise and is relatively transparent to dust in the

atmosphere [*Fergason et al.*, 2006]. This calculation assumes that in Band 9 the surface emissivity is 1 and the atmospheric opacity is 0 [*Christensen et al.*, 2017]. This simple method for deriving brightness temperature will underestimate true surface temperatures, in that the atmosphere absorbing and scattering at these wavelengths will result in reduction of surface emittance. Despite the similarities in the two data sets, overall the magnitude of CRISM-derived temperatures is higher than THEMIS brightness temperatures from the same season. Although the THEMIS brightness temperatures may be lower than the true surface temperature, this effect is also likely a result of the different times of day that the THEMIS and CRISM observations are acquired. CRISM targeted observations are acquired around 15:00-15:30 local solar time (LST) while THEMIS is acquired between 17:00 and 18:00 LST. The daytime surface temperature of the Martian surface peaks between 12:00 and 14:00. The CRISM observation time is much closer to this peak and the observed temperatures are expected to be warmer. The similarity in spatial patterns and divergence in temperature magnitude between the two data sets indicates that the CRISM-derived temperatures are reasonable.

3.7.4 REMS GTS

We also compare CRISM temperature results to ground-based measurements made along the MSL traverse. The REMS instrument [*Gómez-Elvira et al.*, 2012] measures environmental conditions including wind speed, air temperature, pressure, humidity, and ground temperature for five minutes during every hour of every sol. The REMS Ground Temperature Sensor (GTS) is a pyrometer sensitive to emission in the 8-14 μm range [*Sebastián et al.*, 2010]. The GTS is located on a fixed boom and therefore always points in the same direction relative to the rover. Its observed footprint is on the order of 100 m^2 but the precise area varies with the roll of the vehicle [*Hamilton et al.*, 2014]. The GTS measured brightness temperature is expected to be somewhat lower than

the true surface kinetic temperature due to the non-unity emissivity of the observed surface materials [*Sebastián et al.*, 2010]. REMS observations from the same season in multiple Mars years vary likely as result of both weather fluctuations and the different thermal properties of surfaces observed along the traverse.

We use the CRISM scene that covers the largest spatial area over the traverse and Mount Sharp, HRL0000BABA to compare to REMS data. This scene was acquired in July 2008 at L_s = 101° at 15:21 and has a nominal spatial resolution of 36 m/pixel. As this scene was acquired more than four years before MSL landed, we are unable to make a direct comparison to concurrent REMS GTS observations. Instead we compare the available REMS measurements from the same L_s and LST to the CRISM pixels covering the appropriate area of the traverse. Three years of REMS GTS observations are available at the same season as HRL0000BABA (Figure 3.8). For comparison we used a period of five consecutive sols in each year, centered at L_s = 101°. We fit a second-order polynomial to REMS observations between LST = 12:00-18:00 to retrieve the temperature at the same time of day that HRL0000BABA was acquired.

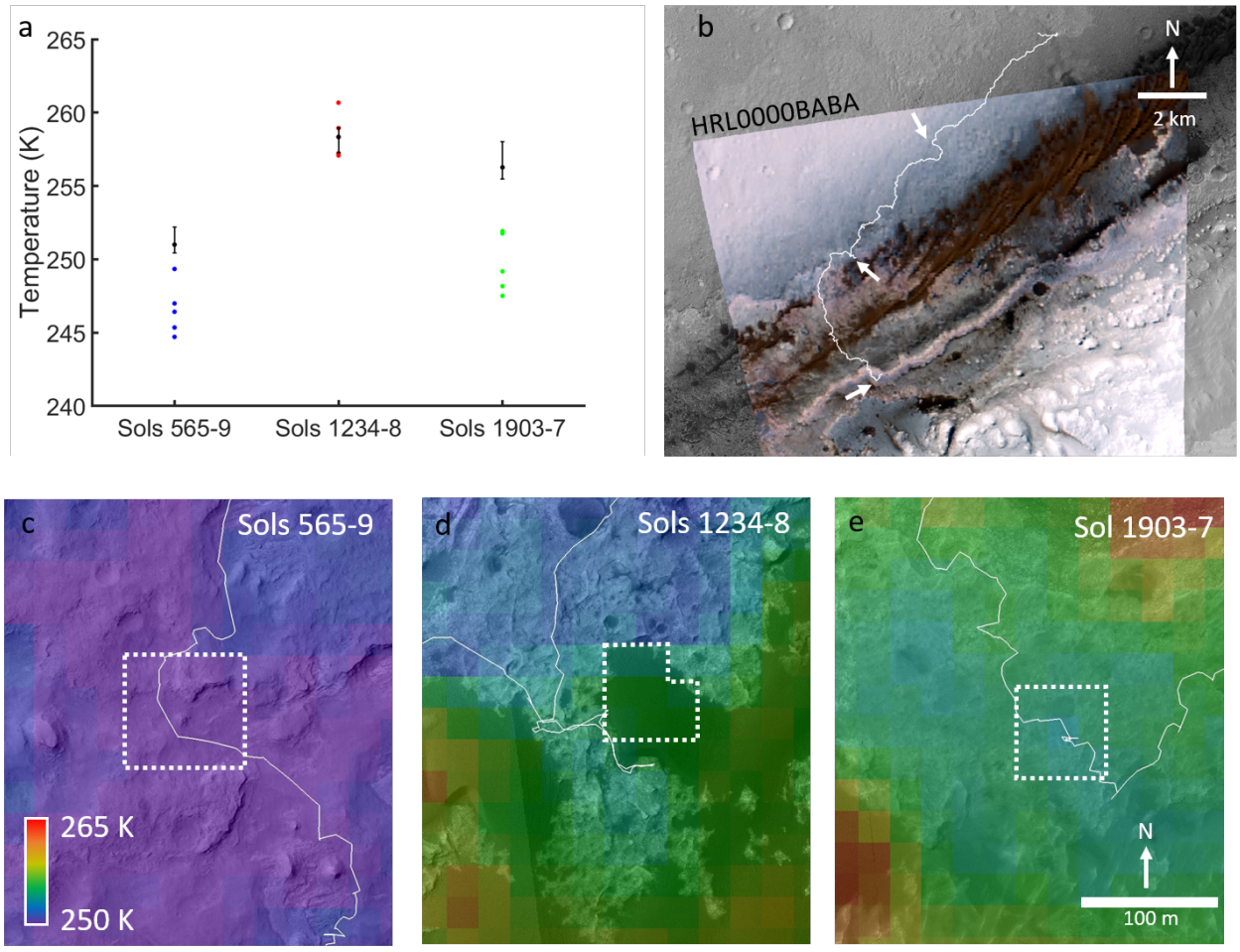

Figure 3.8: Comparison of CRISM HRL0000BABA neural network-derived temperatures with observed temperatures by REMS GTS in the same season, L_s = 101°, in the three available Mars years. a) Plot of CRISM-derived temperatures (black) for approximate GTS field of view versus GTS-derived temperature (colored dots). b) HRL0000BABA with MSL full traverse and three sites denoted with arrows. c-e) HiRISE mosaic with HRL0000BABA pixels used overlaid. Location of Curiosity at the same L_s in each Martian year of the mission, captured on five successive sols with approximate GTS orientation.

During the first period in Mars Year (MY) 32, Sols 565-569, Curiosity was driving across the plains of Gale Crater below Mount Sharp. REMS GTS observations during this period were taken at multiple azimuths. As the plains are relatively flat, there is some uncertainty in the exact area covered by the REMS field of view during this five-sol period. We therefore chose an area surrounding the traverse for comparison (Figure 3.8c), including 16 pixels. CRISM-derived temperatures from this area are higher than those reported by REMS. The expected temperature at 15:21 ranges from 244.7 to 249.3 K, whereas the average CRISM temperature is 251.0 K.

In MY 33 at L_s = 101°, Curiosity was conducting its Bagnold Dunes campaign. During sols 1234-1238, Curiosity was stationary with GTS pointed at the face of Namib dune. The REMS observations taken over this period have the highest temperatures of the three MY, consistent with the warm temperatures expected for a low thermal inertia sand unit in midafternoon. In fact, examining the REMS seasonal temperature curves throughout the mission thus far, the period while parked at Namib dune represents a marked deviation in temperature from both the rest of the observational trend and the modeled temperature curve. The daytime maximum temperature is elevated and the nighttime minimum temperature is depressed [*Vasavada et al.*, 2017]. The GTS measurements also have the least scatter of the three MY. This is likely due to observing the same materials for several sols, leaving only the day-to-day weather variations to cause changes in the GTS observed temperature. From the CRISM data we chose to extract temperatures only from 8 pixels to the east of Curiosity's location, covering the dune (Figure 3.8d). CRISM results fall within the scatter of GTS results. The range of expected GTS temperatures was 257.2 to 260.7 K, whereas the average from CRISM was 258.4 K.

During sols 1903-1907, Curiosity was driving on Vera Rubin Ridge. The direction of observation is again variable and the surface area measured by GTS is not well constrained. The CRISM-derived temperatures are warmer than the REMS data. The average CRISM temperature over 9 pixels was 256.3 K whereas the range of REMS temperatures was 247.5 to 251.9 K (Figure 3.8e).

CRISM-derived temperatures are higher than REMS GTS measurements for two of the three Mars years observed. A possible explanation for the discrepancy is the very different fields of view of the two instruments. CRISM HRL0000BABA was acquired at an incidence angle of 57.3° relative to a flat surface (a poor approximation for Mount Sharp), looking down on the tops

of features and insensitive to surface structures <~50 m/pixel. REMS is observing surfaces at an oblique angle at much smaller scales. It is more likely to capture the sides of features, which may receive less incident sunlight than the tops. It is also possible that these few sols in MY 32 and 34 were simply warmer than in MY 29.

All of the CRISM-derived temperatures are in good agreement with REMS. The discrepancies can be explained by the non-modeled emissivity, uncertainty in terrains observed in the REMS observations, possible errors introduced by the CRISM calibration, and possible true differences in temperature in different years.

Observations by CRISM, THEMIS, and REMS build a self-consistent picture of the thermal environment in Gale Crater. Figure 3.9 shows the diurnal curves for Sol 567 (MY 32) and Sol 1905 (MY 34) and temperatures derived from CRISM and THEMIS observations from the same L_s. The differences between the two REMS curves likely result from both different materials observed and differences in weather in the two years. The effect of the later THEMIS observing time is evident in its lower temperatures for the same L_s. Temperatures on the ridge are slightly lower than those on the plains for all three instruments.

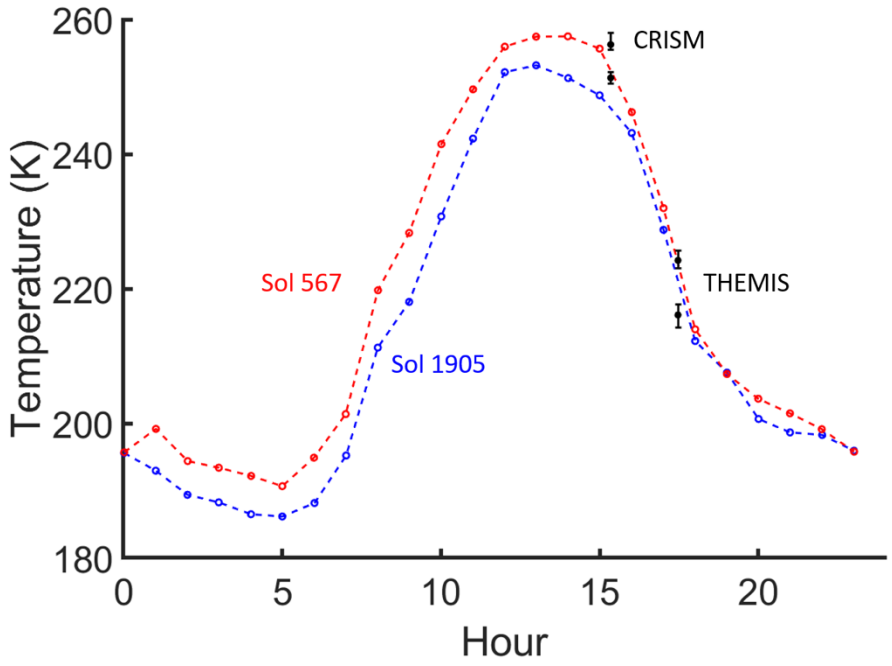

Figure 3.9: Comparison of temperatures from CRISM, THEMIS, and REMS GTS. Dashed lines show REMS diurnal temperature curves for Sol 567 and Sol 1905, both L_s = 101°. We omit Sol 1236 due to the very different thermal properties of Namib dune. Dots at LST = 15.35 show the range of temperatures for regions of interest in HRL0000BABA. Dots at 17.47 show the range of temperatures for regions of interest from THEMIS PBT I54337024, also at L_s = 101°. THEMIS ROIs cover ~20 pixels each and thus represent a larger spatial area than the CRISM or REMS measurements. The effect of THEMIS's later observing time can be seen in the much lower temperatures it observes for the same season.

3.8 Measuring the 3 μm Absorption

Our thermally-corrected SSA spectra can be used to measure spectral features for $\lambda > 2.6$, particularly the broad OH/H_2O absorption features near 3 μm. All CRISM spectra of Mars contain a 3 μm absorption feature, even areas that do not contain identifiable hydrated minerals. This absorption feature is attributed to adsorbed and absorbed water in minerals, sometimes together with structurally bound OH and H_2O. The 3 μm absorption strength of Mars analog minerals has been observed to increase with adsorption in the laboratory, which does not always correspond to an increase in the depth of the 1.9 μm absorption [*Pommerol et al.*, 2009].

We can correlate the 3 μm band depth and shape to other spectral features in previously mapped units. There are multiple approaches to quantifying the strength of absorption features

near 3 μm. The first is a simple calculation of band depth relative to a continuum, BD = ($R_c(\lambda)$ - $R(\lambda)$)/$R_c(\lambda)$, where R is the reflectance value and R_c is the value at the same wavelength of a continuum fit to either side of the absorption. Similarly, the 3 μm band depth as defined in the BD3000 parameter [*Viviano-Beck et al.*, 2014] measures the band depth at 3.00 μm relative to the slope between 2.21 and 2.63 μm. This parameter does not measure the maximum depth of the feature if the band center is shifted away from 3.00 μm. We find that this parameter is strongly correlated with short wavelength SSA values. Bright surfaces exhibit higher BD3000 values than dark surfaces and it can be difficult to distinguish the relative contribution of albedo and hydration. BD3000 is also highly sensitive to shadowed surfaces. Our CRISM processing method does not model shadows and thus we do not report results from spectra of obviously shadowed surfaces. The high values of band depth mapped in shadowed regions thus create misleading visuals and care must be taken not to over-interpret them.

As the 3 μm feature is deep and has a complex shape, we seek alternative measures of its effect on the overall spectrum. The total band area can also be quantified as either an integrated band depth (IBD) or integrated band area (IBA), which more accurately measures the absorption feature when the band center is shifted away from 3.0 μm. An Integrated Band Depth (IBD) averages the band depth relative to a continuum over a range 2.9-3.8 μm [*Jouglet et al.*, 2007]. Accurate thermal correction is very important, as it will strongly affect the continuum point anchor at 3.7 μm for this absorption strength measure (Figure 3.10). An Integrated Band Area (IBA) sums the contributions of the difference between the continuum and reflectance, again for a range 2.9-3.8 μm [*Liu et al.*, 2012]. We find that a normalized IBA relative to the continuum is less sensitive to the overall albedo [*Pommerol and Schmitt*, 2008].

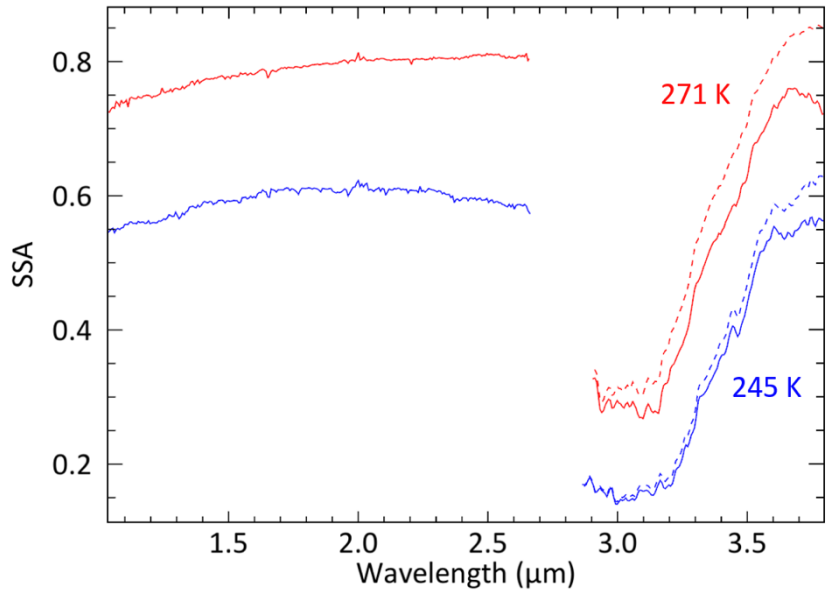

Figure 3.10: CRISM FRT0000B6F1 SSA spectra with and without thermal correction, at 271 K and 245 K. The error associated with lack of thermal correction increases with increasing temperature. This error impacts measurement of the 3 µm feature due to its effect on the continuum slope.

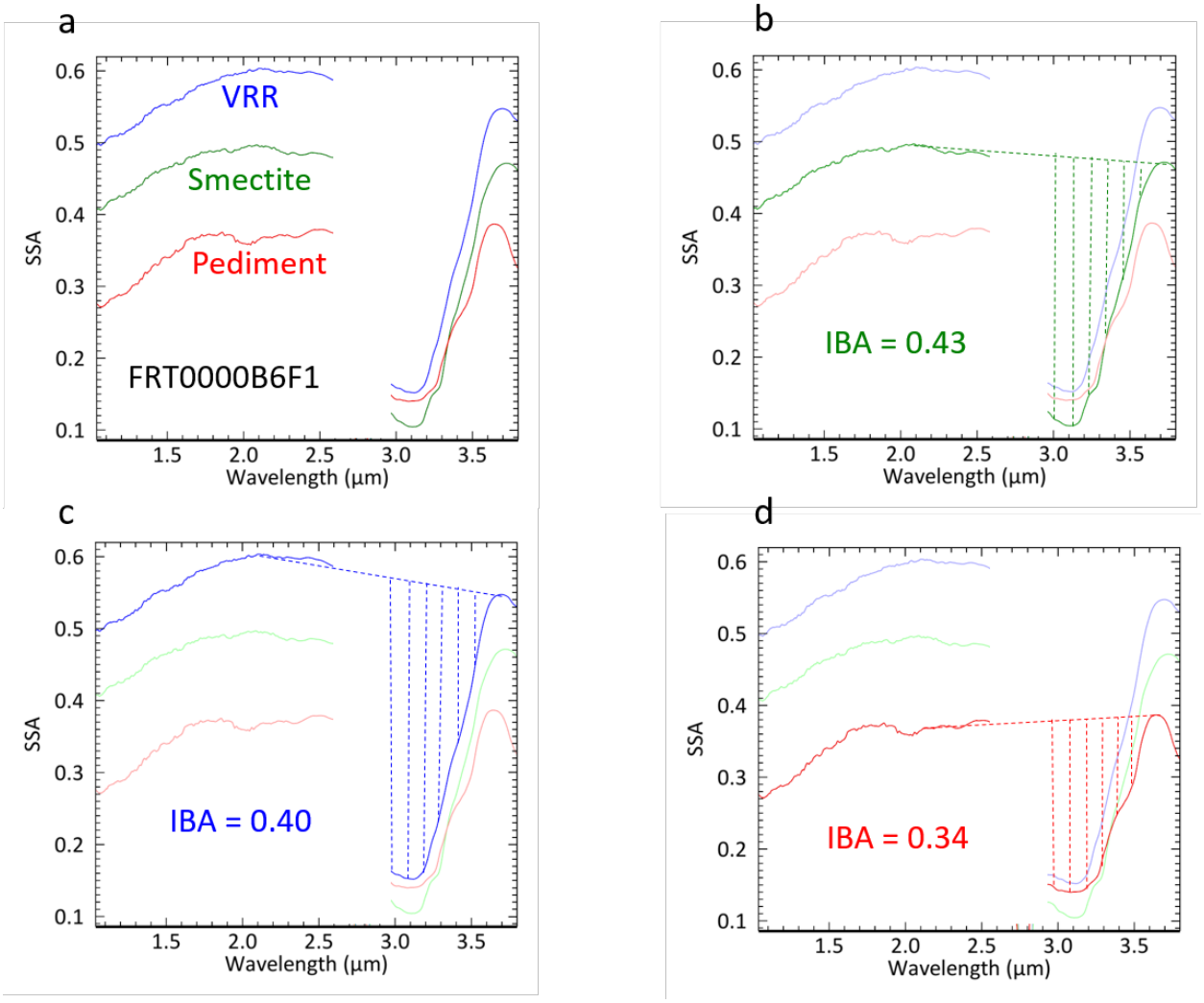

Figure 3.11: Integrated Band Area is a measure of the shape and depth of the 3 μm feature. a) FRT0000B6F1 spectra (5x5 pixel averages) from the smectite-rich unit, Vera Rubin Ridge, and the Greenheugh pediment. b) Example IBA calculation using the smectite spectrum. This feature is both deep and broad and so is calculated as the highest IBA value of the three spectra. c) IBA of Vera Rubin Ridge spectrum. This feature is deep but not as broad as the smectite spectrum. d) IBA of the pediment spectrum. This feature is relatively broad but by far the shallowest of the three spectra, and has a low IBA.

Figure 3.11 shows three examples of the IBA calculation. The continuum was chosen between 2.1 and 3.7 μm. Both the depth and width of the feature contribute to the IBA value. The normalized IBA is less strongly correlated to albedo in the reflectance regime than the band depth parameter.

The strength of the IBA values varies with mineralogy throughout the scene (Figure 3.12). IBA values in the Bagnold dunes range from 0.31-0.35, lower than in the surrounding Murray formation bedrock (0.37-0.45), but still showing a pronounced 3 μm absorption feature. These lower IBA values correspond well to the sharply defined dune surfaces resolved in HiRISE. Vera Rubin Ridge also has a slightly weaker 3 μm IBA (0.36-0.41) relative to the Murray formation directly to its north. This is consistent with the lack of a 1.9 μm absorption nearly everywhere on the ridge. The Greenheugh pediment surface also appears to contain mainly anhydrous phases, with low IBA values of 0.32-0.35. It has some of the lowest 3 μm IBA values in the lower portion of Mount Sharp, and does not exhibit a 1.9 μm absorption.

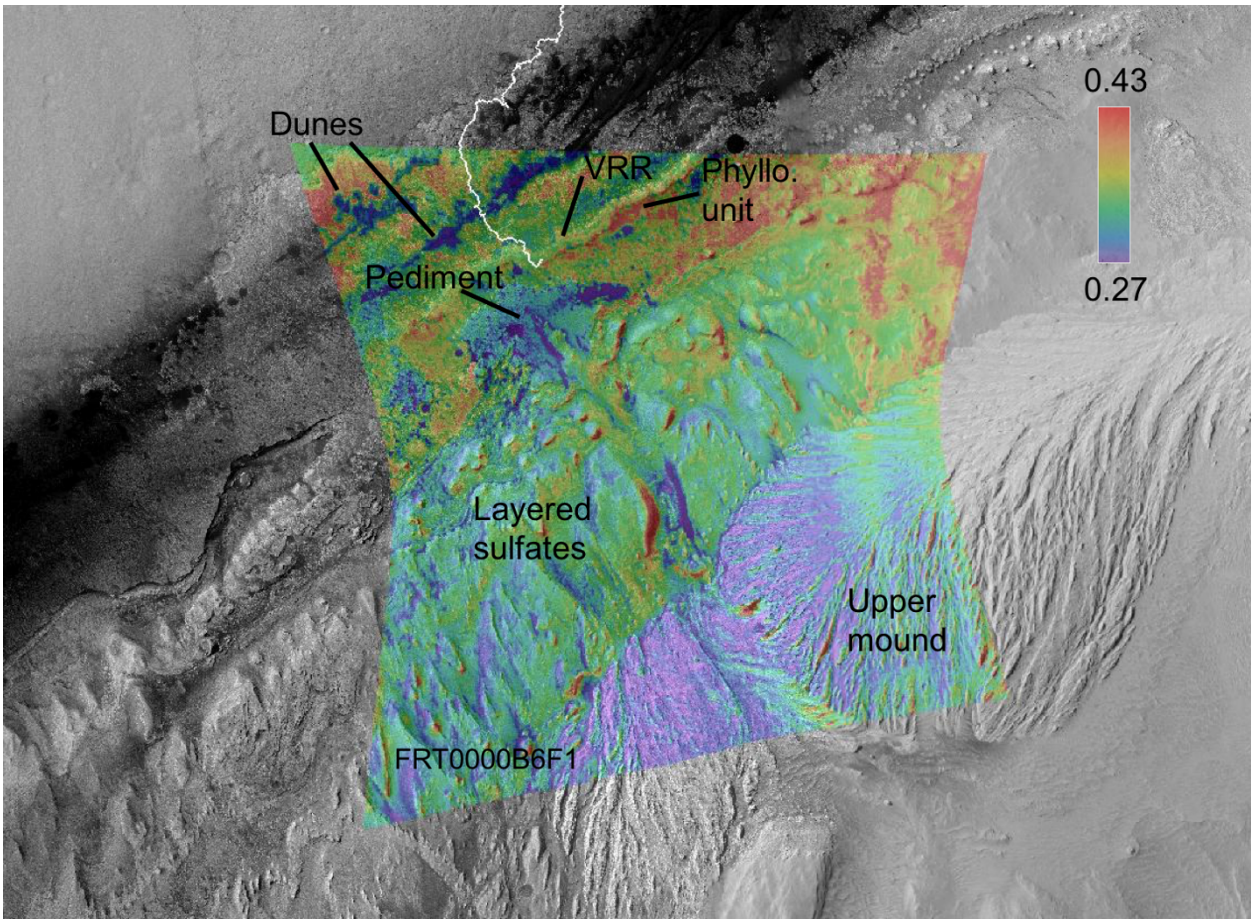

Figure 3.12: Maps of 3 μm Integrated Band Area derived from thermally-corrected FRT0000B6F1, overlaid on HiRISE mosaic. See text for further discussion of band area patterns.

Hydrated minerals have been previously mapped at Gale Crater using the 1.9-2.1 μm OH/H_2O combination and overtone absorptions and 2.1-2.5 μm metal-OH absorption features [*Fraeman et al.*, 2016; *Milliken et al.*, 2010]. We find that many of these regions also have strong 3 μm features, consistent with the presence of hydrated minerals in addition to the ubiquitous sorbed water. The smectite valley within the phyllosilicate unit shows strong evidence of hydration with IBA values 0.40-0.44. Smectites contain interlayer water and can be identified by absorptions at 1.9 μm due to OH/H_2O and metal-OH absorptions between 2.1-2.4, the exact positions of which vary with octahedral sheet cation. Smectites have been previously identified south of Vera Rubin Ridge [*Milliken et al.*, 2010; *Fraeman et al.*, 2016; *Fox et al.*, 2018]. The 3 μm band IBA correlates well with regions of enhanced 1.9 μm band depth and 2.3 μm band depth in the smectite unit. The transition between the smectite-rich unit and layered sulfate unit also shows relatively strong evidence for hydration. The layered sulfate unit itself shows variable IBA parameter values. The anomalously strong values on the southeast sides of mounds correspond to non-modeled slopes in shadow. Local slopes within a CRISM scene are only included at MOLA spatial scales (128 pixels per degree), not including the much finer scale topography present on Mount Sharp. In general, areas between the mounds have a stronger 3 μm feature than the mounds themselves. Above the sulfate strata is a contact with the overlying unit, which have some of the lowest IBA values in the scene (0.28-0.33), consistent with anhydrous dust-stones. Throughout the southwestern portion of the contact the transition is abrupt and closely follows the contact. Overall, the strength of the 3 μm unit is consistent with measures of hydration from the 1.9 μm absorption feature and identification of hydrated minerals using their diagnostic absorption features.

3.9 Conclusions

We retrieve surface albedo in CRISM data from 1-3.8 μm by fully modeling reflectance and emission from the surface and extinction from atmospheric gases and aerosols. To solve the underdetermined problem of mixed surface reflectance and emission at unknown temperatures, we apply a neural network method to simultaneously solve for these multiple variables. To train the neural network we have assembled a training set of laboratory spectra that simulate the possible range of surface materials found on Mars.

The temperatures retrieved represent the highest spatial resolution temperature data set derived from Mars orbital data. The temperatures reported here are derived solely from the CRISM data, not relying on any prior knowledge of the surface temperature from external observations or modeling. These neural network derived temperatures are broadly consistent with observations from other ground-based and orbital instruments that were designed to measure temperature. The variations between data sets are consistent with the different spatial resolutions, fields of view, and observation times, and underlying assumptions used to derive temperatures from these other instruments.

The derived spectra in the form of SSA can be used to quantitatively map 3 μm features. All CRISM spectra have a 3 μm feature due to sorbed water, but the strength of the feature varies with the structural water content of surface minerals. The strength of this feature is observed to be stronger in areas of Mount Sharp where hydrated minerals have been previously identified, and less strong in areas where hydrated minerals are not expected to be a major component. This work opens up the possibility of new capabilities for a rich existing dataset of CRISM observations.

References

Aines, R. D., and Rossman, G. R. (1984), Water in minerals? A peak in the infrared, *J. Geophys. Res.: Solid Earth*, *89*, 4059-4071.

Allen, C. C., Morris, R. V., Jager, K. M., Golden, D. C., Lindstrom, D. J., Lindstrom, M. M., and Lockwood, J. P. (1998), Martian regolith simulant JSC Mars-1, Abstract 1690 presented at the 29th Lunar and Planet. Sci. Conf. Houston, TX, 16-20 March.

Arvidson, R. E., et al. (2014), Terrain physical properties derived from orbital data and the first 360 sols of Mars Science Laboratory Curiosity rover observations in Gale Crater, *J. Geophys. Res: Planets*, *119*, 1322-1344, https://doi.org/10.1002/2013JE004605.

Baldridge, A. M., S.J. Hook, C.I. Grove and G. Rivera, (2009), The ASTER Spectral Library Version 2.0, *Remote Sensing of Environment*, *113*, 711-715, https://doi.org/10.1016/j.rse.2008.11.007.

Bayly, J. G., Kartha, V. B., and Stevens, W. H. (1963), The absorption spectra of liquid phase H2O, HDO and D2O from 0.7 μm to 10 μm, *Infrared Physics*, *3*, 211-222.

Bellucci, G., et al. (2007), Evidence for enhanced hydration on the northern flank of Olympus Mons, Mars, *Icarus*, *192*, 361-377.

Bibring, J. P., et al. (2004), OMEGA: Observatoire pour la Minéralogie, l'Eau, les Glaces et l'Activité. In Mars Express: the scientific payload (Vol. 1240, pp. 37-49).

Bibring, J. P., et al. (2006), Global mineralogical and aqueous Mars history derived from OMEGA/Mars Express data, *Science*, *312*, 400-404.

Bishop, J. L., Pieters, C., and Burns, R. G. (1993), Reflectance and Mössbauer spectroscopy of ferrihydrite-montmorillonite assemblages as Mars soil analog materials, *Geochimica et Cosmochimica Acta*, *57*, 4583-4595.

Christensen, P. R., et al. (2003), Morphology and composition of the surface of Mars: Mars Odyssey THEMIS results, *Science*, *300*, 2056-2061.

Christensen, P. R., et al. (2004), The thermal emission imaging system (THEMIS) for the Mars 2001 Odyssey mission, *Space Science Reviews*, 110(1-2), 85-130.

Christensen, PR. (2017), 2001 Mars Odyssey Thermal Emission Imaging System (THEMIS) Data Processing User's Guide, Part 1 – Infrared. Version 0.23. Retrieved from viewer.mars.asu.edu/content/documents (5-8-2018).

Dyar, M. D., A. H. Treiman, C. M. Pieters, T. Hiroi, and M. D. Lane (2005), MIL03346, the most oxidized martian meteorite: A first look at petrography, mineral chemistry, and spectroscopy, *J. Geophys. Res*., 110, E09005, doi: 10.1029/2005JE002426.

Dyar, M. D., et al. (2009), Spectroscopic characteristics of synthetic olivine: An integrated multi-wavelength and multi-technique approach, *American Mineralogist*, *94*, 883-898.

Edgett, K. S., (2012), Curiosity's Mars hand lens imager (MAHLI) investigation, *Space Science Reviews*, *170*, 259-317.

Edwards, C. S., et al. (2018), The thermophysical properties of the Bagnold dunes, Mars: Ground-truthing orbital data, *J. Geophys. Res: Planets*, 123, 1307–1326, https://doi.org/10.1029/2017JE005501

Ehlmann, B. L., J. F. Mustard, S. L. Murchie, F. Poulet, J. L. Bishop, A. J. Brown, W. M. Calvin, R. N. Clark, D. J. Des Marais, R. E. Milliken, L. H. Roach, T. L. Roush, G. A. Swayze, and J. J. Wray (2008), Orbital identification of carbonate-bearing rocks on Mars, *Science*, *322*, 1828-1832, doi: 10.1126/science.1164759.

Ehlmann, B. L., and Edwards, C. S. (2014), Mineralogy of the Martian surface, *Annual Review of Earth and Planetary Sciences*, *42*, 291-315.

Erard, S., and Calvin, W. (1997), New composite spectra of Mars, 0.4–5.7 μm, *Icarus*, *130*, 449-460.

Falk, M., and Ford, T. A. (1966), Infrared spectrum and structure of liquid water, *Canadian Journal of Chemistry*, *44*, 1699-1707.

Fox, V. K., Bennett, K. A., Vasavada, A. R., Stack, K. M., and Ehlmann, B. L. (2018), The Clay-Bearing Unit of Mount Sharp, Gale Crater, I: Orbital Perspective and Initial Results. In Lunar and Planetary Science Conference (Vol. 49).

Fraeman, A. A., et al. (2016), The stratigraphy and evolution of lower Mount Sharp from spectral, morphological, and thermophysical orbital data sets. *J. Geophys. Res: Planets*, *121*, 1713-1736.

Gendrin, A., et al. (2005), Sulfates in Martian layered terrains: the OMEGA/Mars Express view, *Science*, *307*, 1587-1591.

Fergason, R. L., Christensen, P. R., and Kieffer, H. H. (2006), High- resolution thermal inertia derived from the Thermal Emission Imaging System (THEMIS): Thermal model and applications, *J. Geophys. Res: Planets*, *111*, E12004, doi:10.1029/2006JE002735.

Gómez-Elvira, J., et al. (2012), REMS: The environmental sensor suite for the Mars Science Laboratory rover, *Space Science Reviews*, *170*, 583-640.

Grotzinger, J. P., et al. (2012), Mars Science Laboratory mission and science investigation, *Space Science Reviews*, *170*, 5-56.

Grotzinger, J. P., et al. (2015), Deposition, exhumation, and paleoclimate of an ancient lake deposit, Gale crater, Mars, *Science*, 350(6257), aac7575, doi: 10.1126/science.aac7575

Hamilton, V. E., et al. (2014), Observations and preliminary science results from the first 100 sols of MSL Rover Environmental Monitoring Station ground temperature sensor measurements at Gale Crater, *J. Geophys. Res: Planets*, *119*, 745-770.

Hapke, B. (2012), Theory of Reflectance and Emittance Spectroscopy, Cambridge Univ. Press, New York.

He, L., et al. (2017), Resolution Analysis of Regularized Maximum Log-likelihood Reconstruction Method for CRISM Hyperspectral Data. In Propagation Through and Characterization of Atmospheric and Oceanic Phenomena, *Optical Society of America*, paper JTu5A-16.

He, L., R.E. Arvidson and J.A. O'Sullivan (2018), Retrieving Single Scattering Albedos and Temperatures from CRISM Hyperspectral Data Using Neural Networks, Planetary Science and Informatics and Data Analytics, St. Louis, MO, Abstract #6052.

Houck, J. R., Pollack, J. B., Sagan, C., Schaack, D., and Decker Jr, J. A. (1973), High altitude infrared spectroscopic evidence for bound water on Mars, *Icarus*, *18*, 470-480.

Jouglet, D. et al. (2007), Hydration state of the Martian surface as seen by Mars Express OMEGA: 1. Analysis of the 3 μm hydration feature, *J. Geophys. Res.: Planets*, *112*, E08S06, doi: 10.1029/2006JE002846.

Kokaly, R.F., et al. (2017), USGS Spectral Library Version 7: U.S. Geological Survey Data Series 1035, 61 p., https://doi.org/10.3133/ds1035.

Kreisch, C. D., et al. (2017), Regularization of Mars Reconnaissance Orbiter CRISM along- track oversampled hyperspectral imaging observations of Mars, *Icarus*, *282*, 136-151.

Lacis, A. A., and Oinas, V. (1991), A description of the correlated k distribution method for modeling nongray gaseous absorption, thermal emission, and multiple scattering in vertically inhomogeneous atmospheres, *J. Geophys. Res: Atmospheres*, *96*, 9027-9063.

Langevin, Y., Poulet, F., Bibring, J. P., and Gondet, B. (2005), Sulfates in the north polar region of Mars detected by OMEGA/Mars Express, *Science*, *307*, 1584-1586.

Liu, Y., Arvidson, R. E., Wolff, M. J., Mellon, M. T., Catalano, J. G., Wang, A., and Bishop, J. L. (2012), Lambert albedo retrieval and analyses over Aram Chaos from OMEGA hyperspectral imaging data, *J. Geophys. Res: Planets*, *117*, E11.

Malin, M. C., et al. (2008), Climate, weather, and north polar observations from the Mars Reconnaissance Orbiter Mars Color Imager, *Icarus*, *194*, 501-512.

Mao, K., et al. (2008), A neural network technique for separating land surface emissivity and temperature from ASTER imagery, *IEEE Transactions on Geoscience and Remote Sensing*, *46*, 200-208.

McGuire, P. C., et al. (2009), An improvement to the volcano-scan algorithm for atmospheric correction of CRISM and OMEGA spectral data, *Planetary and Space Science*, *57*, 809-815.

Milliken, RE. (2006), Estimating the Water Content of Geologic Materials Using Near-Infrared Reflectance Spectroscopy: Applications to Laboratory and Spacecraft Data (Doctoral dissertation).

Milliken, R.E. et al. (2007), Hydration state of the Martian surface as seen by Mars Express OMEGA: 2. H2O content of the surface, *J. Geophys. Res: Planets*, *112*, E08S07, doi: 10.1029/2006JE002853.

Milliken, R. E., Grotzinger, J. P., and Thomson, B. J. (2010), Paleoclimate of Mars as captured by the stratigraphic record in Gale Crater, *Geophysical Research Letters*, *37*, L04201, doi:10.1029/2009GL041870.

Murchie, S., et al. (2007), Compact reconnaissance imaging spectrometer for Mars (CRISM) on Mars reconnaissance orbiter (MRO), *J. Geophys. Res: Planets*, *112*, E05S03, doi:10.1029/2006JE002682.

Murchie, S. L., et al. (2009), A synthesis of Martian aqueous mineralogy after 1 Mars year of observations from the Mars Reconnaissance Orbiter, *J. Geophys. Res: Planets*, *114*, E00D06, doi:10.1029/2009JE003342.

Nair, A. M., and G. Mathew (2014), Effect of bulk chemistry in the spectral variability of igneous rocks in VIS-NIR region: Implications to remote compositional mapping*, Int. J. Appl. Earth Obs.*, *30*, 227-237, doi: 10.1016/J.Jag.2014.02.004.

Peretyazhko, T. S., Sutter, B., Morris, R. V., Agresti, D. G., Le, L., and Ming, D. W. (2015), Smectite Formation from Basaltic Glass Under Acidic Conditions on Mars. 46th Lunar and Planetary Science Conference, held March 16-20, 2015 in The Woodlands, Texas. #2404

Pimentel, G. C., Forney, P. B., and Herr, K. C. (1974), Evidence about hydrate and solid water in the Martian surface from the 1969 Mariner infrared spectrometer, *Journal of Geophysical Research*, *79*, 1623-1634.

Pommerol, A., and Schmitt, B. (2008), Strength of the H2O near- infrared absorption bands in hydrated minerals: Effects of particle size and correlation with albedo, *J. Geophys. Res: Planets*, *113*, E10.

Pommerol, A., Schmitt, B., Beck, P., and Brissaud, O. (2009), Water sorption on martian regolith analogs: Thermodynamics and near-infrared reflectance spectroscopy, *Icarus*, *204*, 114-136.

Poulet, F., et al. (2005), Phyllosilicates on Mars and implications for early Martian climate, *Nature*, *438*, 623.

Sebastián, E., et al. (2010), The rover environmental monitoring station ground temperature sensor: A pyrometer for measuring ground temperature on Mars, *Sensors*, *10*, 9211-9231.

Silvestro, S., (2013), Pervasive aeolian activity along rover Curiosity's traverse in Gale Crater, Mars, *Geology*, *41*, 483-486.

Smith, M. D., Wolff, M. J., Clancy, R. T., and Murchie, S. L. (2009), Compact Reconnaissance Imaging Spectrometer observations of water vapor and carbon monoxide, *J. Geophys. Res: Planets*, *114*, 34.

Smith, M. D., Wolff, M. J., Clancy, R. T., Kleinboehl, A., and Murchie, S. L. (2013), Vertical distribution of dust and water ice aerosols from CRISM limb geometry observations, *J. Geophys. Res: Planets*, *118*, 321-334.

Stamnes, K., Tsay, S. C., Wiscombe, W., and Jayaweera, K. (1988), Numerically stable algorithm for discrete-ordinate-method radiative transfer in multiple scattering and emitting layered media, *Applied Optics*, *27*, 2502-2509.

Vasavada, A. R., Piqueux, S., Lewis, K. W., Lemmon, M. T., and Smith, M. D. (2017), Thermophysical properties along Curiosity's traverse in Gale crater, Mars, derived from the REMS ground temperature sensor, *Icarus*, *284*, 372-386.

Viviano- Beck, C. E., et al. (2014), Revised CRISM spectral parameters and summary products based on the currently detected mineral diversity on Mars, *J. Geophys. Res: Planets*, *119*, 1403-1431.

Wolff, M. J., et al. (2009), Wavelength dependence of dust aerosol single scattering albedo as observed by the Compact Reconnaissance Imaging Spectrometer, *J. Geophys. Res: Planets*, *114*, E00D04, doi:10.1029/2009JE003350.

Chapter 4: Spectral and Stratigraphic Mapping of Layered Sulfates in Mount Sharp

Abstract

The Mars Science Laboratory Curiosity rover is exploring Mt. Sharp, the ~5km high central mound of Gale Crater, which contains clay-bearing areas stratigraphically below layered sulfate-bearing strata. This sequence documents an environmental change in Gale Crater which may be analogous to Mars-wide environmental change. We map the sulfate-bearing section in detail using orbital remote sensing including CRISM VNIR spectroscopy, high-resolution HiRISE color imagery, and THEMIS thermophysical properties. The layers visible at the HiRISE scale are tens of meters apart and form a section >600 meters in thickness. Signatures of polyhydrated Mg-sulfates are detectable throughout, varying in strength of absorption features with slope and aeolian material cover. We also map an inverted channel within a wind-eroded valley that corresponds to a paleoenvironment that pre-dates the deposition of the layered sulfate section. Our results will be used to guide the Curiosity team in choosing traverses within the layered sulfates.

4.1 Introduction

The Mars Science Laboratory (MSL) Curiosity rover landed in Gale Crater in August 2012, with the goal of exploring its 5-km high interior mound Aeolis Mons, informally named Mt. Sharp [*Grotzinger et al.*, 2012]. The mound is formed of sedimentary deposits that were once much more extensive. Observations with the Compact Reconnaissance Imaging Spectrometer for Mars (CRISM) onboard the Mars Reconnaissance Orbiter [*Murchie et al.*, 2007] have been used to identify a stratigraphic sequence within the mound of smectite-bearing terrains overlain by sulfate-bearing terrains [*Milliken et al.*, 2010]. This stratigraphic sequence is thought to reflect changing

environments through time in Gale crater and may document regional or global climatic transitions on Mars.

In this chapter we summarize the mineralogy and geologic setting of the layered sulfate section using CRISM VNIR hyperspectral images, HiRISE high-resolution images [*McEwen et al.*, 2007] and derived topography, and THEMIS thermophysical data [*Christensen et al.*, 2004]. We use CRISM observations from 0.4-4 μm and solve for single scattering albedos (SSA) using the Hapke function [*Hapke*, 2012], accounting for mixed reflectance and thermal emission using a neural network approach [*He et al.*, 2018]. SSA spectra are used to make quantitative assessments of the 1.9 μm and 3 μm absorption features, indicators of hydration in minerals and absorbed and adsorbed water. We use multiple CRISM scenes over the same spatial area to increase the robustness of our mineral parameter mapping with respect to noise and differing atmospheric and lighting conditions. We also use improved spatial regularization for map-projected CRISM data [*Kreisch et al.*, 2016] relative to previous studies. We discuss correlations between CRISM-derived mineralogy and topography, texture, and thermal inertia.

Mapping the sulfate minerals and their distribution, as well as the geologic context of these layered deposits, has implications for the direction of Curiosity's future traverses. Our study emphasizes the areas that Curiosity is most likely to visit during the next few years, defined by the Mount Sharp Strategic Ascent Route (Figure 4.1, yellow line). Specific sites of interest will be informed in part by the results of this study.

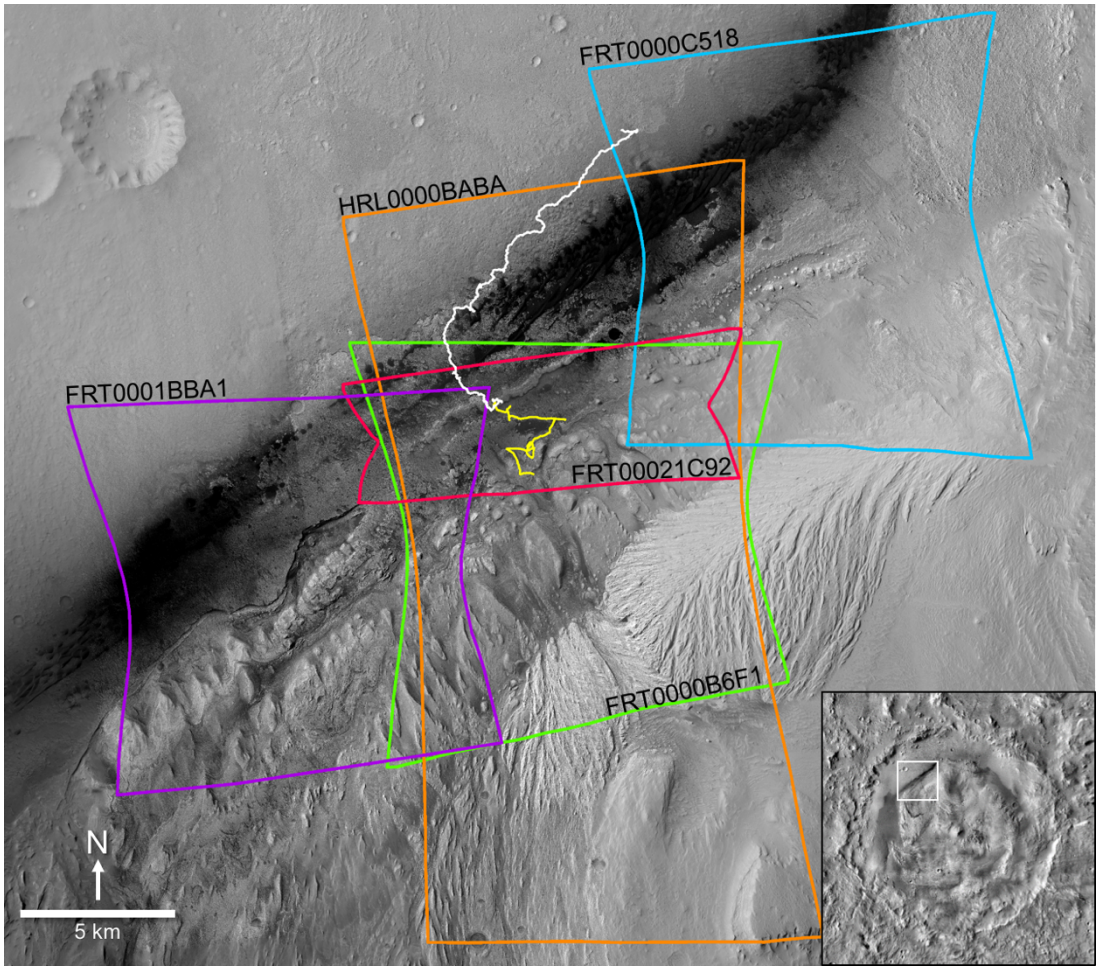

Figure 4.1: Lower Mount Sharp context map. HiRISE mosaic with footprints of CRISM scenes used in this study. Blue – FRT0000C581, green – FRT0000B6F1, orange – HRL0000BABA, purple – FRT0001BBA1, red – FRT00021C92. The MSL traverse through sol 2094 shown by the is the solid white line. The notional traverse through entering the layered sulfate section is shown by the white dashed line. Inset: THEMIS daytime IR mosaic of Gale crater with enlarged area in box.

4.2 Ancient Environments in Gale Crater

Minerals formed in aqueous environments have been discovered on Mars using orbital VNIR spectroscopy [e.g., *Bibring et al.*, 2006]. Clays, most commonly Fe/Mg smectites, are widespread in Noachian terrains and consistent with formation in aqueous environments at the surface or subsurface [*Ehlmann et al.*, 2011], but sulfates on Mars have been detected in fewer regions [*Gendrin et al.*, 2006; *Ehlmann and Edwards*, 2014]. Sulfates were initially identified with OMEGA (Observatoire pour la Minéralogie, l'Eau, les Glaces et l'Activité) onboard Mars Express

[*Bibring et al.*, 2005; *Bibring et al.*, 2006; *Gendrin et al.*, 2006], and CRISM has subsequently been used to map areas containing sulfates at higher spatial resolution. Sulfates can be detected if they are hydroxylated or hydrated. Meridiani Planum contains sulfate-rich sandstones, the Burns formation, which formed through multiple episodes of groundwater upwelling [*Grotzinger et al.*, 2005*; McLennan et al.*, 2005] and exist as a section several hundred meters thick [*Griffes et al.*, 2007; *Wiseman et al.*, 2010; *Powell et al.*, 2017]. Sulfates have also been mapped in layered terrains in Aram Chaos [*Lichtenberg et al.*, 2010] and within multiple chasma in the Valles Marineris system, [e.g., *Mangold et al.*, 2008; *Chojnacki and Hynek*, 2008; *Murchie et al.*, 2009; *Bishop et al.*, 2009]. Many of these areas are correlated with predicted areas of groundwater upwelling [*Andrews-Hanna et al.*, 2010], and the related formation of sulfate evaporites has been interpreted as evidence of changing climatic conditions after the Noachian resulting from lower water availability [*Andrews-Hanna et al.*, 2011].

In Meridiani Planum, the layered sulfate outcrops known as the Burns formation have been documented with both CRISM mineralogy and Opportunity rover chemical and mineralogical measurements. Only the top <10 m of stratigraphic section has been explored by the Opportunity rover [*Squyres et al.*, 2009] and determined to contain sulfates including Mg-, and Ca-bearing sulfates, jarosite, silicates including plagioclase, pyroxene, and olivine, and alteration products including hematite, and silica [*McLennan et al.*, 2005; *Glotch et al.*, 2006; *Morris et al.*, 2006]. CRISM has been used to identify gypsum and kieserite in exposed Burns outcrops in the walls of small craters and at Botany Bay in Endeavour Crater and integrated with Opportunity ground truth measurements of some of the same locations [*Arvidson et al.*, 2015]. Nonlinear mixing of sulfates with darker basaltic phases tends to darken CRISM spectra preferentially at shorter wavelengths, and reduce the depth of absorption features [*Arvidson et al.*, 2015]. Jarosite has not been detected

in CRISM spectra of Burns outcrops despite comprising ~10 wt% by Opportunity measurements [*Clark et al.*, 2005].

Gale Crater is located at 5.3°S, 137.7°E, on the boundary of Mars' north-south dichotomy. Crater counting indicates that Gale was formed ~3.6 billion years ago at the Noachian-Hesperian boundary [*Thomson et al.*, 2010; *Le Deit et al.*, 2013]. The bulk of Mount Sharp is located in the northern half of the crater (Figure 4.1) and its peak reaches ~5 km above crater floor. The layers that form Mount Sharp are part of a larger stratigraphic section that was deposited within the crater and later partially exhumed, likely by aeolian processes [*Anderson and Bell*, 2010; *Grotzinger et al.*, 2015; *Watkins et al.*, 2017]. The mound is embayed by units formed in the early Hesperian, giving a minimum age for the lower mound deposits themselves [*Thomson et al.*, 2010]. Crater counting by *Grant et al.* [2014] constrains the end of crater filling with mound material to ~3.3-3.2 billion years ago during the Hesperian.

Previous remote sensing work has mapped the geomorphic units on Mt. Sharp and identified hydrated minerals within by their VNIR spectral signatures. The layered sulfate section roughly corresponds to Units 6 and 7 of the map by *Malin and Edgett* [2010]. *Anderson and Bell* [2010] performed mapping of geomorphic units units throughout the Gale mound, including the layered sulfate section ("dark-toned yardangs"). *Milliken et al.* [2010] used CRISM to identify sulfate-bearing layers underlain by mixed sulfate-clay layers. They identified the sulfate species as kieserite (monohydrated) and polyhydrated Mg- sulfates, due to lack of strong Fe-sulfate or Ca-sulfate absorption features. The detections of monohydrated sulfate were located on the west side of the Gale mound. They also reported detections of hematite in some of the sulfate layers and identified several lithologic boundaries within the lower Mt. Sharp section. *Thomson et al.* [2010] traced the mineralogy from a mixed clay-sulfate layer to dominantly sulfate up-section. *Fraeman*

et al. [2013] mapped a crystalline hematite CRISM signature associated with a resistant ridge (now named Vera Rubin Ridge) at the base of Mount Sharp. *Fraeman et al.* [2016] defined a layered sulfate unit within the lower Mt. Sharp group, containing both monohydrated and polyhydrated sulfates based CRISM spectral features. However, a detailed spectroscopic and morphologic study specifically of the layered sulfate section has not been conducted.

After landing Curiosity spent the first ~300 sols of its mission exploring Yellowknife Bay, revealing evidence of previous fluvial and lacustrine environments in Gale [*Grotzinger et al.*, 2014]. Curiosity then conducted an extended traverse across the crater floor through the rocks of the Bradbury Group in order to reach a gap in the Bagnold dunes. Curiosity reached the base of Mt. Sharp at Pahrump Hills on sol 751 in September 2014. Here it encountered the basal units of Mt. Sharp, the Murray formation. It also documented resistant outcrops of likely aeolian origins that are unconformably draped over the Murray, known as the Stimson formation [*Watkins et al.*, 2016; *Banham et al.*, 2018]. *Fraeman et al.* [2016] noted that sulfate signatures also appear in the Murray, where sulfates have been detected with Curiosity, but without any noticeable morphologic correlation. Observations with the Curiosity payload indicate that the Bradbury Group and Murray formation were formed as a fluvial-deltaic-lacustrine system [*Grotzinger et al.*, 2015]. As of July 2018 Curiosity is exploring Vera Rubin Ridge, a resistant outcrop in which elevated hematite signatures have been detected with CRISM [*Fraeman et al.*, 2013; *Fraeman et al.*, 2016]. Curiosity's near-term traverse will take it northward off of Vera Rubin Ridge and into a unit that has an elevated orbital smectite signature [*Fox et al.*, 2018] that transitions into a mixed clay and sulfate signature.

4.3 Data Sets and Methods

4.3.1 Spectroscopic Mapping

CRISM is a visible and near-infrared hyperspectral imager that captures radiance from 0.36-1 μm ('S' spectrometer) and 1-3.92 μm ('L' spectrometer). CRISM acquires gimbaled targeted observations of the surface at a nominal 18 m/pixel in Full Resolution Targeted (FRT) mode and 36 m/pixel in Half Resolution Targeted (HRL) mode. Along-track oversampled (ATO) observations are acquired by commanding the gimbal to take overlapping pixels in the along-track direction. ATOs can be map-projected to 12 m/pixel or less [*Kreisch et al.*, 2016]. The details of CRISM scenes used in this work are listed in Table 1 and shown in context in Figure 4.1. FRT00021C92 is an ATO, but uses the FRT designation that was assigned to early ATOs.

Table 4.1: CRISM Observations

CRISM ID	FRT0000B6F1	HRL0000BABA	FRT0000C518	FRT0001BBA1	FRT00021C92
Earth Date	9 July 2008	20 July 2008	2 September 2008	6 November 2010	8 December 2011
Center Latitude	-4.695°	-4.813°	-4.658°	-4.994°	-4.686°
Center Longitude	137.427°	137.425°	137.537°	137.305°	137.426°
L_s	96.3°	101.3°	121.6°	176.3°	40.6°
Dust Opacity	0.53	0.53	0.56	0.75	0.75
Ice Opacity	0.11	0.11	0.10	0.10	0.08
Incidence Angle	58.9°	58.0°	58.2°	56.0°	46.2°
Detector temp.	-151°	-152°	-154°	-147°	-148°

We use the DISORT radiative transfer code [*Stamnes et al.*, 1988] to model single scattering albedo (SSA) from CRISM I/F data, the radiance on sensor divided by solar irradiance at the Martian surface and π. Surface reflection is modeled with the Hapke function with a

modestly forward-scattering two-term Henyey Greenstein phase function [*Hapke*, 2012]. Atmospheric gases may either be removed using the volcano scan algorithm [*Langevin et al.*, 2005; *Bellucci et al.*, 2007; *McGuire et al.*, 2009], or explicitly modeled using DISORT [*Arvidson et al.*, 2014]. Dust aerosol opacities are obtained from CRISM Emission Phase Function observations [*Wolff et al*., 2009]. Ice aerosol opacities are obtained from MARCI data at 320 nm [*Malin et al.*, 2008]. The CRISM scenes used in this study were converted to I/F from the radiance cubes without additional filtering, and atmospheric gases were modeled with DISORT. Emission from the surface and atmosphere is explicitly included, using surface kinetic temperatures derived by a neural network method [*He et al.*, 2018]. We correct for topographic effects using MOLA data (128 pixels per degree), so features at the ~10s of meters scale and smaller are not modeled. SSA spectra are median filtered to remove egregious spikes and then spatially regularized using a log maximum likelihood method [*Kreisch et al.*, 2016; *He et al.*, 2017].

4.3.2 Identification of Sulfates

Sulfates are identified by diagnostic absorption features in the VNIR spectral region related to structural OH and H_2O, detected by CRISM and compared to laboratory spectra of minerals. Hydrated sulfates display spectral features at 1.9 and 2.4 μm, with the latter sometimes present as a discrete absorption and otherwise as a shoulder on a slope towards longer wavelengths [*Crowley et al.*, 1991].

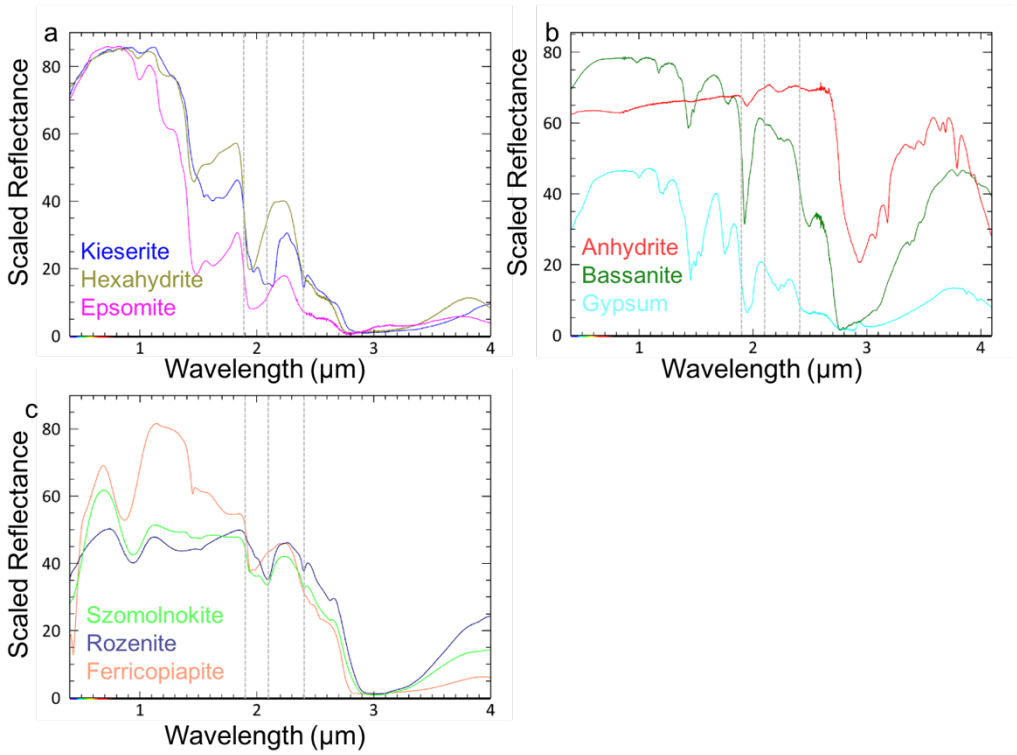

Figure 4.2: Laboratory spectra of Mg-, Fe-, and Ca-bearing hydrated and hydroxylated sulfates. a) Fe-bearing sulfates szomolnokite ($Fe^{2+}SO_4 \bullet H_2O$), rozenite ($Fe^{2+}SO_4 \bullet 4H_2O$), ferricopiapite ($Fe^{3+}_{2/3}\ Fe^{3+}_4(SO_4)_6(OH)_2 \bullet 20H_2O$) from RELAB (bkr1jb622, 623, 620). b) Ca-bearing sulfates anhydrite ($CaSO_4 \bullet H_2O$), bassanite($CaSO_4 \bullet 0.5H_2O$), and gypsum ($CaSO_4 \bullet 2H_2O$) from the USGS spectral library. c) Mg-bearing sulfates kieserite ($MgSO_4 \bullet H_2O$) (F1CC15, from the CRISM spectral library, rescaled), hexahydrite ($MgSO_4 \bullet 6H_2O$) epsomite ($MgSO_4 \bullet 7H_2O$) from the USGS spectral library. Dashed lines are at 1.9, 2.1, and 2.4 μm.

The monohydrated sulfates kieserite ($MgSO_4 \cdot H_2O$) and szmolnokite ($Fe^{2+}SO_4 \cdot H_2O$) have combination OH/H_2O or S-O bend overtones at ~2.1, 2.4 and 2.55 μm [*Cloutis et al.*, 2006]. Polyhydrated magnesium sulfates have similar absorptions but at ~1.9 and 2.4 μm (Figure 4.2a). The 1.9 μm vs. 2.1 μm feature is an important distinguisher between polyhydrated Mg sulfates and kieserite. Polyhydrated Mg sulfates are fairly featureless in the 2.1-2.3 μm range [*Crowley*, 1991]. It is therefore difficult to distinguish between polyhydrated Mg sulfate species using CRISM, as outcrops at this scale are very unlikely to be composed of pure minerals. Common polyhydrated Mg sulfates include starkeyite ($MgSO_4 \cdot 4H_2O$), hexahydrite ($MgSO_4 \cdot 6H_2O$), and epsomite ($MgSO_4 \cdot 7H_2O$) (Figure 4.2a).

Calcium-bearing sulfates have additional absorption features that distinguish them from Mg sulfates. Gypsum ($CaSO_4 \cdot 2H_2O$) and bassanite ($CaSO_4 \cdot 0.5H_2O$) have H_2O combination and overtone bands between 2.1-2.3 μm, the most prominent of which occur at ~2.22 and ~2.26 μm (Figure 4.2b) [*Bishop et al.*, 2014]. Iron-bearing sulfates can be identified using crystal field absorption bands in the 0.4-1 μm range, whereas certain species may have additional absorptions in the 2-2.5 μm range (Figure 4.2c) [*Lane et al.*, 2015].

The OH stretch fundamentals in OH-bearing sulfates such as jarosite and alunite can occur from 2.80-3.15 μm, and the H_2O stretch fundamentals in hydrated sulfates can occur from 2.85-3.1 μm [*Cloutis et al.*, 2006]. The individual absorption bands are difficult to separate. The shape and center of the 3 μm band in sulfates changes with temperature and grain size [*Jamieson et al.,* 2014; *De Angelis et al.,* 2017].

Intimate mixtures of fine-grained epsomite and various smectites have some of the spectral properties of both. With greater proportions of sulfate, the 2.4 μm absorption or shoulder becomes deeper, while retaining but shallowing the smectite metal-OH features at 2.2-2.3 μm. [*Stack and Milliken*, 2015].

Unlike laboratory samples, sulfates in geologic settings are expected to be detected in conjunction with other minerals. Spectra of intimate mixtures of minerals are a non-linear combination of the components [*Clark*, 1999]. The Burns formation provides one analogy for what may comprise the Mt. Sharp layered sulfate unit; exposed Burns outcrops contain silicate minerals and iron oxides in addition to sulfates [*McLennan et al.*, 2005; *Glotch et al.*, 2006; *Morris et al.*, 2006] and do not have CRISM spectral signatures of pure minerals [*Arvidson et al.*, 2015]. In flat areas of Meridiani Planum, outcrops are typically obscured by sand and regolith; VNIR spectra of these areas generally do not show sulfate signatures and instead are consistent with pyroxene and

iron oxides [*Arvidson et al.*, 2006]. These realities of observing from orbit must be taken into account when assessing the strength of spectral absorptions and the spatial extent of the sulfate-bearing section.

4.3.3 Spectral Indices

We map sulfate-bearing strata on Mt. Sharp using CRISM spectral indices, primarily derived from *Viviano-Beck et al.* [2014]. These include BD1900R2, which measures the band depth at 1.9 μm, and SINDEX2 (Figure 4.3), which measures a convexity at 2.3 μm due to hydrated sulfate absorptions at shorter and longer wavelengths (Figure 4.3). We searched for but did not find evidence for 2.1 μm absorptions indicating monohydrated sulfates. We also calculate an Integrated Band Area of the broad 3 μm feature [*Pommerol and Schmitt*, 2008]. The color composite overlay shown in Figure 4.4 and details in later figures are three-color composites of CRISM FRT0000B6F1 with R = SINDEX2, G = IBA(3 μm), and B = BD1900R2. In this color scheme, sulfate-rich areas have a strong red component and appear red, pink, or orange, varying with the strength of the 3 μm and 1.9 μm features. Pink indicates strong values of both SINDEX2 and BD19000R2. Orange indicates strong SINDEX2 and 3 μm IBA. Smectite-rich areas, which have a 2.3 μm absorption instead of a maximum, lack the SINDEX2 signature and appear blue or cyan. Green areas, corresponding to high values of the 3 μm feature only, mainly appear on the south and east sides of mounds, where they correspond to areas in facing away from the sun and/or in shadow. These are artifacts resulting from the non-modeling of fine-scale topography in DISORT.

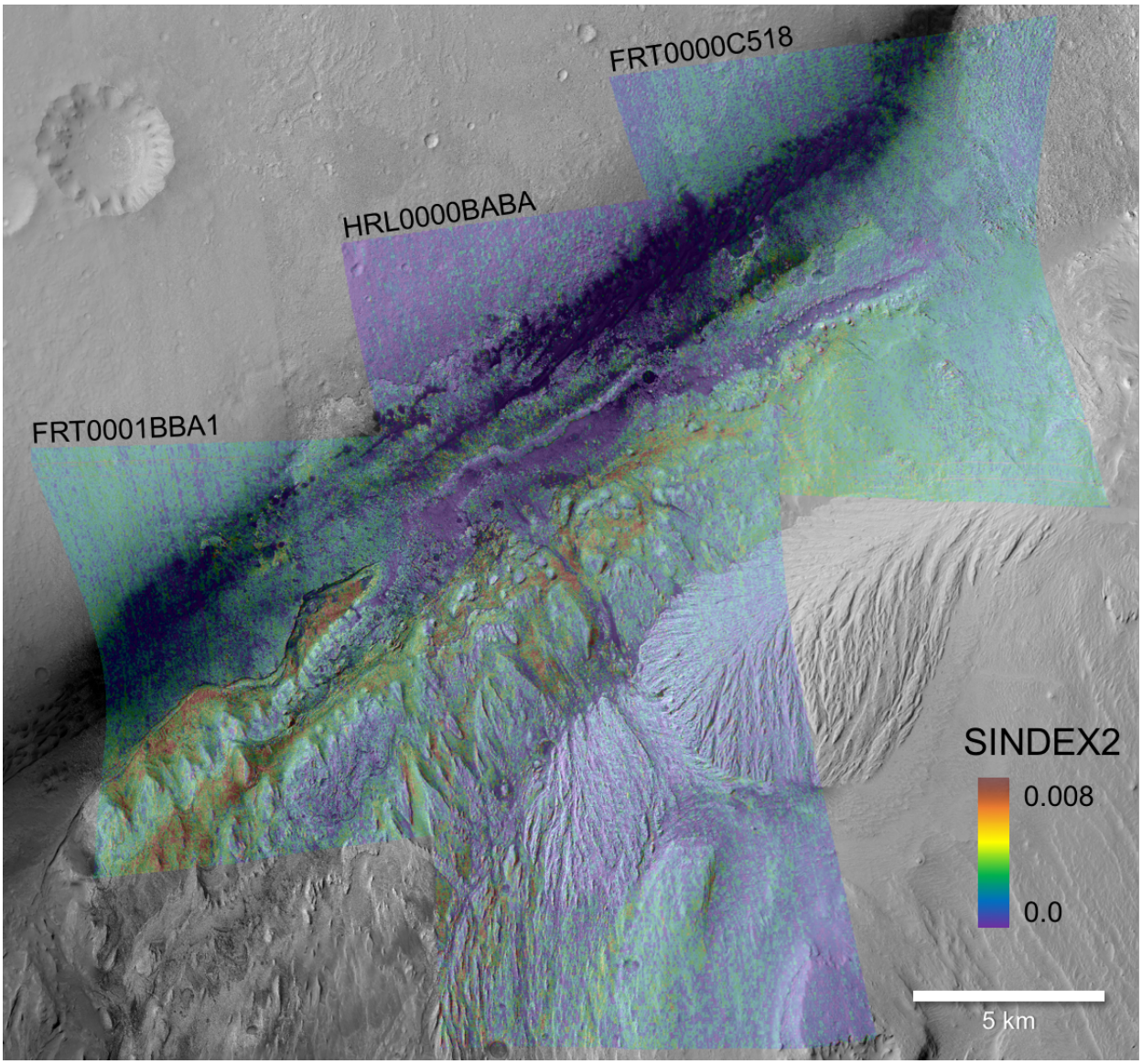

Figure 4.3: SINDEX2 parameter maps derived from HRL0000BABA and FRT0001BBA1, overlaid on HiRISE mosaic of lower Mt. Sharp. SINDEX2 measures the convexity at 2.3 μm found in hydrated sulfates due to absorptions at 2.4 μm and either 1.9 or 2.1 μm .

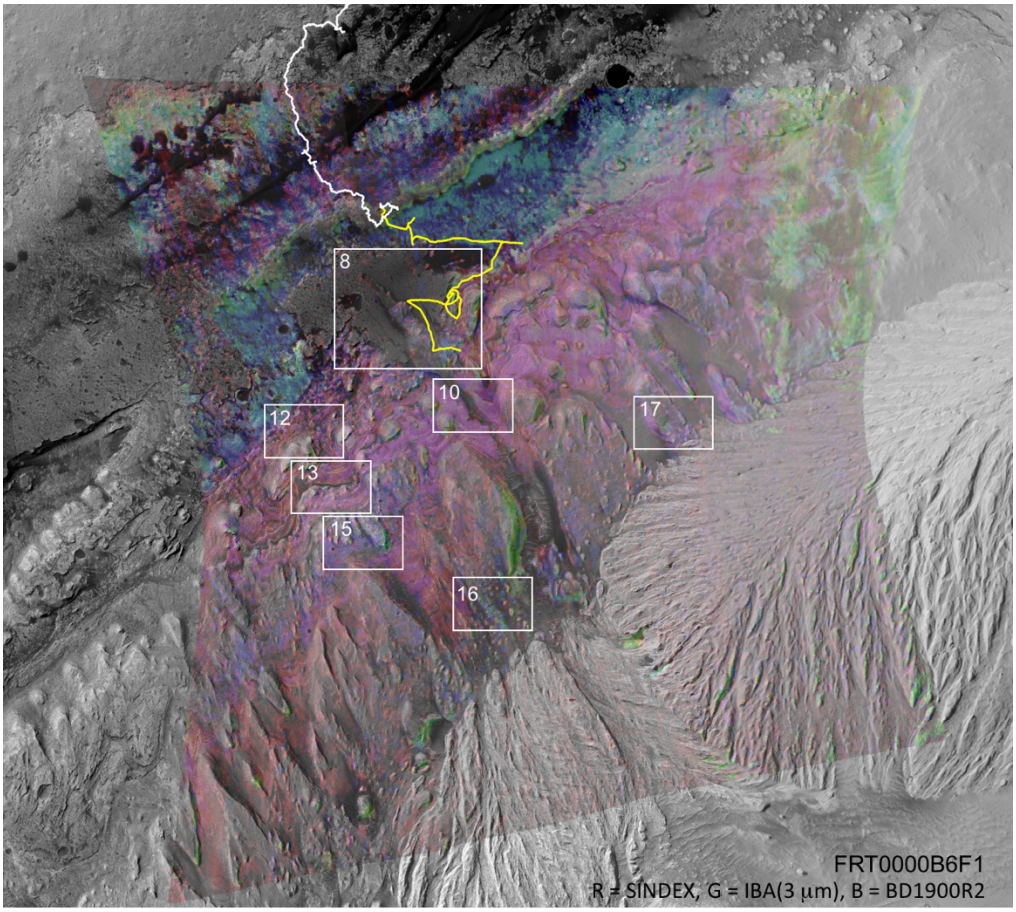

Figure 4.4: Color composite of CRISM parameters derived from FRT0000B6F1 overlaid on HiRISE mosaic of lower Mt. Sharp. Red: SINDEX2, Green: 3 μm IBA, Blue: BD1900R2. White boxes indicate detailed areas of the sulfate section shown in subsequent figures.

4.3.4 Morphologic Mapping

The detailed morphology of the layered sulfate section was investigated using HiRISE [*McEwen et al.,* 2007] image mosaics. HiRISE was used in both red band (694 nm) [*Calef and Parker*, 2016] and false color (near IR, red, blue/green, centered at 874, 694, and 536 nm) [Christopher Edwards, personal communication] for fine-scale analysis of sulfate-bearing outcrops at at 25 cm/pixel. HiRISE stereo data has also been used to create a DEM [*Parker and Calef*, 2016], which was used for topographic measurements (Figure 4.5). The DEM mosaic has a resolution of 1 m/pixel. The HiRISE red mosaic and DEM were used to make strike and dip

measurements of layers by a least-squares fit to a plane using MATLAB. The dip values reported in this chapter are those of the fit plane.

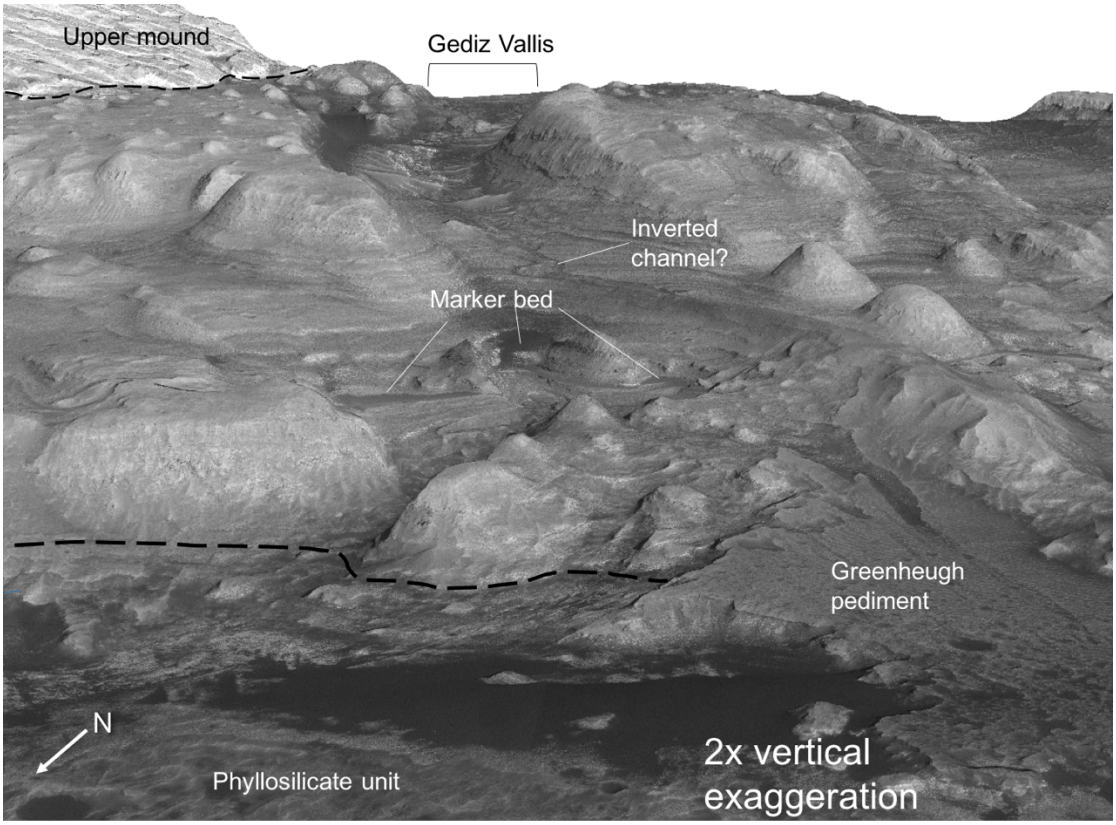

Figure 4.5: Perspective view of Mount Sharp from HiRISE mosaic and DEM, 2x vertically exaggerated. Extent of the layered sulfate unit is given by the black dashed lines. Gediz Vallis cuts through the center of the scene and terminates at the Greenheugh pediment. Large mesas dominate the top portion of the section and smaller rounded buttes and mounds appear lower. The phyllosilicate unit is in the lower left corner of the image and the duststone upper mound is in the upper left. The upper mound continues beyond Gediz Vallis but this area is not part of the image mosaic.

4.3.5 Thermophysical Parameters

THEMIS data [*Christensen et al.*, 2004] were used in the form of a mosaic of thermal inertia values (Figure 4.6) [Christopher Edwards, personal communication]. Thermal inertia is a measure of the ability of the materials in the upper few centimeters of a surface to resist changes in temperature. It is defined as $TI = (k\rho c)^{1/2}$, where k is the thermal conductivity, ρ is the density, and c is the specific heat. The factor that varies the most is thermal conductivity, so thermal inertia can be related to grain size and porosity [*Christensen et al.*, 2003; *Fergason et al.*, 2006].

Unconsolidated particles with small sizes, such as dust and sand, have the lowest thermal inertias, whereas igneous bedrock has very high thermal inertia. Intermediate thermal inertias may correspond to a variety of materials, including mixtures of particles with different sizes, duricrusts, and sedimentary rocks. THEMIS observations have a resolution of ~100 m/pixel, as does the thermal inertia mosaic.

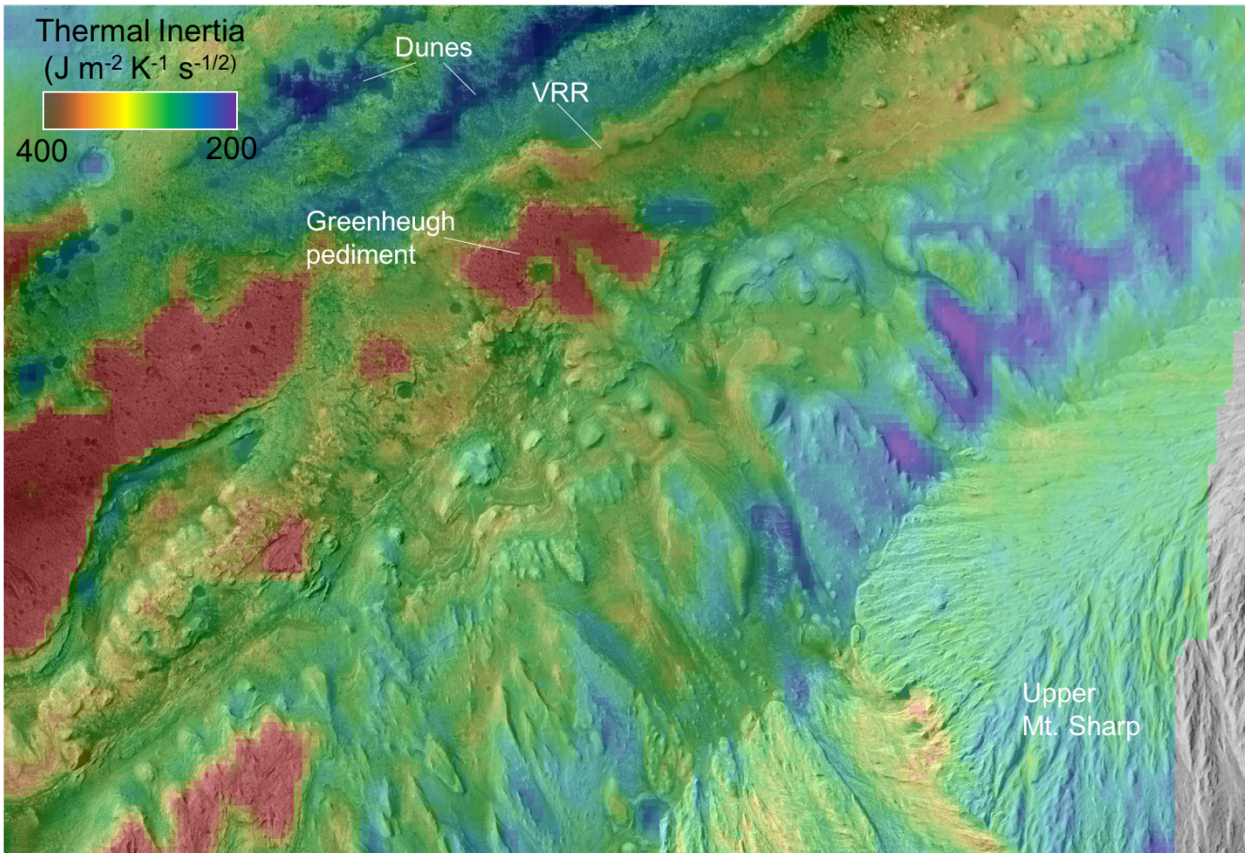

Figure 4.6: THEMIS-derived thermal inertia mosaic overlaid on HiRISE red mosaic. The Greenheugh pediment and potentially related draping strata have some of the highest TI values in the area. The lowest areas correspond to aeolian materials, such as the Bagnold dunes. VRR = Vera Rubin Ridge.

4.4. Orbital Mapping of the Layered Sulfate Unit

4.4.1 Overall properties

We define the upper and lower boundaries of the sulfate-bearing section using CRISM spectral indices, examination of individual spectra, morphologic boundaries in HiRISE, and changes in slope in the HiRISE DEM. The extent of sulfate-rich areas as mapped by SINDEX2 is shown in Figure 4.3. The base of the sulfate-bearing section varies from -4075 to -4030 meters in elevation relative to the MOLA areoid. The contact with the clay and clay/sulfate bearing units is defined by a change in morphologic expression and mineral parameters and a transition to an overall lower slope below.

"Upper Mount Sharp" strata are defined to be the anhydrous layers that stratigraphically lie above the sulfate-bearing unit (Figure 4.5), and are interpreted as duststones [*Milliken et al.*, 2010]. The transition from layered sulfate to the upper mound is marked by a change in spectral shape, albedo, morphologic texture, and topographic slope. Spectra of the upper mound are bright and relatively anhydrous, with a weak 3 μm feature relative to lower units. The slope of the upper mound is steeper than the layered sulfates and the yardangs that cover it have different orientations than the ridges and buttes below. Much of the contact between the layered sulfate unit and the upper mound is obscured by aeolian deposits and regolith cover. The contact with the duststones above varies from -3150 towards the southwest and to -3470 to the northeast. Therefore, the difference in topography in the entire exposed section is 600-800 meters and the overall slope of the sulfate-bearing material is 8-10°.

We divide the layered sulfate section into subunits on the basis of the nature and strength of spectral indices, detailed examination of spectra, and textural and morphological data from HiRISE images and DEMs (Figure 4.7). We observe a CRISM spectral signature indicative of polyhydrated sulfate throughout the section, with variations in its strength correlated to surface

expression and regolith cover. Like similar observations made of the Burns formation, these signatures indicate silicate minerals make up a significant portion of the rock. The spectral, textural, and morphologic qualities of these areas are outlined below. The layered sulfate is divided into upper and lower sections separated by a distinctive marker bed [*Milliken et al.*, 2010] as well as a unit with many small round knobs near the unconformity with Upper Mt. Sharp. Several features that are not strictly part of the layered sulfate section are also outlined for their relevancy to later discussions. These include the Greenheugh pediment and the Gediz Vallis ridge.

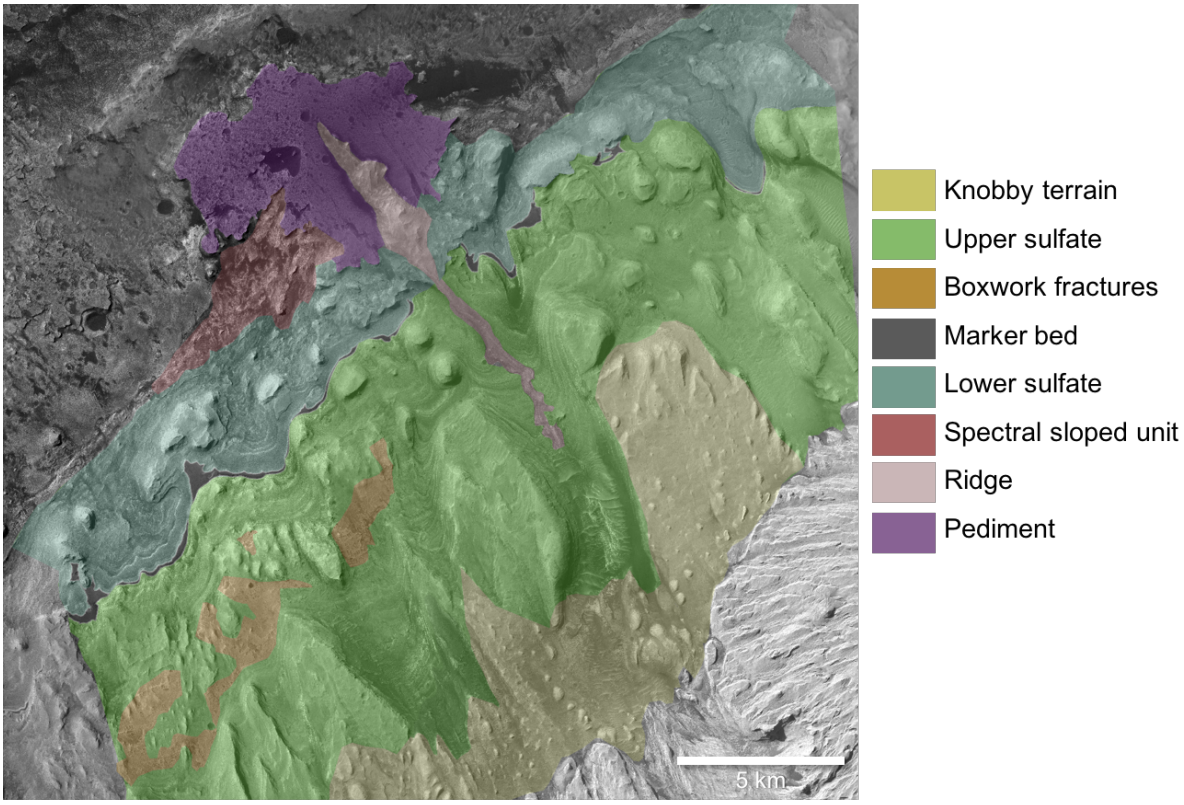

Figure 4.7: Map of layered sulfate subunits and adjacent units discussed in the text.

4.4.2 Subunits

Greenheugh pediment

The fan-shaped deposit known as Greenheugh pediment (Figure 4.8) is a resistant, low albedo surface that unconformably overlies lower Mt. Sharp units [*Fraeman et al.,* 2016] including the phyllosilicate unit and layered sulfates. Its surface slopes upward at ~9°. At fine scales the

surface has a pitted and ridged texture. Brighter bedrock appears along its margins and the edges of depressions on its surface. The relative elevations indicate that the pediment itself is only a few meters thick. CRISM spectra of the pediment have a red slope from 1.7 – 2.5 μm (Figure 4.9). These areas are spectrally distinct from the sands collected in depressions on the pediment, which have broad ~1 μm and 2 μm absorption features indicative of olivine and pyroxene content. The pediment does not show any evidence for hydrated minerals (Figure 4.9). This surface has higher thermal inertia (400-430 J m^{-2} K^{-1} $s^{-1/2}$) than its surroundings (320-350 J m^{-2} K^{-1} $s^{-1/2}$), suggesting a more competent unit.

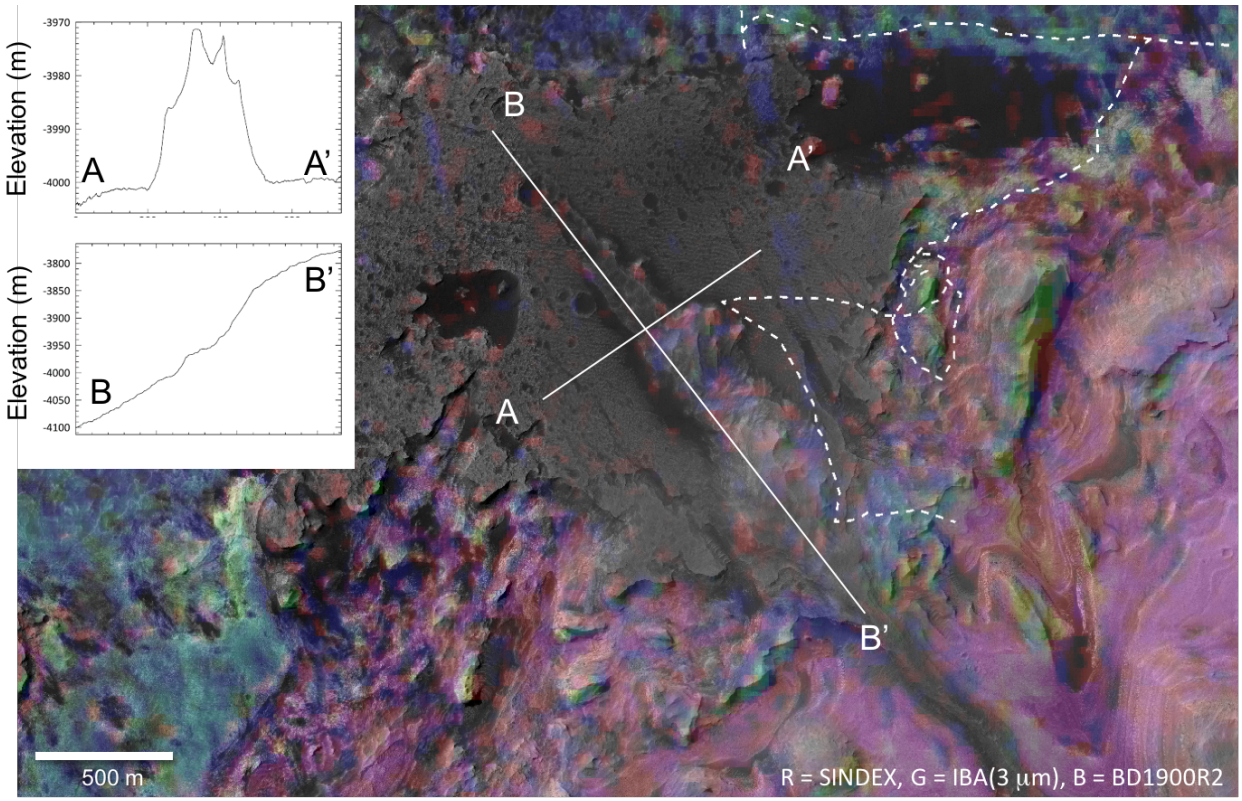

Figure 4.8: Detail of the Greenheugh pediment and the Gediz Vallis ridge. The surface of the pediment is almost totally devoid of hydrated mineral detections. The ridge overlying it contains scattered detections of hydrated sulfate. The notional traverse through entering the layered sulfate section is shown by the white dashed line. Inset: topographic profiles derived from HiRISE DEM.

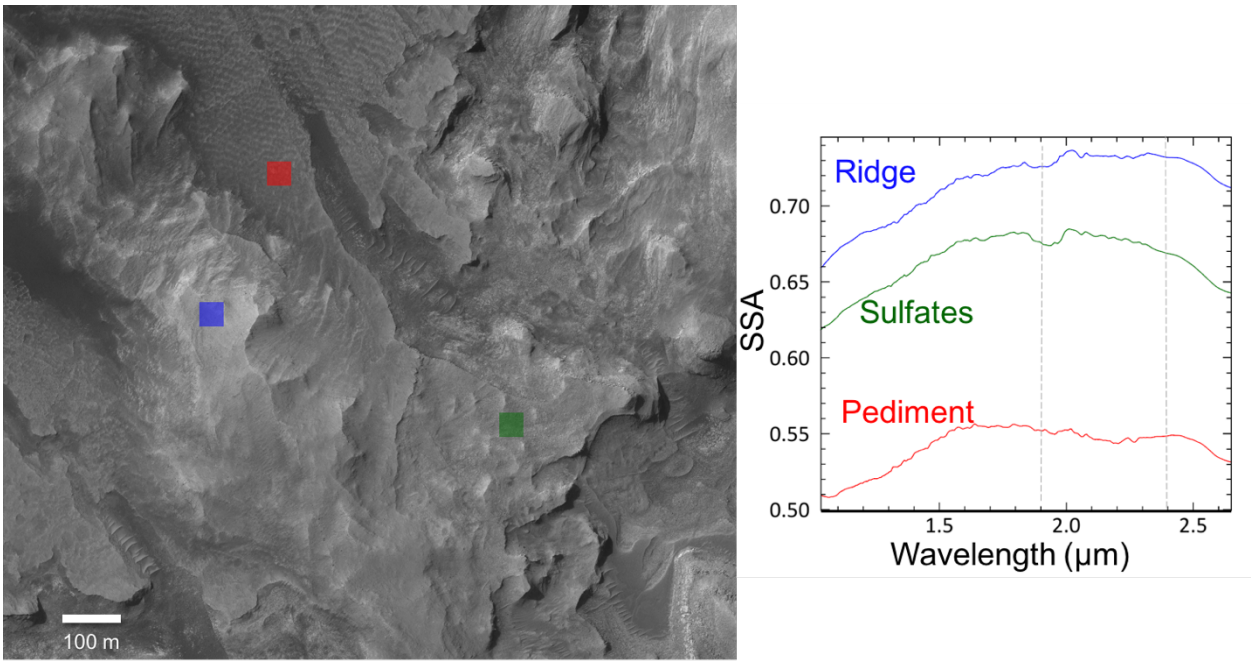

Figure 4.9: Left: Gediz Vallis ridge and the Greenheugh pediment with locations of spectra. Right: CRISM spectra from the ridge and surrounding area. Dashed lines are at 1.9 and 2.4 μm. Red: pediment surface, dark, dehydrated, and mafic-mineral-bearing. Green: sulfate terrain adjacent to the ridge. Blue: high elevation of ridge, showing hydration but not a clear 2.4 μm absorption related to hydrated sulfate.

Gediz Vallis and Gediz Vallis ridge

Gediz Vallis is a U-shaped valley running SE-NW that originates in the Upper Mount Sharp duststones and terminates at the Greenheugh pediment (Figure 4.10). The vallis walls exhibit regular layering in HiRISE and have strong spectral signatures of polyhydrated sulfate (Figure 4.11). The upper portion of Gediz Vallis contains a wind-blown dark sand deposit that is concentrated on its eastern side and obscures any layering. The CRISM parameters HCPINDEX (broad ~2 μm absorption) and BD860_2 (860 nm band depth) indicate that these sands contain high-Ca pyroxene and hematite.

A raised sinuous ridge, the Gediz Vallis ridge, cuts through the center of Gediz Vallis (Figure 4.10). It is elevated above the floor of the vallis (Figure 4.10) and appears to be an inverted channel. The ridge's upper extreme is obscured by aeolian materials, and it first emerges at a height of only a few meters. As it meanders downslope, it gains in elevation relative to the vallis floor.

Where it meets the Greenheugh pediment, it is up to 70 meters high. The ridge is bounded in some areas by a narrow trough (<30 meters wide) filled with wind-blown sand (Figure 4.11). Unlike the surrounding layered sulfate walls, the ridge lacks a significant sulfate signature (Figure 4.11). Instead the ridge spectra are relatively flat from 1.6 – 2.4 μm, after which they dip redward. The ridge lacks a strong 2 μm pyroxene absorption (Figure 4.11). At CRISM's 12 m/pixel resolution we cannot distinguish between the sand-filled trough and the raised ridge.

The Gediz Vallis ridge runs down the center of the pediment, perpendicular to the outward face of Mt. Sharp, and grows wider, to ~560 meters at its maximum. The ridge stands up to 65 meters above the pediment on either side (Figure 4.8), before sloping downward into the pediment surface. Its texture is rugged and massive. There is some evidence for layering in the sides of the ridge, but we do not observe anything similar to the banding common to the layered sulfates. The ridge adjacent to the pediment shows a weak and patchy sulfate signature (Figure 4.9). The ridge has lower thermal inertia than the pediment (290-340 J m^{-2} K^{-1} $s^{-1/2}$), more consistent with the overlying sulfate-bearing units.

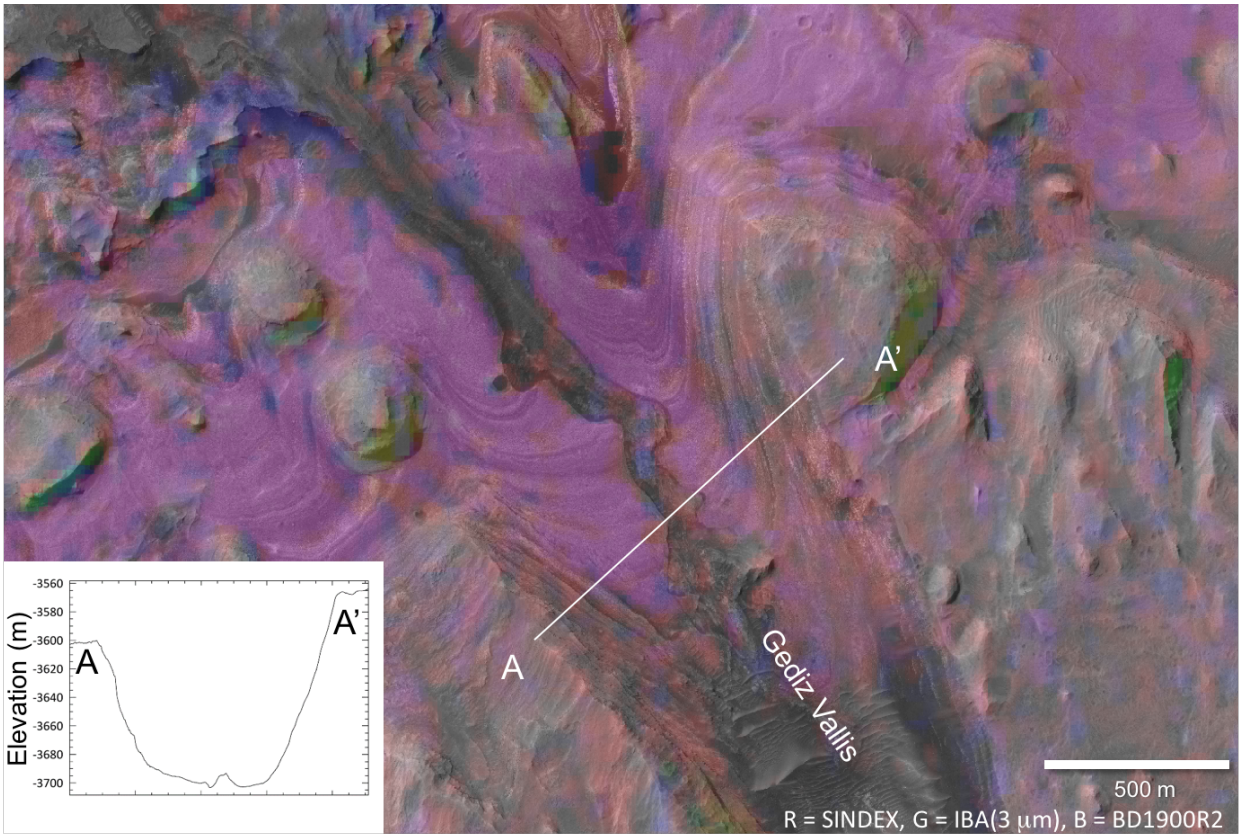

Figure 4.10: Detail of Gediz Vallis and the inverted channel or ridge. The raised channel surface at the center of the vallis lacks a sulfate signature. in sharp contrast to the contiguous sulfate-bearing layers on either side. Inset: topographic profile from HiRISE DEM.

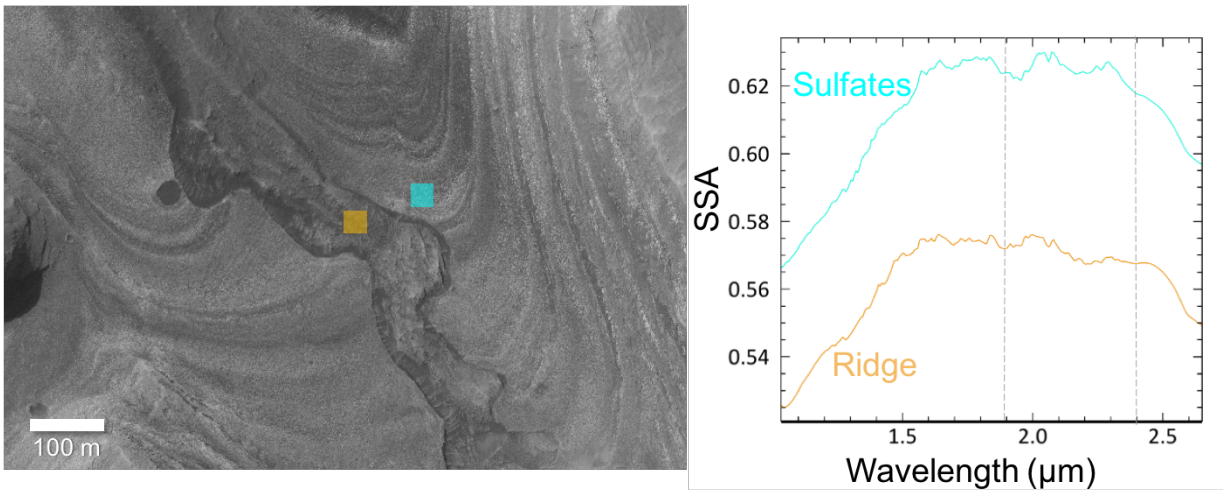

Figure 4.11: Left: The middle portion of the Gediz Vallis ridge with locations of spectra. Right: CRISM spectra of the channel and adjacent layered sulfate. Dashed lines are at 1.9 and 2.4 μm.

Lower sulfate unit

On the northeast side of the Greenheugh pediment, the layered sulfate unit and phyllosilicate unit are separated by an area with more ambiguous spectral signatures, interpreted to be a mixture of sulfate and clay species [*Fox et al.*, 2018]. Adjacent to the pediment, much of this transition area is obscured by aeolian sand cover (Figure 4.8). On the southwestern side of the Greenheugh pediment, the the lowest part of the layered sulfate section begins above a narrow trough containing bright material, which onlaps the pediment and has the spectral signature is strongly red sloped from 1.3-1.6 μm, possibly caused by an enhanced iron-bearing component such as olivine, iron-bearing sulfates, or ferrous smectites [*Fraeman et al.*, 2016]. The lowest portion of the layered sulfate unit on this side is bounded by a cliff 10-20 m high that separates it from the spectrally slope material.

The lower portion of the layered sulfate section consists of exposed continuous layering for many hundreds of meters horizontally, particularly to the south and west of Greenheugh pediment (Figure 4.12). The layers appear as dark and light bands in the sides of cliffs, buttes, and mesas, with some layers forming gently sloping shelves or benches. The layers resolvable in HiRISE are only a few meters in thickness, although finer-scale layering may also be present. The lower sulfate contains dozens of subrounded mounds that rise tens of meters above the other strata with plateaus or U-shaped valleys between them. The sides of the mounds frequently show layering in HiRISE (Figure 4.5). The tops of the mounds do not show layering visible in the sides of the mounds, and may be a capping unit. The strongest hydrated sulfate spectral signatures are associated with the valleys or plateaus between the mounds.

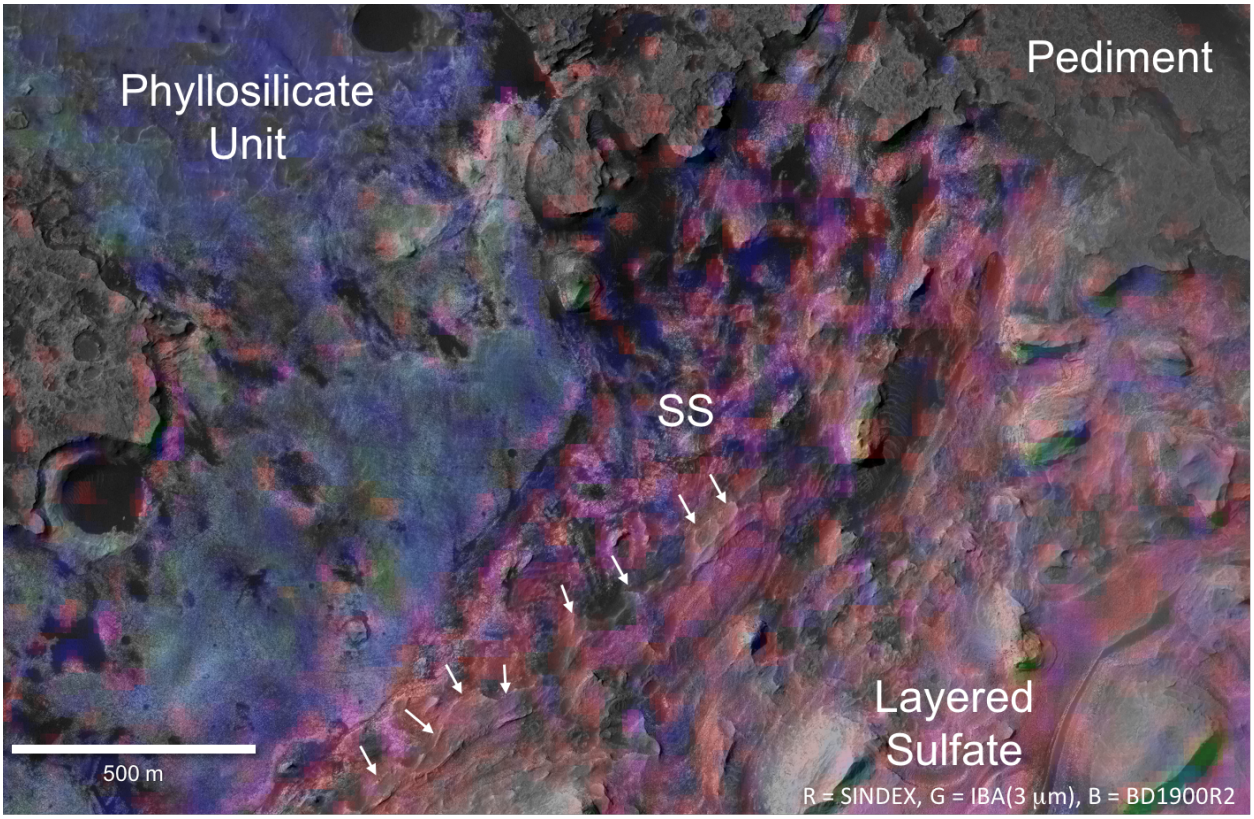

Figure 4.12: Detail of lower fractured unit and contact with spectrally-sloped material below. Arrows mark the edge of a cliff at the bottom of the layered sulfate unit. SS = spectral sloped unit.

Marker bed

Milliken et al. [2010] mapped a dark, smooth marker bed as the boundary between two sections of the mound (Figure 4.12). Unlike typical banded sulfate areas, the marker bed forms a wide, relatively flat terrace. It forms cliffs at its lower margin and preserves craters. Small ripples are visible on its surface, and debris has accumulated near the uphill boundary with the layers above (Figure 4.13). The marker bed is exposed at variable lateral extent for up to 3 km southwest and northeast of the Greenheugh pediment. The marker bed disappears completely below Gediz Vallis and reappears on the opposite side. Overall the marker bed appears at an elevation between

-3780 and -3830. The surface is very shallowly sloped (Figure 4.13), with dips of generally <4° and a dip direction towards the northwest.

The width of the marker bed's surface expression in this region is a maximum of 240 m (Figure 4.13), but more typically <50 m, making it resolvable with CRISM in some but not all areas where it is identifiable in HiRISE images. Its spectral signature possesses a broad absorption > 2 μm indicative of high-Ca pyroxene, consistent with a primarily basaltic composition for the marker bed (Figure 4.14). Select areas have faint sulfate signatures overprinted on the high-Ca pyroxene.

Spectra of the layers directly below the marker bed are variable in shape. Some show clear 2.4 μm absorptions but have weak or absent 1.9 μm absorptions. Some show broad 2 μm absorptions indicative of pyroxene enrichment. These layers have lower albedo than those above the marker bed. The patchy pyroxene signature may result from enrichment in the bedrock itself, or more likely, debris carried downhill from the marker bed.

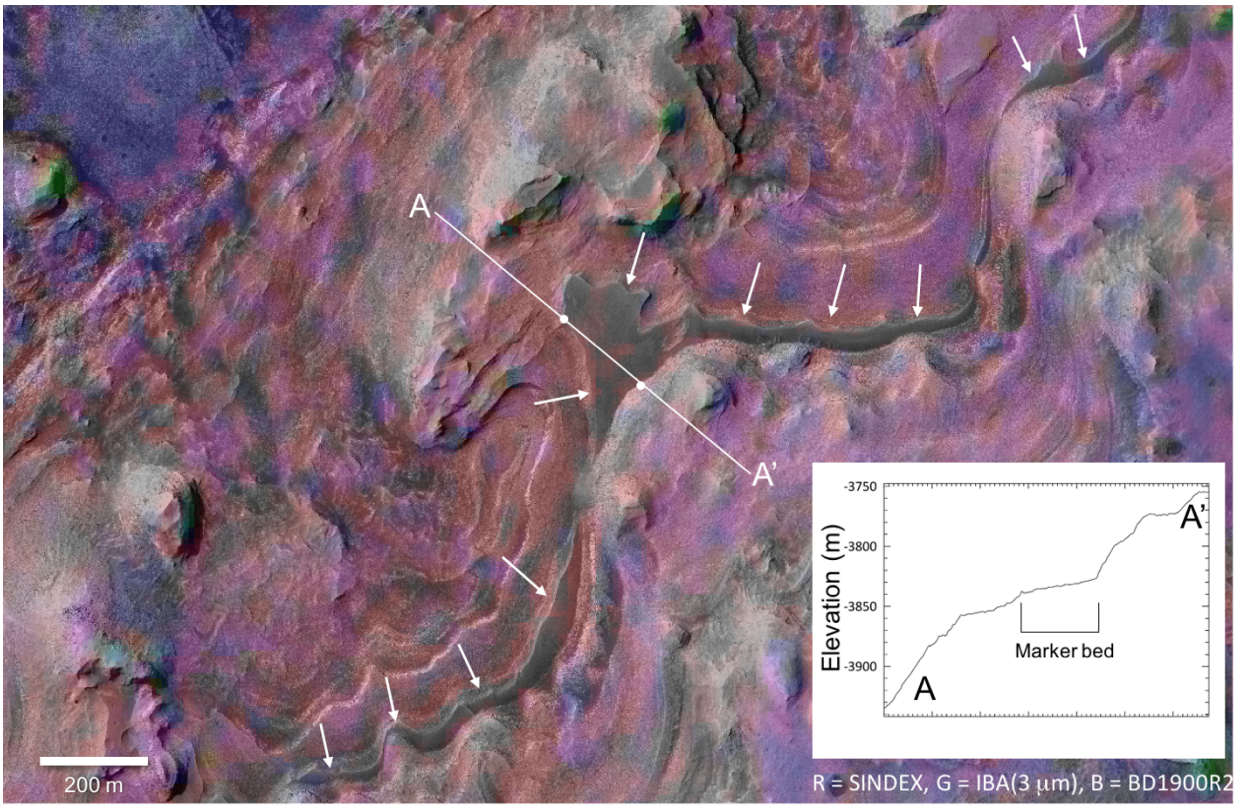

Figure 4.13: Detail of the marker bed and strata above and below. Arrows show the lower edge of the marker bed. Inset: topographic profile from HiRISE DEM.

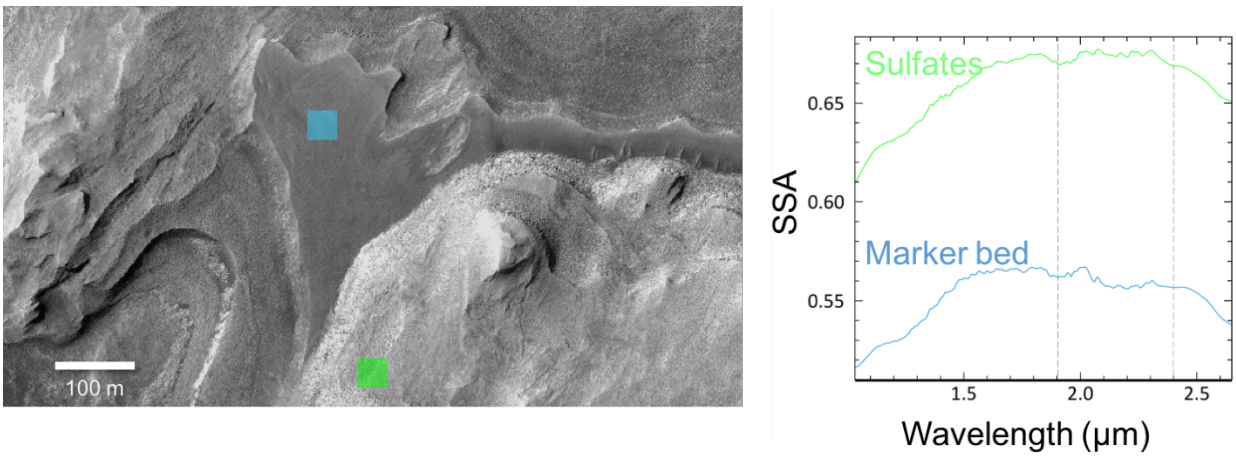

Figure 4.14: Left: The widest portion of the marker bed with spectral locations shown. Right: CRISM spectra of the marker bed and layers above. Dashed lines are at 1.9 and 2.4 μm. The marker bed contains HCP whereas the strata above and below contain polyhydrated sulfate.

Upper sulfate unit

Above the marker bed, the surface expression of the layered sulfates is generally similar to the section immediately below it. Rounded mounds are separated by U-shaped valleys, and both have horizontal banding that can be traced for hundreds of meters. However, this part of the layered sulfates contains evidence for diagenesis, and the erosional state varies from that below.

Approximately 150 meters above the marker bed is a region of more shallowly sloped strata. This layer is the only one to contain boxwork fractures [*Anderson and Bell*, 2010; *Siebach et al.*, 2014] (Figure 4.15). Boxwork ridges at the tens-of-meters scale have been previously mapped by *Siebach et al.* [2014]. They suggest the following sequence of events to form these features: fracturing in the existing rock, infill and cementation, and erosion of the surrounding rock to expose the cemented areas above the rest. This modification requires fluid circulation in these areas after the formation of layers.

The layers with boxwork fractures are associated with a higher BD1900R2 parameter and lower BD3000 and SINDEX2 parameters than the layers above and below (Figure 4.14). The boxwork fracture areas have consistently high values of 1.9 μm band depth, and relatively lower values of SINDEX2. The weaker sulfate signature that consistently appears in the boxwork fracture areas (mapped independently with HiRISE), does not suggest that sulfate is the major cementing agent. It is difficult to tell if other hydrated secondary minerals are present in the boxwork region or the sulfates are simply poorly exposed.

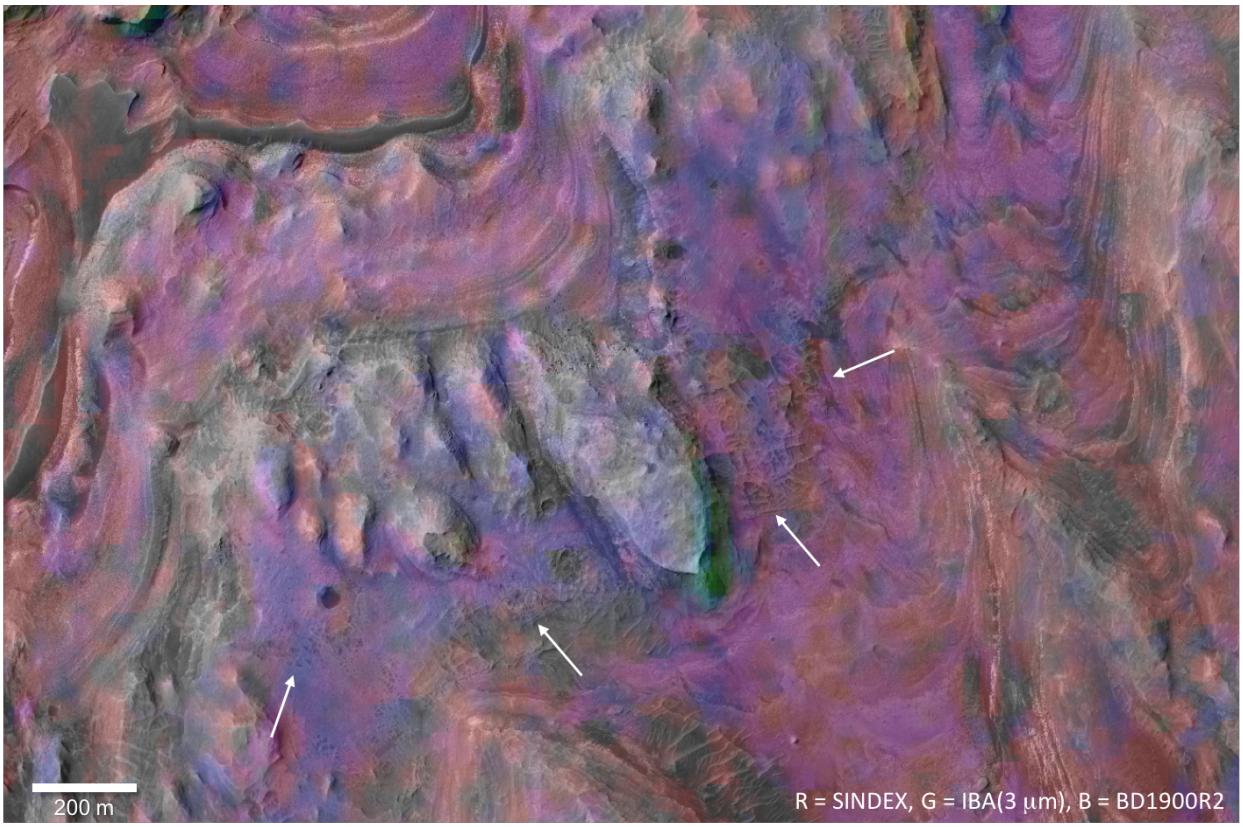

Figure 4.15: Detail of boxwork fracture zone. Arrows indicate some of the boxwork structures. These areas are correlated with a stronger BD1900R2 and weaker SINDEX2 signature than surrounding areas.

The upper sulfate section is dominated by massive elongated ridges pointing NW-SE and downhill out of Mt. Sharp. They are separated by U-shaped valleys. On the southwest side of the study area between layered cliff faces are some of the highest values of SINDEX2 (Figure 4.16). In contrast, on the northeast side the sulfate signatures disappear almost completely. Inspection of HiRISE images indicates that these areas are covered with wind-blown material that forms ripples (Figures 4.17-18). These areas have correspondingly low thermal inertias (190-240 200 J m^{-2} K^{-1} $s^{-1/2}$), but do not have enhanced mafic mineral parameters. It is likely that CRISM and THEMIS in these areas are sampling the overlying aeolian material rather than the bedrock.

A darker, more pyroxene-rich layer with a different texture appears at the top of the layered sulfate section (Figure 4.16) which may represent a change in the expression of the sulfate layers,

or sand fill at a scale too small to be definitively assessed with HiRISE. There is no obvious change in thermal inertia, however, compared to the brighter sulfate-bearing layers below.

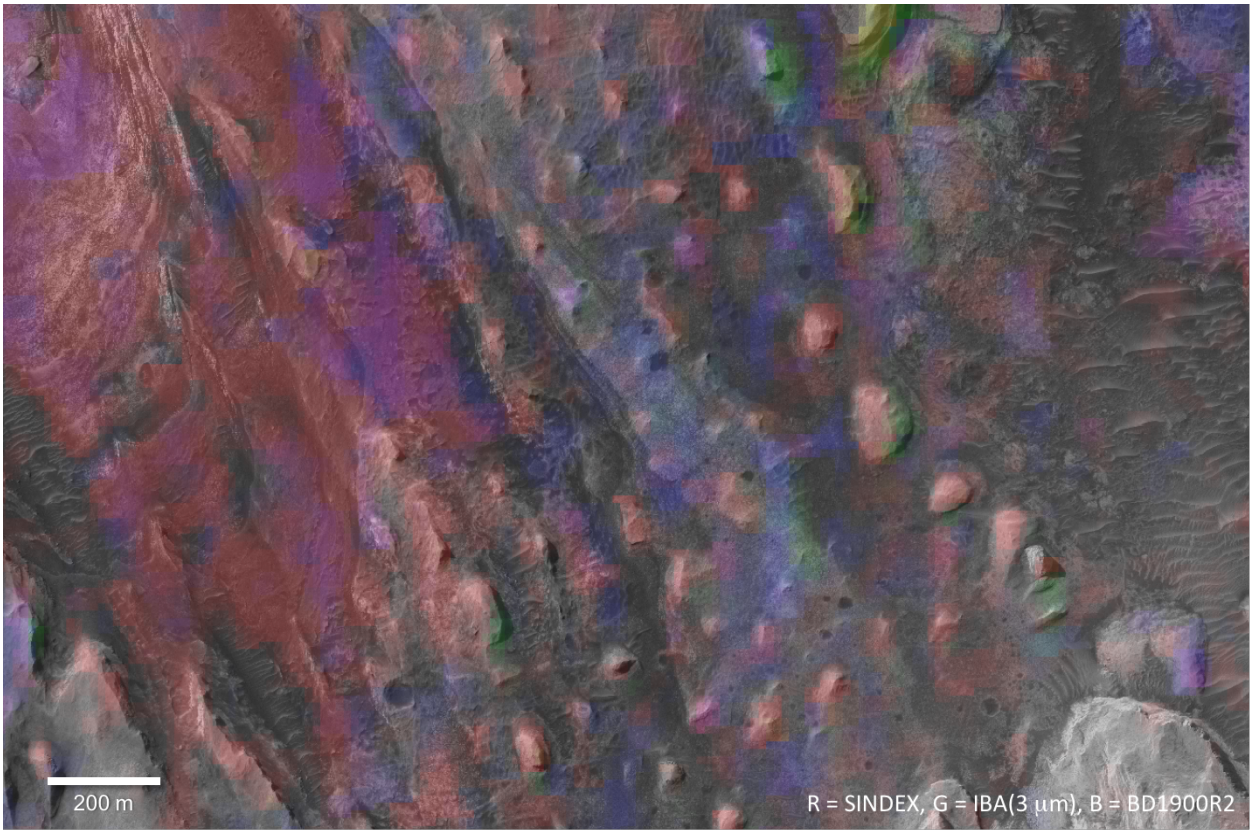

Figure 4.16: Detail of upper sulfate section with strong SINDEX2 signatures and small mounds.

Knobby unit

To the north and east of Gediz Vallis, the largest of the rounded mounds and a series of pointed mesas meet a smoothly sloping surface ~1400 m wide. At its upper extreme it is overlain by the Upper Mound yardangs. This surface is covered with a number of smaller mounds that form loosely defined chains (Figure 4.16). They range from 20 to 100 m in diameter and <5 to 20 m high. Bright ripples at the tens of meter scale are prevalent, probably contributing to its relatively low TI values. CRISM spectra of this area have high overall SSA and only patchy sulfate signatures. The lack of consistent sulfate signature could be due to obscuration by aeolian materials, possibly derived from the upper mound, or due to differences in textural properties.

On the southwestern edge of the knobby surface, just above Gediz Vallis, are a number of small circular features (Figure 4.19). They are too numerous to be impact craters. The direction of shadowing in HiRISE images suggests they are pits but if so they are too shallow to be resolved by the 1 m DEM. Linear features less than a meter wide separate through them, perpendicular to the edge above Gediz Vallis. A similar but areally smaller series of these pits appears ~400 meters to the north and west above.

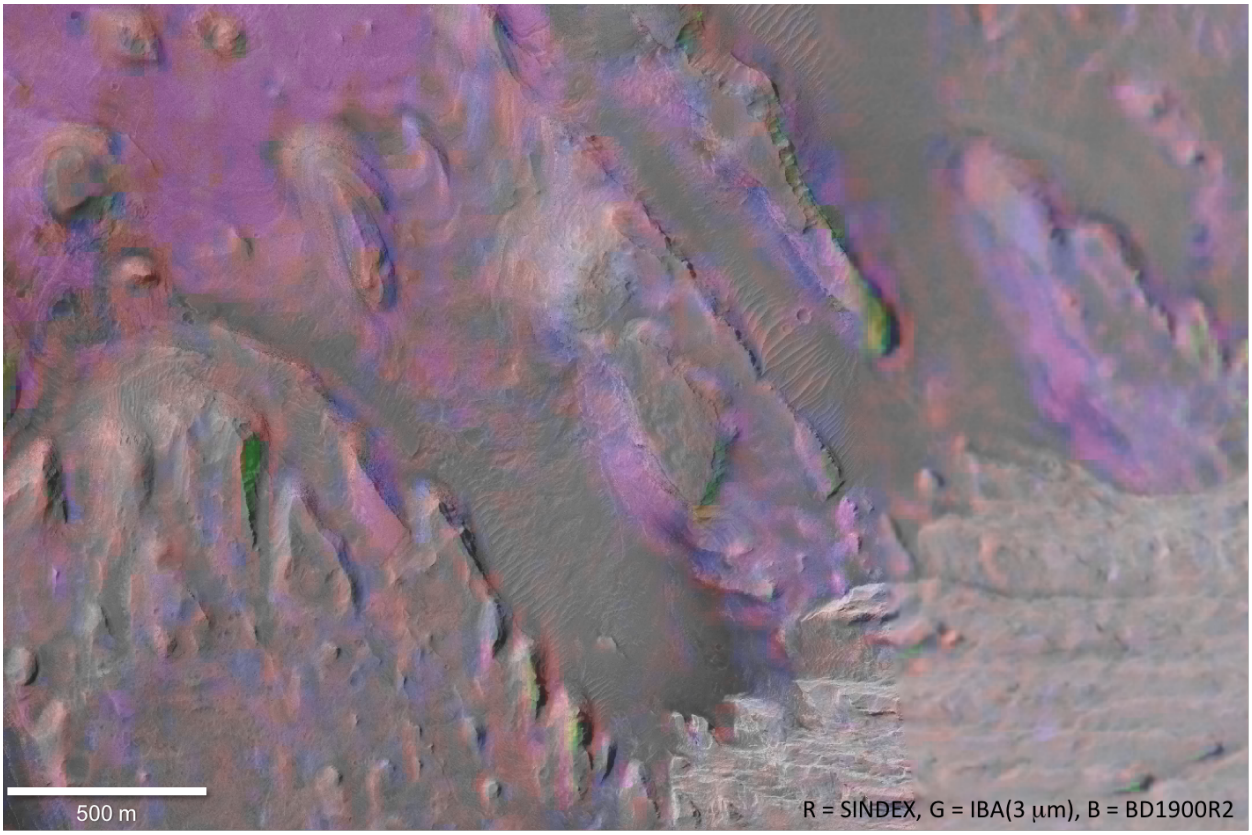

Figure 4.17: Detail of upper sulfate areas with sand cover.

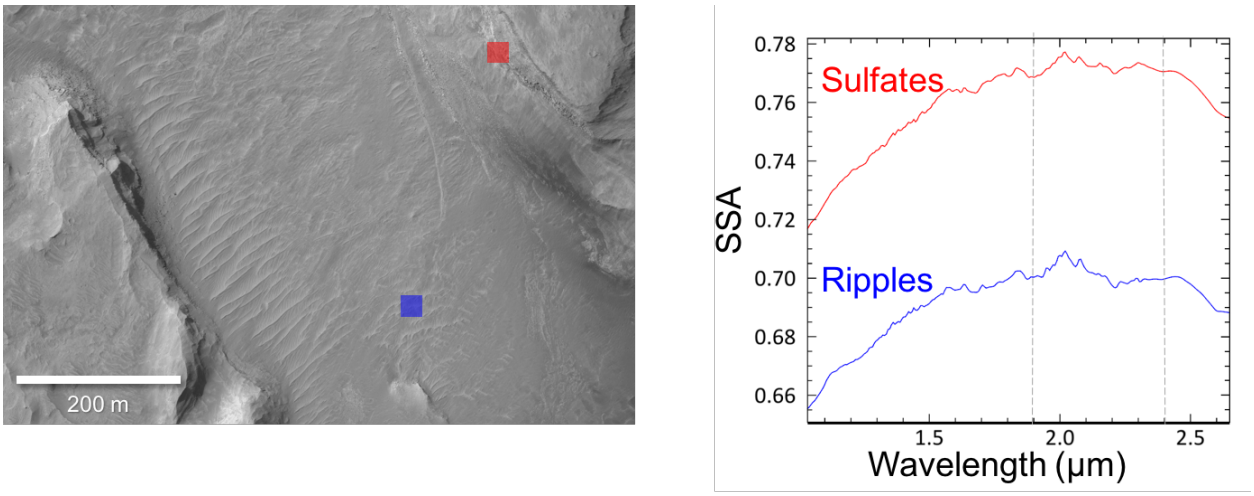

Figure 4.18: Left: Detail of uphill areas lacking a sulfate signature and obscured by unconsolidated material. Right: CRISM spectra of sands, possibly derived from duststones above, along with adjacent layered sulfate. Dashed lines are at 1.9 and 2.4 μm.

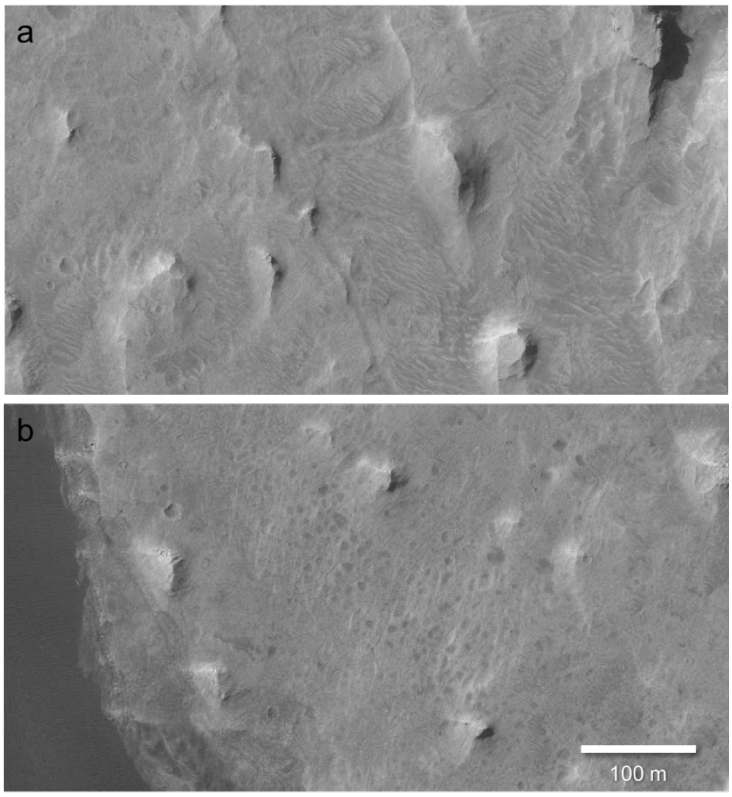

Figure 4.19: Detail of textures near the contact with the Upper Mound. Small mounds and ridges are ubiquitous throughout. Small ripples likely obscure the spectral signature of the bedrock.

4.5 Discussion

4.5.1 Trends Across the Layered Sulfates

The strength of the sulfate index (SINDEX2), the 1.9 μm band depth, and the 3 μm band depth vary throughout the layered sulfate section. A variety of factors can influence the shape of spectra and the depth of absorption features in CRISM spectra. Like previous authors, we interpret these sulfate detections as polyhydrated Mg-sulfates, given the lack of diagnostic Ca- or Fe-sulfate absorption features. We do not report any instances of monohydrated sulfate that correlate with geologic expression of features. The CRISM scene in which *Milliken et al.* [2010] reported monohydrated sulfate covers the western part of the mound and thus was not part of our study. A siliclastic component is likely present along with sulfates, contributing to the overall spectral shape and relatively low depth of absorption features. The relative proportion of minerals, grain sizes, and packing may vary as well as the amount of sand and dust cover, analogous to environments seen from orbit and at the rover scale in Meridiani Planum. Steep cliff faces and deep valleys have some of the strongest SINDEX2 values, perhaps because they are wind-swept, relatively clean surfaces. Texture is also a spectral variable; changes in grain size, packing, consolidation of strata, amount of fracturing, and erosional expression are likely to vary with slope and local setting. For instance, the layers containing boxwork fractures have a lower SINDEX2 than layers above and below, while maintaining an equivalent 1.9 μm absorption. Variations in SINDEX2 and 1.9 μm strength locally follow contiguous layers in their horizontal expression.

Within the upper and lower sulfate section, individual layers can often be traced laterally and continuously for tens or hundreds of meters. Some tentative correlations can be made between disconnected layers in adjacent buttes. The measured dips are consistently <10°. There are no obvious unconformities within the sulfate-bearing layers themselves, although Curiosity's

investigations will reveal much finer details than are visible in HiRISE. The erosional forms change from the top of the layered sulfates to the bottom; at the highest part of the section are small mounds atop a large plateau, further down are massive elongated mesas, and finally there are rounded mounds near the bottom of the section.

Thermal inertia maps were overlaid on HiRISE image mosaics of the same areas for comparison between TI and surface expression. Low and moderate-to-low thermal inertia values are well correlated with increasing wind-blown sand and regolith cover. In some areas this appears as low albedo sand sheets or ripples. In others, smaller ripples occur with similar albedo to the bedrock, possibly derived from the duststones above the layered sulfate section. The relatively clear surfaces of the layered sulfate section have thermal inertias 320-350 J m^{-2} K^{-1} $s^{-1/2}$, consistent with having similar properties throughout. These values are similar to the maximum thermal inertia of 375 J m^{-2} K^{-1} $s^{-1/2}$ of the Burns formation at wind-scoured Botany Bay, Endeavour Crater [*Arvidson et al.*, 2015].

4.5.2 Formation Conditions

There are parallels to be drawn between the layered sulfates in Gale and those in Meridiani Planum [e.g., *Grotzinger et al.*, 2005*; McLennan et al.*, 2005; *Arvidson et al.*, 2015]. They are spectrally and morphologically similar, and both form a layered section that is hundreds of meters thick. Along with sulfate species, the Gale section probably includes a basaltic component, which could be derived from the rim/central peak rocks or material previously fluvially transported into the crater. If the sulfate section can be considered an analog to the Burns formation, it may have formed in a shallow, episodically wet playa environment after the cessation of more widespread water activity in the Gale region that formed the clay units. The formation of layered sulfate deposits in Gale by groundwater upwelling, similar to Meridiani Planum, has been modeled by

Andrews-Hanna et al. [2012]. They predicted that under constant hydrological conditions, the formation of strata would cease around the observed maximum elevation of sulfates due to simultaneous deposition in other areas in the region. The layers exposed now could represent multiple periods of deposition and erosion.

The thickness of the sulfate section and the presence of repeated banding may suggest it represents multiple episodes of deposition, possibly interspersed with periods of erosion. The relatively low strikes and dips in the sulfate section are consistent with deposition in a lacustrine or evaporitic setting. The dips observed in the sulfate section, while shallow, are consistently directed outward from the center of the mound. This is consistent with the idea that the mass of layers above would have compacted layers below [*Grotzinger et al.*, 2015].

The marker bed is a unique feature within the sulfate section and may represent a different depositional environment relative to the surrounding layers. Its lack of sulfate signature and much stronger mafic mineral signature indicates a different composition. The lack of a sulfate signature may mean that it does not contain evaporites, in which case it may have formed instead in a more arid period of Gale's history. The lack of repetition of this unit suggests it was not formed as part of a cyclic process and may or may not be related to the deposition mechanism of the rest of the section. For instance, it could represent an isolated event such as an ash fall deposit.

4.5.3 Erosion Conditions

Mesas, buttes, and mounds are ubiquitous in the layered sulfate section. They show layering and sulfate-bearing compositions similar to the area between the mounds, suggesting all are part of the same depositional sequence, which has subsequently been eroded by wind. Although the mounds themselves are tall, the overall slope of the section often prevents tracing layers in walls to valley layers further uphill. Larger, taller, elongated mesas upslope give way to smaller,

shorter, rounder mounds downslope. This difference in expression may represent varying states of erosion in which the mounds could be the eroded remnants of larger features. The presence of well-developed wind erosion features suggests that hyperarid conditions have been prevalent since the end of the development of the sulfate-rich layers or their re-exposure after burial. Evidence of fluvial processes after the deposition of the sulfate section is not observed.

The Greenheugh pediment surface shares a number of similarities with surfaces to the north and west, including the Stimson Formation. The Stimson is a sandstone unit sculpted by the wind that unconformably overlies the Murray [*Watkins et al.*, 2016, *Banham et al.*, 2018]. It has composition similar to the average Mars basaltic crust [*Thompson et al.*, 2016; *Siebach et al.*, 2017] and sedimentary characteristics indicative of formation by dry aeolian processes [*Banham et al.*, 2018]. The pediment has high thermal inertia, is visually and spectrally similar to the Stimson formation, and drapes unconformably over Mt. Sharp strata. *Fraeman et al.* [2014] suggested that both may be part of a much larger surface that once draped over the Mt. Sharp group and has since been eroded back.

4.5.4 Formation of the Gediz Vallis Ridge

The ridge within Gediz Vallis is a unique feature within the study region. We suggest that the ridge was formed by relief inversion. First, a fluvial channel was formed in this location, on a surface that slopes in the same direction as this area of Mt. Sharp does now. The material within channel eventually became more resistant than its surroundings, either by cementation, armoring of its surface, or infilling by a more resistant material. The surrounding strata have since been removed, leaving behind only the channel fill and thus creating inverted relief by differential erosion. Inverted relief occurs commonly on Earth, and inverted channels and craters have been identified on Mars from orbital images [e.g., *Pain et al.*, 2007]. Inverted relief features have been

mapped on the floor of Gale Crater [*Anderson & Bell*, 2010] and in a canyon in Mt. Sharp to the south of our study area [*Thomson et al.*, 2011]. The ridge winds through sulfate layers within Gediz Vallis and terminates in a much taller stack of material, which may be the remnants of a delta where the channel met a paleolake surface. We interpret the Greenheugh pediment, which was perhaps once part of a much larger deposit, as now burying this deltaic material.

In our preferred scenario, the channel was formed within a pre-existing surface that has since been removed. The required topographic profile could have existed in this location if the Gale impact formed a peak ring, as has been suggested by previous authors [*Schwenzer et al.*, 2012; *Spray et al.*, 2013; *Baker*, 2016]. The sulfate-bearing layers were subsequently deposited on top. The lower sulfate layers formed around the pre-existing channel surface, while higher up they were able to cover the inverted channel. In the present day, the sulfates are eroding more quickly than the channel fill and exposing it on the surface of Mt. Sharp. If the inverted channel formed in strata older than the layered sulfates that have since been eroded away, it is the oldest exposed part of the section.

Alternatively, the inverted channel may have formed within the existing layered sulfate section. For instance, if the Gale impact formed a central peak rather than a ring structure, crater infill with a slope similar to the current topography would be required to provide surface for the channel to form. In this scenario the channel would be younger than much of the sulfate section and could represent a rare episode of late fluvial activity. However, if the original extent of the channel is only what is currently exposed, then additional sulfate layers could have been deposited on top since its formation. The filled channel has subsequently exhumed by wind erosion.

It is also possible that the pediment surface is older than the channel and the channel deposited material on top of it. In this case the pediment surface would have formed after the

lowest portion of the sulfate section was deposited (as it unconformably overlies these layers), after which the channel deposited material on top of it. In a related scenario, *Anderson & Bell* [2010] interpreted the distal end of the channel as the erosional remnants of a much more extensive fan-shaped deposit that shielded the pediment surface beneath. *Palucis et al.* [2016] also mapped the lowest portion of the ridge as several overlapping deltaic deposits, all overlying the pediment surface. These interpretations are less consistent with the similarity of the pediment to the Stimson formation in morphology, spectral signature, and thermal inertia. If the pediment was formed by dry aeolian processes analogously to the Stimson, it has been preserved through eras of greater water activity in the same region, e.g., those in which the channel and layered sulfates were formed, without obvious corresponding erosional features.

4.5.5 Implications for Curiosity's Traverse

The Mount Sharp Strategic Ascent route (MSAR) outlines the long-term intended path for Curiosity. Version 7 of the MSAR is shown in Figure 4.4. Part of Curiosity's route into the sulfate section is visible in Mastcam mosaics acquired while on Vera Rubin Ridge (Figures 4.21-22). After investigating the clay-bearing unit, Curiosity will enter the layered sulfate section near the Greenheugh pediment. It will have the opportunity to document several of the smaller mounds before ascending onto the pediment surface. The rover will then approach the ridge, where it will be able to search for evidence of fluvial-deltaic deposits at the base of the Gediz Vallis ridge and assess the relative stratigraphic relationships. Curiosity will then ascend the sloping pediment surface alongside the ridge. It will descend off of the ridge again by traveling eastward into the sulfate section. At the end of the MSAR it will have reached an exposure of the marker bed.

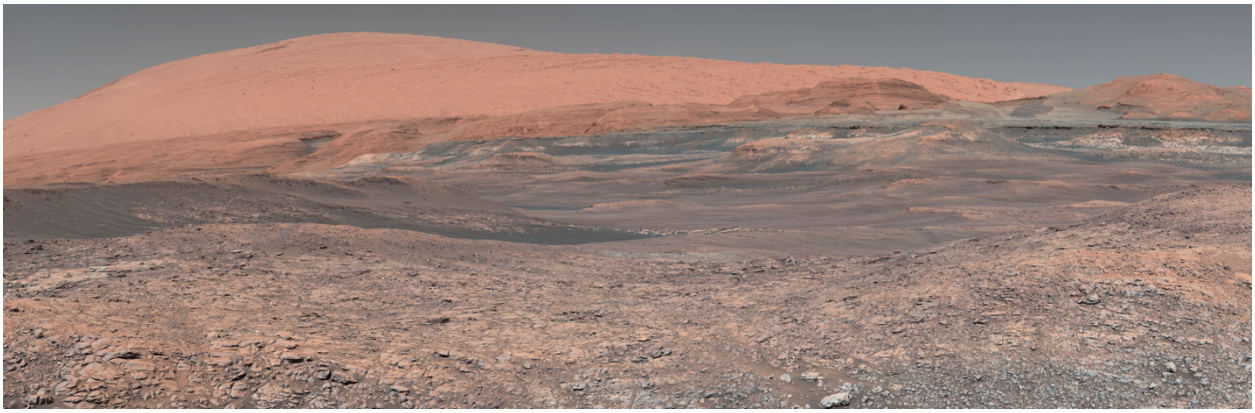

Figure 4.20: Mastcam mosaic of layered sulfate unit acquired on sol 1931 from Vera Rubin Ridge.

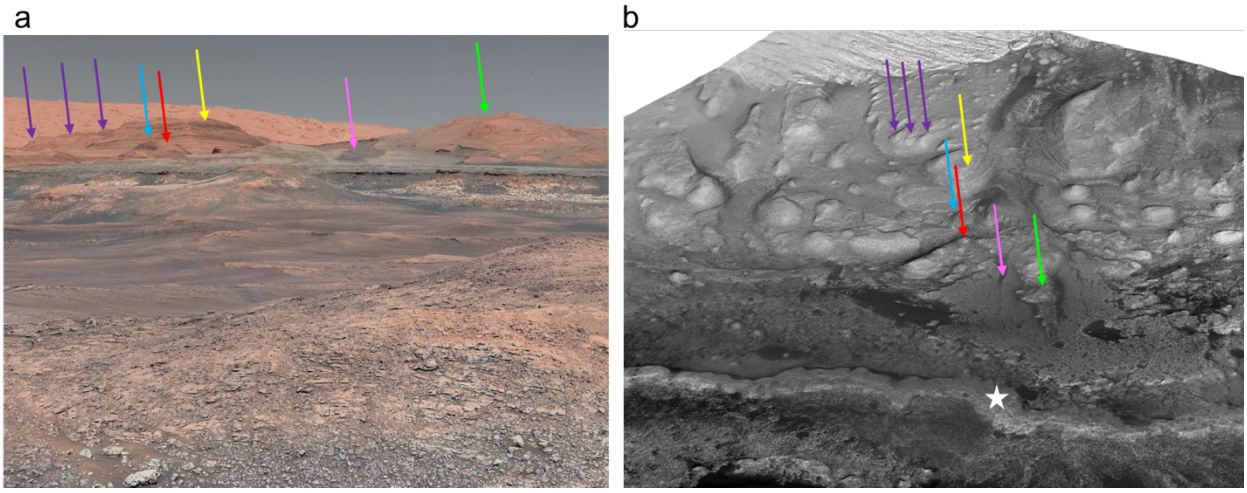

Figure 4.21: Detail of perspective view from Mastcam (left) and a perspective view of some of the same terrain from HiRISE (right). Arrows show the location of features common to the two scenes. Three purple arrows: upper unit mounds. Blue: Layered sulfate near marker bed. Red: Lower layered sulfate mound. Yellow: Large mound on side of Gediz Vallis. Pink: Sand-filled canyon within pediment surface. Green: The Gediz Vallis ridge within the pediment.

Key observations that can be made from the lower layers include the composition of layers (including by drilling into the shallow surface), fine-scale primary sedimentary features, textures, grain sizes, cementation, evidence for digenesis, and extent of aeolian cover. In particular, the marker bed should be accessible to the east of the pediment and analyzed to determine its composition and origin. Within the layered sulfate section, it will be able to identify constituent minerals. If ferric sulfates are present, they will be detectable with Mastcam wavelengths [*Wellington et al.*, 2013]. Polyhydrated Mg-sulfates may be detectable by Mastcam by enhanced

1012 nm band depth [*Rice et al.*, 2018]. Curiosity's cameras will likely resolve finer layers and greater compositional diversity than can be identified from orbit. Exploration of the lower sulfate section should reveal whether the lower layers are a continuous section. The Curiosity instrument suite can test the environmental conditions in which sulfates were deposited and determine if they were similar to the only other Martian layered sulfate section observed in situ, the Burns formation. The pediment will also be explored and various stratigraphic relationships and wet vs. dry hypotheses for its origin will be assessed.

Curiosity's exploration of Mt. Sharp represents the first time a sequence of sulfate-rich units has been observed above clay-rich units in a stratigraphic section. Observations made by Curiosity will also provide an additional ground truth data point for CRISM observations. The strength of hydrated-sulfate-related spectral absorptions is related not only to mineral abundance but also to the physical properties of the sulfate-bearing unit and regolith and dust cover. Visiting areas that appear sulfate-rich in CRISM will provide a test of CRISM observations of sulfates in other parts of the planet. The observations of geology and mineralogy made in detail by Curiosity have implications for our interpretation of sulfate-rich environments on the rest of Mars.

References

Anderson, R., and J. F. Bell (2010), Geologic mapping and characterization of Gale Crater and implications for its potential as a Mars Science Laboratory landing site, *Mars*, *5*, 76–128. doi:/10.1555/mars.2010.0004.

Andrews-Hanna, J. C., Phillips, R. J., and Zuber, M. T. (2007), Meridiani Planum and the global hydrology of Mars, *Nature*, *446*, 163–166, http://doi.org/10.1038/nature05594.

Andrews- Hanna, J. C., and Lewis, K. W. (2011), Early Mars hydrology: 2. Hydrological evolution in the Noachian and Hesperian epochs, *J. Geophys. Res.: Planets*, *116*, E02007, doi:10.1029/2010JE003709.

Andrews-Hanna, J. C., Soto, A., and Richardson, M. I. (2012), The hydrologic and climatic context of the Gale crater sedimentary mound, Abstract 7038 presented at the Third Conference on Early Mars, Lake Tahoe, Nevada, 21-25 May.

Arvidson, R. E., et al., (2006), Nature and origin of the hematite- bearing plains of Terra Meridiani based on analyses of orbital and Mars Exploration rover data sets, *J. Geophys. Res.: Planets*, *111*, E12S08, doi:10.1029/2006JE002728.

Arvidson, R. E., et al. (2014), Ancient aqueous environments at Endeavour crater, Mars, *Science*, *343*, 1248097.

Arvidson, R. E., et al. (2015), Mars Reconnaissance Orbiter and Opportunity observations of the Burns formation: crater hopping at Meridiani Planum, *J. Geophys. Res.: Planets*, *120*, 429-451.

Baker, D. M. H. (2016), Updated Catalogs of Peak-Ring Basins and Protobasins on Mars, Abstract 3046 presented at the 47th Lunar and Planetary Science Conference, The Woodlands, Texas, 21-25 March.

Banham, S. G., et al. (2018), Ancient Martian aeolian processes and palaeomorphology reconstructed from the Stimson formation on the lower slope of Aeolis Mons, Gale crater, Mars, *Sedimentology*, *65*, 993-1042.

Bellucci, G., et al. (2007), Evidence for enhanced hydration on the northern flank of Olympus Mons, Mars, *Icarus*, *192*, 361-377.

Bibring, J. P., et al. (2005), Mars surface diversity as revealed by the OMEGA/Mars Express observations, *Science*, *307*, 1576-1581, doi: 10.1126/science.1108806

Bibring, et al., (2006), Global mineralogical and aqueous mars history derived from OMEGA/Mars Express data, *Science*, *312*, 400–404, doi:10.1126/science.1122659

Bishop, J. L., et al. (2009), Mineralogy of Juventae Chasma: Sulfates in the light-toned mounds, mafic minerals in the bedrock, and hydrated silica and hydroxylated ferric sulfate on the plateau, J. *Geophys. Res.: Planets*, *114*, E00D09, doi:10.1029/2009JE003352

Bishop, J. L., Lane, M. D., Dyar, M. D., King, S. J., Brown, A. J., and Swayze, G. A. (2014), Spectral properties of Ca-sulfates: Gypsum, bassanite, and anhydrite, *American Mineralogist*, *99*, 2105-2115.

Buz, J., Ehlmann, B. L., Pan, L., and Grotzinger, J. P. (2017), Mineralogy and stratigraphy of the Gale crater rim, wall, and floor units, *J. Geophys. Res.: Planets*, *122*, 1090–1118. http://doi.org/10.1002/2016JE005163.

Calef III, F.J. and Parker, T., 2016, MSL Gale Merged Orthophoto Mosaic, Publisher: PDS Annex, U.S. Geological Survey, URL: http://bit.ly/MSL_Basemap

Chojnacki, M., Burr, D. M., Moersch, J. E., and Wray, J. J. (2014), Valles Marineris dune sediment provenance and pathways, *Icarus*, *232*, 187-219.

Christensen, P. R., et al. (2003), Morphology and composition of the surface of Mars: Mars Odyssey THEMIS results, *Science*, *300*, 2056-2061.

Christensen, P. R., et al. (2004), The thermal emission imaging system (THEMIS) for the Mars 2001 Odyssey mission, *Space Science Reviews*, *110*, 85-130.

Clark, R. N. (1999), Chapter 1: Spectroscopy of Rocks and Minerals, and Principles of Spectroscopy, in Manual of Remote Sensing, Volume 3, Remote Sensing for the Earth Sciences, (A.N. Rencz, ed.) John Wiley and Sons, New York, p 3- 58.

Clark, B. C., et al. (2005), Chemistry and mineralogy of outcrops at Meridiani Planum, *Earth and Planetary Science Letters*, *240*, 73-94.

Cloutis, E. A., et al. (2006), Detection and discrimination of sulfate minerals using reflectance spectroscopy, *Icarus*, *184*, 121-157.

Crowley, J.K. (1991), Visible and near- infrared (0.4–2.5 μm) reflectance spectra of Playa evaporite minerals, *J. Geophys. Res.: Solid Earth*, *96*, 16231-16240.

De Angelis, S., et al. (2017), Temperature-dependent VNIR spectroscopy of hydrated Mg-sulfates, *Icarus*, *281*, 444–458, doi: 10.1016/j.icarus.2016.07.022

Ehlmann, B. L., Mustard, J. F., Murchie, S. L., Bibring, J. P., Meunier, A., Fraeman, A. A., and Langevin, Y. (2011), Subsurface water and clay mineral formation during the early history of Mars, *Nature*, *479*, 53.

Ehlmann, B. L., and Edwards, C. S. (2014), Mineralogy of the Martian surface, *Annual Review of Earth and Planetary Sciences*, *42*, 291-315.

Fergason, R. L., Christensen, P. R., and Kieffer, H. H. (2006), High- resolution thermal inertia derived from the Thermal Emission Imaging System (THEMIS): Thermal model and applications, *J. Geophys. Res.: Planets*, *111*, E12004, doi:10.1029/2006JE002735.

Fox, V. K., Bennett, K. A., Vasavada, A. R., Stack, K. M., and Ehlmann, B. L. (2018), The Clay-Bearing Unit of Mount Sharp, Gale Crater, I: Orbital Perspective and Initial Results, Abstract 1728 presented at the 49th Lunar and Planetary Science Conference, The Woodlands, Texas, 19-23 March.

Fraeman, A. A., et al. (2016), The stratigraphy and evolution of lower Mount Sharp from spectral, morphological, and thermophysical orbital data sets, *J. Geophys. Res.: Planets*, *121*, 1713-1736.

Gendrin, A. et al. (2006), Sulfates in Martian Layered Terrains: The OMEGA/Mars Express View, *Science*, *307*, 1587-1591, doi: 10.1126/science.1109087.

Glotch, T. D., et al. (2006), Mineralogy of the light- toned outcrop at Meridiani Planum as seen by the Miniature Thermal Emission Spectrometer and implications for its formation*, J. Geophys. Res.: Planets*, *111*, E12, doi:10.1029/2005JE002672.

Grant, J. A., Wilson, S. A., Mangold, N., Calef, F., and Grotzinger, J. P. (2014), The timing of alluvial activity in Gale crater, Mars, *Geophysical Research Letters*, *41*, 1142-1149.

Griffes, J. L., Arvidson, R. E., Poulet, F., and Gendrin, A. (2007), Geologic and spectral mapping of etched terrain deposits in northern Meridiani Planum, *J. Geophys. Res.: Planets*, *112*, E08S09, doi:10.1029/2006JE002811.

Grotzinger, J. P. et al., (2005), Stratigraphy and sedimentology of a dry to wet eolian depositional system, Burns formation, Meridiani Planum, Mars, *Earth and Planetary Science Letters*, *240*, 11-72.

Grotzinger, J. P. et al., (2012), Mars Science Laboratory mission and science investigation, *Space Science Reviews*, *170*, 5-56.

Grotzinger, J. P., et al. (2014), A Habitable Fluvio-Lacustrine Environment at Yellowknife Bay, Gale Crater, Mars, *Science*, *343*, http://doi.org/10.1126/science.1242777

Grotzinger, J. P., et al. (2015), Deposition, exhumation, and paleoclimate of an ancient lake deposit, Gale crater, Mars, *Science*, *350*, aac7575.

Hapke, B. (2012), Theory of Reflectance and Emittance Spectroscopy, Cambridge Univ. Press, New York.

He, L., et al. (2017), Resolution Analysis of Regularized Maximum Log-likelihood Reconstruction Method for CRISM Hyperspectral Data, Paper JTu5A presented at Propagation Through and Characterization of Atmospheric and Oceanic Phenomena, San Francisco, California, 26-29 June.

He, L., R.E. Arvidson and J.A. O'Sullivan (2018), Retrieving Single Scattering Albedos and Temperatures from CRISM Hyperspectral Data Using Neural Networks, Abstract 6052 presented at Planetary Science and Informatics and Data Analytics, St. Louis, MO, 24-26 April.

Jamieson, C. S., E. Z. Noe Dobrea, J. B. Dalton III, K. M. Pitman, and W. J. Abbey (2014), The spectral variability of kieserite (MgSO4·H2O) with temperature and grain size and its application to the Martian surface, *J. Geophys. Res.: Planets*, *119*, 1218–1237, doi:10.1002/2013JE004489.

Kreisch, C. D., et al. (2017), Regularization of Mars Reconnaissance Orbiter CRISM along- track oversampled hyperspectral imaging observations of Mars, *Icarus*, *282*, 136-151.

Lane, M. D., et al. (2015), Mid-infrared emission spectroscopy and visible/near-infrared reflectance spectroscopy of Fe-sulfate minerals, *American Mineralogist*, *100*, 66-82.

Langevin, Y., Poulet, F., Bibring, J. P., and Gondet, B. (2005), Sulfates in the north polar region of Mars detected by OMEGA/Mars Express, *Science*, *307*, 1584-1586.

Le Deit, L., Hauber, E., Fueten, F., Pondrelli, M., Rossi, A. P., and Jaumann, R. (2013), Sequence of infilling events in Gale Crater, Mars: Results from morphology, stratigraphy, and mineralogy, *J. Geophys. Res.: Planets*, *118*, 2439-2473.

Lichtenberg, K. A., et al. (2010), Stratigraphy of hydrated sulfates in the sedimentary deposits of Aram Chaos, Mars, *J. Geophys. Res.: Planets*, *115*, E00D17. http://doi.org/10.1029/2008JE003208.

Malin, M. C., and Edgett, K. S. (2000), Sedimentary rocks of early Mars, *Science*, *290*, 1927-1937.

Malin, M. C., et al. (2008), Climate, weather, and north polar observations from the Mars Reconnaissance Orbiter Mars Color Imager, *Icarus*, *194*, 501-512.

Mangold, N., et al. (2008), Spectral and geological study of the sulfate-rich region of West Candor Chasma, Mars, *Icarus*, *194*, 519-543.

McEwen, A.S., et al. (2007), Mars Reconnaissance Orbiter's High Resolution Imaging Science Experiment (HiRISE), *J. Geophys. Res.*, *112*, E05S02, doi:10.1029/2005JE002605.

McGuire, P. C., et al. (2009), An improvement to the volcano-scan algorithm for atmospheric correction of CRISM and OMEGA spectral data, *Planetary and Space Science*, *57*, 809-815.

McLennan, S. M., et al. (2005), Provenance and diagenesis of the evaporite-bearing Burns formation, Meridiani Planum, Mars, *Earth and Planetary Science Letters*, *240*, 95-121.

Milliken, R. E., Grotzinger, J. P., and Thomson, B. J. (2010), Paleoclimate of Mars as captured by the stratigraphic record in Gale Crater, *Geophysical Research Letters*, *37*, L04201, doi:10.1029/2009GL041870.

Morris, R. V., et al. (2006), Mössbauer mineralogy of rock, soil, and dust at Meridiani Planum, Mars: Opportunity's journey across sulfate-rich outcrop, basaltic sand and dust, and hematite lag deposits, *J. Geophys. Res.*, *111*, E12S15, doi:10.1029/2006JE002791.

Murchie, S., et al. (2007), Compact reconnaissance imaging spectrometer for Mars (CRISM) on Mars reconnaissance orbiter (MRO), *J. Geophys. Res.: Planets*, *112*, E05S03, doi:10.1029/2006JE002682.

Murchie, S., et al. (2009), Evidence for the origin of layered deposits in Candor Chasma, Mars, from mineral composition and hydrologic modeling, *J. Geophys. Res.: Planets*, *114*, E00D05, doi:10.1029/2009JE003343.

Pain, C. F., Clarke, J. D. A., & Thomas, M., (2007), Inversion of relief on Mars, *Icarus*, *190*, 478-491.

Palucis, M. C., et al. (2016), Sequence and relative timing of large lakes in Gale crater (Mars) after the formation of Mount Sharp, *J. Geophys. Res.: Planets*, *121*, 472-496.

Parker, T. and Calef III, F.J. (2016), MSL Gale Merged Digital Elevation Model, Publisher: PDS Annex, U.S. Geological Survey, URL: http://bit.ly/MSL_DEM

Pommerol, A., and Schmitt, B. (2008), Strength of the H2O near- infrared absorption bands in hydrated minerals: Effects of particle size and correlation with albedo, *J. Geophys. Res.: Planets*, *113*, E10009, doi:10.1029/2007JE003069.

Powell, K. E., Arvidson, R. E., Zanetti, M., Guinness, E. A., and Murchie, S. L. (2017), The structural, stratigraphic, and paleoenvironmental record exposed on the rim and walls of Iazu Crater, Mars, *J. Geophys. Res.: Planets*, *122*, 1138-1156.

Rampe, E. B., et al. (2017), Mineralogy of an ancient lacustrine mudstone succession from the Murray formation, Gale crater, Mars, *Earth and Planetary Science Letters*, *471*, 172-185.

Rice, M. S., Dixon, D., Bell, J. F., Wellington, D., and Johnson, J. R. (2018), Spectral Variability of Sulfate Veins Observed by Mastcam Along Curiosity's Traverse in Gale Crater, Mars, Abstract 2949 presented at the 49th Lunar and Planetary Science Conference, The Woodlands, Texas, 19-23 March.

Siebach, K. L., and Grotzinger, J. P. (2014), Volumetric estimates of ancient water on Mount Sharp based on boxwork deposits, Gale Crater, Mars, *J. Geophys. Res.: Planets*, *119*, 189-198.

Siebach, K.L. et al. (2017), Geochemistry of the Stimson Sandstone, Gale Crater, Mars, Abstract 2499 presented at the 48th Lunar and Planetary Science Conference, The Woodlands, Texas, 20-24 March.

Spray, J. G., Elliott, B. E., and Thompson, L. M. (2013), The Gale Impact Structure, Mars: Original Shape and Formation Age, Abstract 1719 presented at the 44th Lunar and Planetary Science Conference, The Woodlands, Texas, 18-22 March.

Squyres, S. W., et al. (2012), Ancient impact and aqueous processes at Endeavour Crater, Mars, *Science*, *336*, 570–576, doi:10.1126/science.1220476.

Stack, K. M., and Milliken, R. E. (2015), Modeling near-infrared reflectance spectra of clay and sulfate mixtures and implications for Mars, *Icarus*, *250*, 332-356.

Stamnes, K., Tsay, S. C., Wiscombe, W., and Jayaweera, K. (1988), Numerically stable algorithm for discrete-ordinate-method radiative transfer in multiple scattering and emitting layered media, *Applied Optics*, *27*, 2502-2509.

Schwenzer, S. P. et al. (2012), Gale Crater: Formation and post-impact hydrous environments, *Planetary and Space Science*, *70*, 84-95.

Thompson, L.M. et al. (2016), APXS Compositional Trends Along Curiosity's Traverse, Gale Crater, Mars: Implications for Crustal Composition, Sedimentary Provenance, Diagenesis, and Alteration, Abstract 2709 presented at the 47th Lunar and Planetary Science Conference, The Woodlands, Texas, 21-25 March.

Thomson, B. J., et al. (2011), Constraints on the origin and evolution of the layered mound in Gale Crater, Mars using Mars Reconnaissance Orbiter data, *Icarus*, *214*, 413-432.

Viviano-Beck, C. E., et al. (2014), Revised CRISM spectral parameters and summary products based on the currently detected mineral diversity on Mars, *J. Geophys. Res.: Planets*, *119*, 1403-1431.

Watkins, J. A., et al. (2016), Paleotopography of erosional unconformity, base of Stimson formation, Gale crater, Mars, Abstract 2939 presented at the 47th Lunar and Planetary Science Conference, The Woodlands, Texas, 21-25 March.

Watkins, J. A., Grotzinger, J. P., and Avouac, J. P. (2017), Fracture formation by compaction-related burial in Gale Crater, Mars: Implications for the origin of Aeolis Mons, Abstract 3019 presented at the 48th Lunar and Planetary Science Conference, The Woodlands, Texas, 20-24 March.

Wellington, D. F., et al. (2017), Visible to near-infrared MSL/Mastcam multispectral imaging: Initial results from select high-interest science targets within Gale Crater, Mars, *American Mineralogist*, *102*, 1202-1217.

Wiseman, S. M., et al. (2010), Spectral and stratigraphic mapping of hydrated sulfate and phyllosilicate- bearing deposits in northern Sinus Meridiani, Mars, *J. Geophys. Res.: Planets*, 115, E00D18, doi:10.1029/2009JE003354.

Wolff, M. J., et al. (2009), Wavelength dependence of dust aerosol single scattering albedo as observed by the Compact Reconnaissance Imaging Spectrometer, *J. Geophys. Res: Planets*, 114, E00D04, doi:10.1029/2009JE003350.